Distribution Agreement

In presenting this thesis or dissertation as a partial fulfillment of the requirements for an advanced degree from Emory University, I hereby grant to Emory University and its agents the non-exclusive license to archive, make accessible, and display my thesis or dissertation in whole or in part in all forms of media, now or hereafter known, including display on the world wide web. I understand that I may select some access restrictions as part of the online submission of this thesis or dissertation. I retain all ownership rights to the copyright of the thesis or dissertation. I also retain the right to use in future works (such as articles or books) all or part of this thesis or dissertation.

Signature:

_____

Chen Liang Date

CONFORMATIONAL EVOLUTION IN AMYLOID SELF-ASSEMBLY

By

Chen Liang
Doctor of Philosophy
Chemistry

_____

Dr. David G. Lynn
Advisor

_____

Dr. Emily Weinert
Committee Member

_____

Dr. Khalid S. Salaita
Committee Member

Accepted:

_____

Lisa A. Tedesco, Ph.D.
Dean of the James T. Laney School of Graduate Studies

_____ Date

CONFORMATIONAL EVOLUTION IN AMYLOID SELF-ASSEMBLY

By

Chen Liang

B. S., China Pharmaceutical University, 2011

Advisor: David G. Lynn, PhD.

An abstract of

A dissertation submitted to the Faculty of the

James T. Laney School of Graduate Studies of Emory University

in partial fulfillment of the requirements for the degree of

Doctor of Philosophy

in Chemistry

2017

Abstract

Amyloid has been correlated with numerous protein misfolding diseases, yet no effective treatment is currently available. A thorough understanding of the misfolding process is crucial for understanding the disease mechanism and designing therapeutics. This dissertation presents a conformational evolution model that builds on earlier nucleation dependent assembly and polymorphism models. The nucleating core of Aβ Dutch mutant, Aβ (16-22) E22Q is quantitatively characterized to go through a conformational transition from anti-parallel out-of-register to parallel strand orientation. Solid-state NMR and isotope-edited infrared (IE-IR) spectroscopies are developed to assign basis sets for monitoring and resolving the evolving conformations. The impact of single amino acid mutation and ionic strength of the environment are used to reveal the sensitivity of the self-assembly process to intrinsic and extrinsic modulators along the evolving energy surface.

Significant extension of local and normal IR active modes are uniquely revealed in the extended amyloid secondary structure and these are extended and optimized for the analyses. Overall, the results extend and enhance our current understanding of amyloid assembly for the potential design of therapeutics for neurodegenerative diseases.

CONFORMATIONAL EVOLUTION IN AMYLOID SELF-ASSEMBLY

By

Chen Liang

B. S., China Pharmaceutical University, 2011

Advisor: David G. Lynn, PhD

A dissertation submitted to the Faculty of the

James T. Laney School of Graduate Studies of Emory University

in partial fulfillment of the requirements for the degree of

Doctor of Philosophy

in Chemistry

2017

ACKNOWLEDGMENTS

First of all, I would like to express my deep gratitude towards my thesis advisor, Professor David G. Lynn. During the past 6 years of graduate studies, he has been a mentor for both science and life. He fueled my curiosity, encouraged me to ask bold questions, and led me to the discovery that the boarder of science can always be pushed. His enthusiasm towards education and mentorship as helped me to become a scientist. I'm also grateful for my second academic advisors, Professor Emily Weinert and Professor Khalid Salaita for being my role model in science and providing insightful suggestions to my research projects.

For conducting experiments, I would first like to thank Dr. Meth Anil for not only carrying out critical experiments, but having the wisdom to provide valuable suggestions and break many bottle necks. He is a rigorous scholar and patient mentor. Additionally, I'm grateful for Dr. Hong Yi of department of neurology and Dr. John Bacsa for their generous guidance with TEM and X-ray diffraction experiments.

I've enjoyed such a privilege to work with so many colleagues at Lynn lab. Dr. Yue Liu, Dr. Chenrui Chen, and Dr. Junjun Tan are my sisters in spirit. Dr. Sha Li, Dr. Li Zhang, and Dr. Savannah Johnson are my elder friends, Dr. Jay Goodwin, Dr. Jill Smith, Dr. Dibyendu Das, Dr. Neil Anthony, Dr. Yi-Han Lin, Dr. Olga Taran, Dr Yushi Bai and Dr. Daniel Pierce, Dr. Tolu

Omosun are my mentors and offered great guidances. Many thanks to Rolando Rengifo, Ting Pan, Jackey Hsieh, Noel Li, Allisandra Mowles, Anthony Sementilli and Siying Cen for your company. Your presence makes workplace into my second home.

Aside from research, I have the privilege to have founded Student Educational Experience Development with the help of Dr. Barbara Coble and many friends. The passion and dedication of you made it a successful program that have huge impact in the life of many Atlanta public high school students.

I consider myself lucky to have so many friends and such a big church family. We walked through tears and laughter together.

Finally, I would like to address my thanks to my Father Guosheng Liang and my Mother Xingzao Dai for supporting my dream and loving me deeply. You are my motivation to excel; also to Dr. Yang Dai, my uncle who inspired me to study in us, and the rest of my family who love me unconditionally.

Table of Contents

List of Figures

List of Tables

Chapter 1. Background

Protein self-assembly

Self-assembly is a process that results in the formation of well-defined structures from individual molecular building blocks. [3]The evolution of biology is built on small molecules that aggregate, increase their relative order and form complex assemblies essential for living organisms. Protein represents a crucial part of these self-assembly systems. Their amphiphilic characteristics, self-replicating capacity[4] and variety of potential interactions[5] make them suitable for building supramolecules with various functions. Multiple studies have been conducted on the correlation between peptide and evolution. Our group studied peptide membranes as potential agents in chemical evolution. [6]A amyloid-like self-assembly constructs critical cellular components for normal functions [7] and Bernd M. Rode et.al hypothesized that peptide formation proceeds RNA.[8]

The study of protein self-assembly is also crucial for the understanding disease mechanisms. Self-assembling peptides amyloid peptides have been shown to be closely associated with multiple neurodegenerative diseases such as Alzheimer's disease, prion disease and type II diabetes. [9, 10-12,13, 14] Recently, Aβ has been discovered to exhibit prion-like behaviors, allowing

it to spread and convert soluble monomers to toxic aggregates. [15]

In this thesis, I will focus on Aβ(1-40) or Aβ(1-42) and their derivative, which are hypothesized to cause neuronal loss through mechanisms involving cellular membrane penetration, direct receptor interaction and oxidative stress, [16] and are targets for therapeutics[17].

Peptide self-assembly has now been widely adopted in the fabrication of macromolecules with a diversity of structures and functions. Due to their biocompatibility, biodegradability, easy availability and cost effectiveness[18], they have been put into applications varying from tissue regeneration and drug delivery, surface engineering and the cosmetic industry. [19]For example, high order self-assembled amyloids are applied in fabricating scaffolds that can support cell attachment and spread, [20,21] self-assembled biofilm that support nanoparticles for transferring photo-induced electrons,[22] and targeted drug delivery and vaccine engineering[23]. Therefore, a thorough understanding of the self-assembly process is fundamental to both promoting the understanding of life, explore disease mechanisms, and expanding our capacity to precisely control the properties of self-assembled biomaterials.

Cross-beta structure

Amyloids have common structural architectures know from their X-ray diffraction patterns known as cross-beta, in which extended β-sheets stack on top of each other to form fibers with widths of nanometer scale. The hydrogen bonds run parallel to fiber long axis and orthogonal

to beta-sheet stacking.

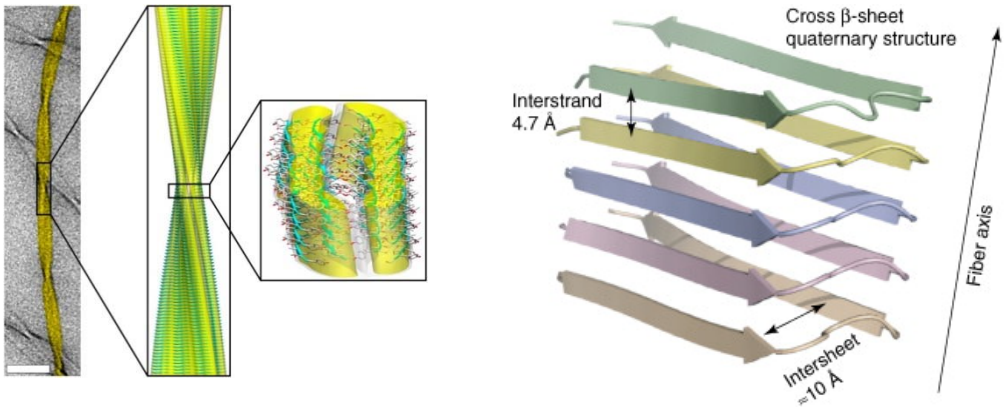

Figure 1-1. Structure of amyloid cross-beta structure [1,2]

Due to the variety of functional groups on peptides, different groups can have multiple interactions through hydrogen bonding, Π-Π stacking, hydrophobic, electrostatic, and van der Waals interactions to direct molecular of assembly. The energy landscape of the folding process however could proceed through multiple metastable states until the thermodynamically favored structure is formed. This pathway could then have a profound and environmentally sensitive impact on any control we hope to have on the final structure. Decoding this pathway became a major focus of this dissertation.

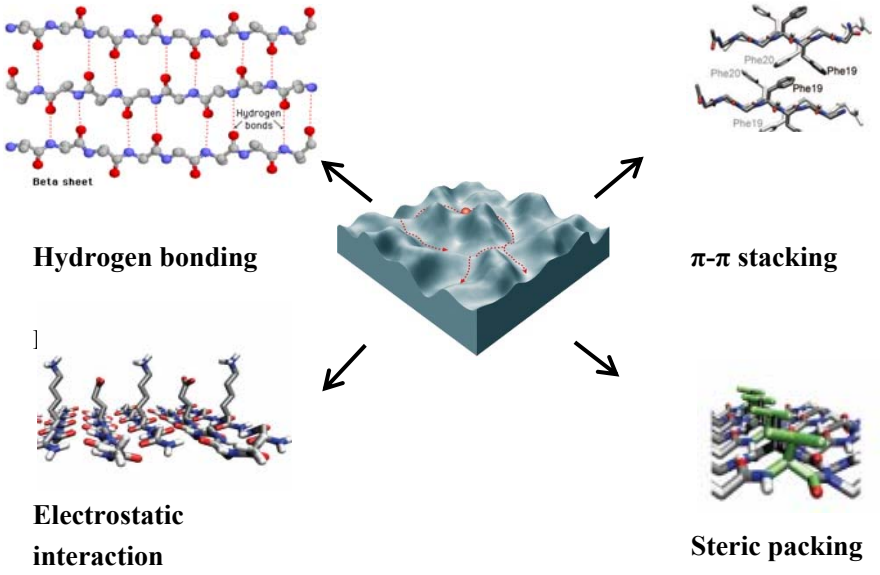

Figure 1-2. Physical forces dictate the final structure of amyloid self-assembly.

Decoding amyloid self-assembly

We will refer to the physical factors dictating amyloid self-assembly as “code of assembly”. It is analogues to A/T and G/C molecular codes that dictate nucleic acid assembly, however, unlike DNA, whose conformation is precisely dictated by base paring with defiend fidelity and reproducibility, self-assembly of proteins is far more diverse and highly sensitive to the assembly environment and process.[3] Such diversity provides protein self-assembly far more structural complexity and greater potential for functionality. Using the nucleating core of Aβ peptide and its congeners as a model system, we have interpreted several physical factors that determine the structure of amyloid and also demonstrate structurally how environmental factors influence this process. This information contributes to more precise prediction of peptide self-

assembly and protein folding[5], and provide insight into how the process might be controlled and used. The specific forces that regulates the folding energy landscape include:

A. Electrostatic forces

Electrostatic forces between charged residues can define the structure of self-assembly. Under neutral pH[24], Aβ (16-22) or Ac-^{16}KLVFFAE^{22}-NH_2 assembles into anti-parallel in-register peptide and the salt bridge formed between positively charged lysine and negatively charged glutamic acid maintained in-register strand arrangement of twisted fibers.[24] The strength of such electrostatic interaction is mitigated by the solvent. Permittivity is used to measure how the solvent affects the Coulomb force between two point charges. Relative permittivity, commonly known as dielectric constant, is the factor by which the two charges' electric field is decreased relative to vacuum. Water has high dielectric constant, organic solvents have lower dielectric constant. Under dehydrated environments, the electrostatic interaction is stronger.

B. V-A cross-strand pairing

When the glutamic acid is protonated, Aβ (16-22) forms anti-parallel out-of-register β-sheets that under TEM were nanotubes. Such a shift in one amino acid is assigned to the β-branched V18 residue and its preferential packing against alanine in the adjacent strand.[25] Without the salt bridge, such steric packing between bulky valine and small alanine becomes the major determinator of β-sheets conformation. When V18 is replaced with bulkier t-butyl side chain,

the peptide remains out-of-register even under conditions where the salt bridge is expected to be most stable. Environment serves as a mediator between various physical forces that collectively dictate amyloid structure.

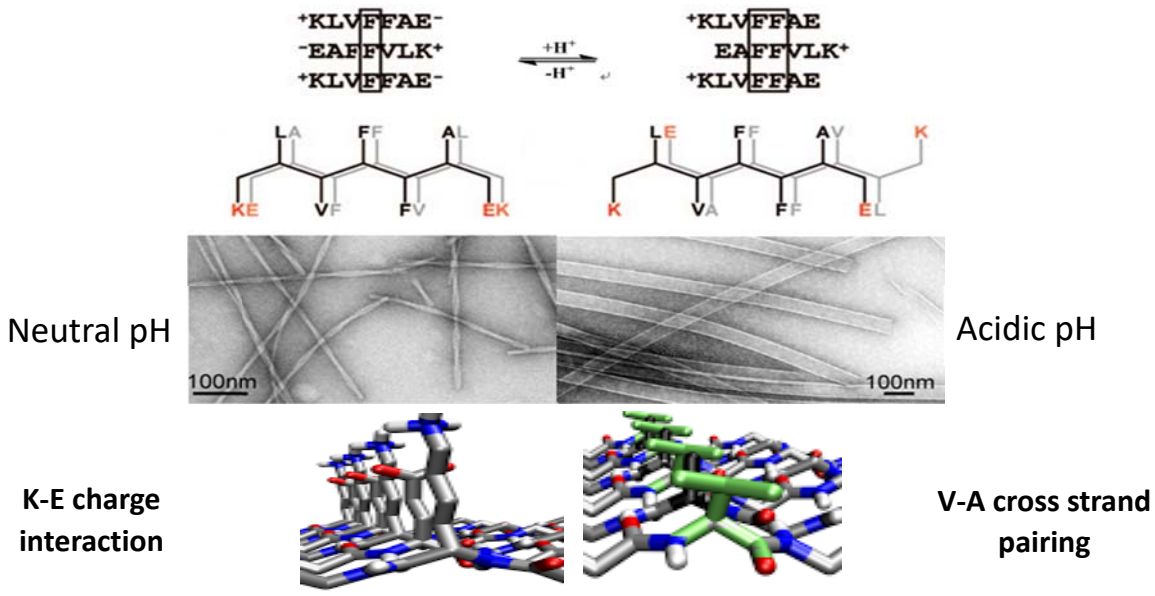

Figure 1-3. Electrostatic interaction and V-A cross-strand paring dictates the conformation of Aβ (16-22)

C. Q-Q cross-strand hydrogen bonding

Glutamine can have a strong influence on self-assembled structures. Aβ (16-22) E22Q forms parallel in-register β-sheets where the stabilizing constraint is assigned to inter-sheet hydrogen bond between glutamines known as Q track.

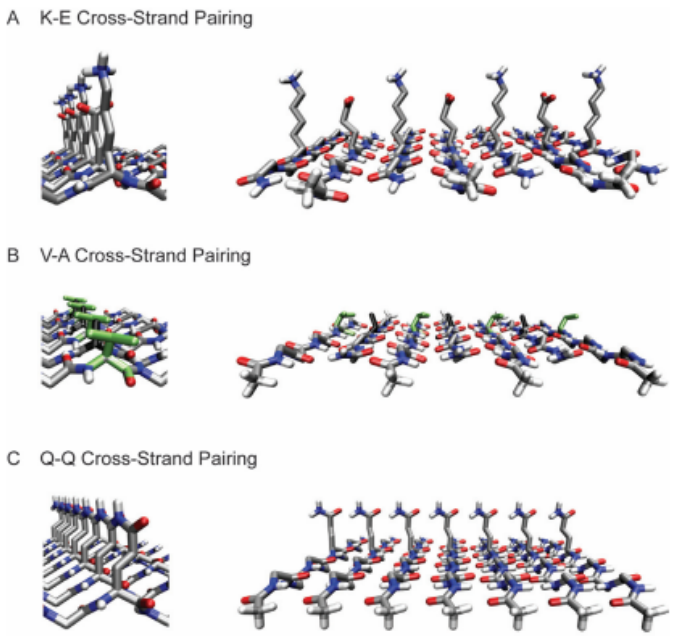

Figure 1-4. Summary of molecular forces that dictate self-assembly with β-sheet.

D. Lamination

Lamination, or steric zipper [26]is defined as the dry interface formed by packing the side chains of adjacent β-sheets[26]. This hydrophobic stacking dictates the initial hydrophobic collapse of amyloid and controls the morphology of steric zipper. In the case of Aβ (16-22)[24], when assembled into anti-parallel in-register conformations, the hydrophobicity above and below the β-sheet are different and have been argued to be symmetrical for anti-parallel out-of-register. The morphologies of fiber vs tube is related to the difference in lamination (**Figure 1-5**).

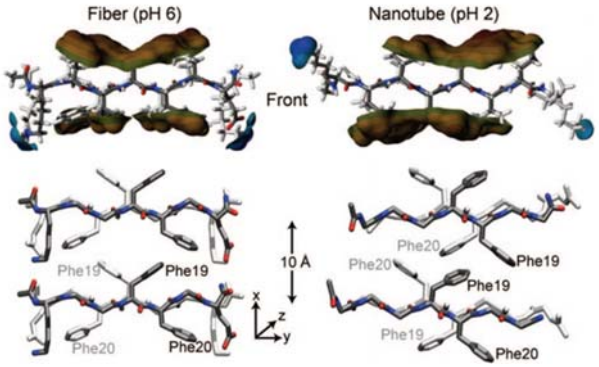

Figure 1-5. Hydrophobic surface for fiber and tubes. The hydrophobic surface of in-register anti-parallel β-sheet (left) and out-of-register anti-parallel β-sheet (right). Brown indicate hydrophobic surface, blue hydrophilic regions, green stands for neutral areas.

The self-assembly process

Our growing understanding of the forces that control assembly now make it possible to evaluate the different models that have been proposed.

Nucleation dependent self-assembly

The most well established model is the nucleation dependent model. From peptide monomers to large scale macromolecules, amyloid goes through two stages, nucleation and elongation.[27] As shown in **figure 1-6** (**A and B**), from the solution phase the peptide hydrophobic core undergoes hydrophobic collapse via a liquid-liquid phase transition into a particle phase. Within the particle, paracrystalline nuclei are formed and serve as a template for further monomer addition; elongation is defined as growing nuclei into full mature fiber, a process that exhibits exponential growth as demonstrated by thioflavin T binding.[28]The addition of mature fiber

seeds at the beginning of assembly trigger elongation immediately, bypassing nucleation phase[28]. The seeding process has been widely characterized, both in vitro and in vivo[29], and this prion-like property is of great significance in both the progression of neurodegenerative diseases[30] and development of bio-materials.[31]

It is worth noting that the chemical environment of nucleation differs from the elongation stage (**Figure 1-6 C**). Within the particle, the peptide concentration is high, peptides appear to be less ordered in the particle, and free monomers are under rapid exchange. Despite the dynamic nature of particle, the internal environment is expected to be more desolvated such that the energetics of peptide alignment in the grown would differ from propagation in solution. Such differences in environment could lead to different energetics and a different initial morphology.

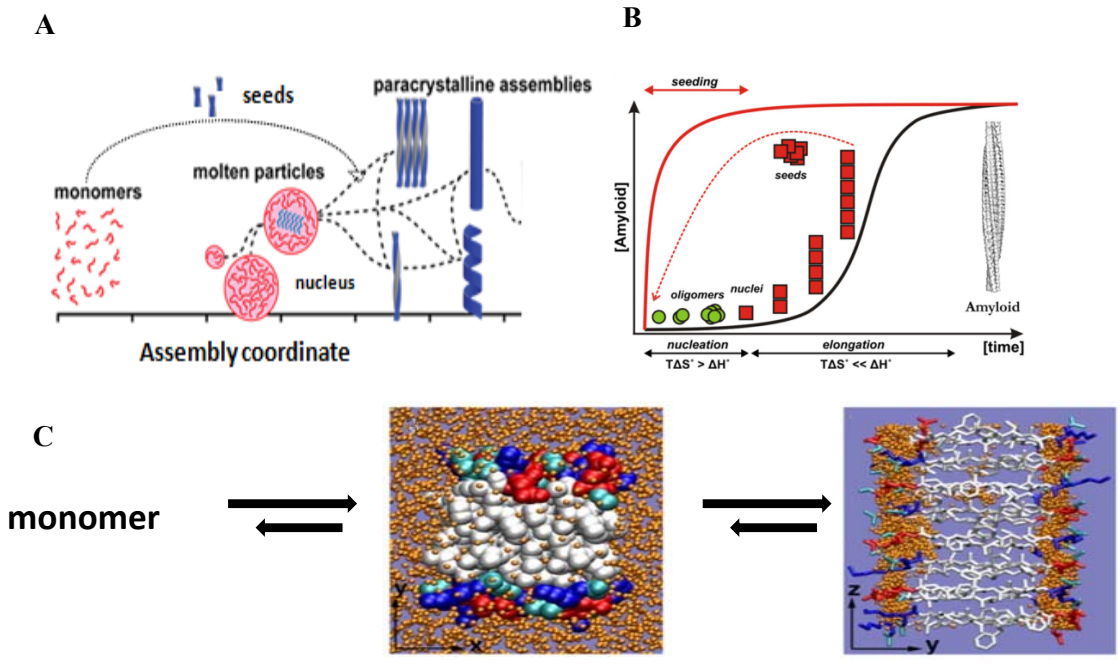

Figure 1-6. Process of self-assembly process
(A) Assembly stages represented by the increasing molecular order
(B) Assembly process with and wihtout seeding, represented by quantity of amyloid
(C) The anticipated environmental difference between nucleation and elongation environments. [32]

Polymorphism in amyloid self-assembly

Under certain conditions amyloid fibers can be polymorphic, meaning that within a given sequence, the peptides assemble into different morphologies with distinct fibril structures. These various structures can co-exist for extended periods of time due to the high thermostability of amyloid and multiple energy minimum across the energy landscape.[27] The formation of polymorphism can result from different bundling or twisting of protofibers, or fundamentally different structures (**Figure 1-7**). The study of polymorphism is significant in the study of neurodegenerative diseases[33]. Studies have shown different toxicity[34], interaction with cells, propagation rate[35], stability and propagation mechanism between various polymorphs. Initial efforts have been able to characterized the structures of polymorphic amyloid structures and define structures with different toxicities.[36]

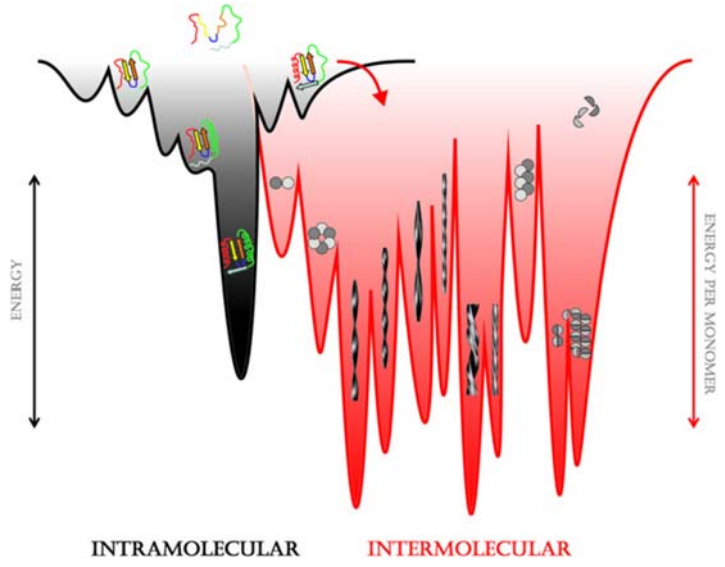

Figure 1-7. Comparison of energy landscape between soluble proteins and amyloid. Unlike soluble proteins, amyloid possesses many energy minimum with high thermostability, setting the foundation for polymorphism.[27]

The structure of amyloid is not only determined by the absolute thermostability, but also the assembly pathway. A review done by Wang et.al has comprehensively reviewed the kinetics of assembly condition on the amyloid pathway. [18]The evaluated factors include temperature, solvent composition, pH, ionic strength and shear forces. These environmental conditions impact assembly by regulating molecular interactions. Even if the final assembly condition is identical, some self-assembly pathway can be extremely sensitive to the preparation protocol. Korevaar et.al revealed that by adding different percentages of HFIP in water leads to a drastic difference in the supramolecular morphology of the peptide amphiphiles. [37]

Conformational evolution in amyloid self-assembly process

As techniques mature for monitoring assembly overtime, kinetic intermediates whose structures are different from the stable conformation have been defined even without any outside environmental perturbation, along the assembly pathway. Such conformational evolution results from a difference of activation energy and thermostability between different conformational species. The kinetic intermediates emerge as a result of lowered activation energy while the stable conformation persists due to higher thermostability. Such stable conformations can appear as a result of secondary nucleation, mutation or internal structural re-arrangement. The more stable conformation shifts the equilibrium of the system and assimilates all peptides. Depending on the relative stability of the intermediate, its life time can vary significantly form almost undetectable to persisted (**Figure 1-8**).

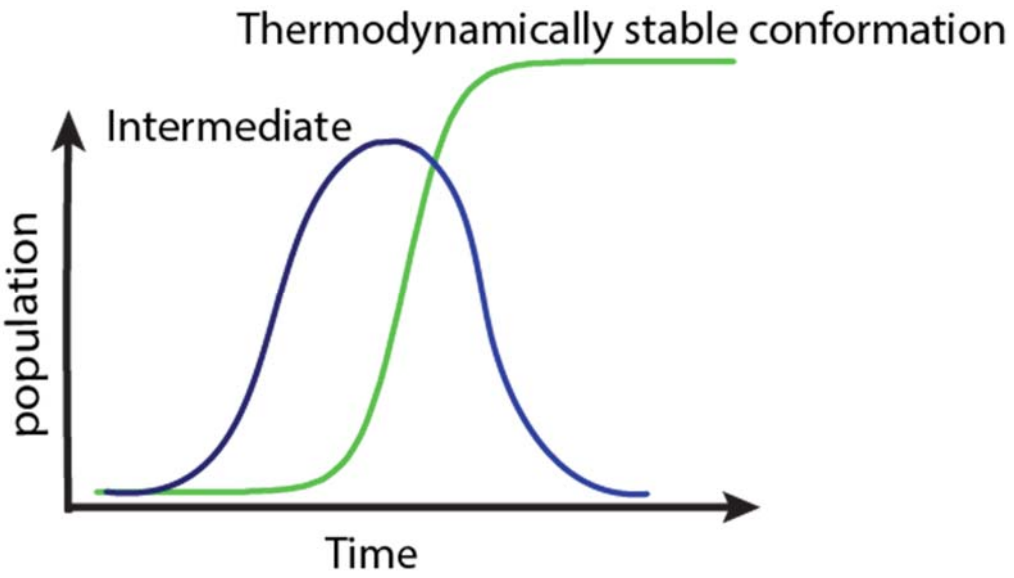

Figure 1-8. The conformational evolution of amyloid self-assembly.
Blue line represents species with lower activation barrier therefore forms first. A second species could emerge in the middle of the assembly process possesses higher thermostability. The thermodynamically stable conformation eventually assimilates the kinetic intermediate and dominates the assembly.

Intermediates in the oligomer state

Extensive studies have been conducted on amyloid oligomers, yet only a few structural results are shown because these intermediates are transient, polymorphic, and dynamic. From a nucleation dependent perspective, the structure within the particle should be the same as the final confirmation and some studies support this assertion. A study on Aβ (1-40) revealed the same crystalline structure reveals that although the nuclei within the oligomer are smaller in scale, their basic molecular position and orientation are identical with the stable conformation. [38]

However, many studies report the structure of oligomer differ from fibers, and even within oligomers, structural transitions can occur, and different types of oligomers, commonly categorized as pre-fibrillar oligomers or non-fibrillar oligomers, fibrillar oligomers and angular

prefibrillar oligomers that have different affinity to different conformational dependent antibodies. Antibody A11 binds to pre-fibrillar oligomers formed by various amyloidogenic peptides, but don't bind to mature fibers, suggesting a common structural domain in oligomers which is absent in mature fibers.[39] Antibody OC binds to fibrillar oligomers that contain fiber nuclei and mature fiber, but not to prefibrillar oligomers or random coils [40]. Overtime prefibrillar oligomers shift into fibrillar oligiomers.[41]The fibrillar oligomer is reported to be proteinase K resistant and possesses higher toxicity in α-Synuclein.

While these antibodies could different structural elements on surface, IR analyses also revealed intermediary β-sheet structures early in assembly for Aβ peptides, yet no detailed structural models have been provided. [42] Interestingly, the majority IR studies suggested anti-parallel beta-sheet forming within oligomers, [42] a result later substantiated by several ssNMR structural studies introduced below. Anti-parallel beta-sheet has been reported to possess higher toxicity in multiple cases in including HET-s, BAM and amyloid β peptides.[43-46]

Further solid-state NMR studies have further supported the structure of oligomers contain transient structures with distinct conformation from mature fibers. The Aβ(1-42) peptide from Alzheimer's disease exists as a hairpin structure spanning from V18 to G33, establishing that both parallel and anti-parallel orientation forms early on. This segment later transitioned to purely parallel β-sheet within mature fibers (**Figure 1-9**). An engineered disulfide mutant (L17C, L34C) could trap the intermediate permanently at oligomer state, this oligomer is recognized by the same conformational specific antibody that binds WT oligomers. [47]

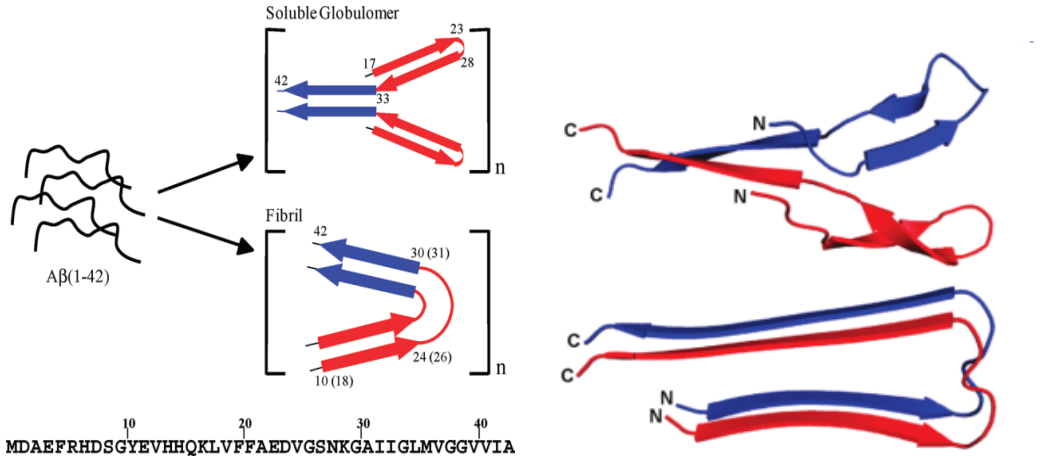

Figure 1-9. The structure of Intermediate and final structure of Aβ (1-42). The left shows the alignment of resides, the right graph shows the general conformation.[47]

Similarly, Aβ (1-40) also forms s hairpin before forming parallel, in register fibers, and again di-sulfide bond anchored beta-hairpin only forms stable [45]oligomer but not fibers(**Figure 1-10**)[45,48].

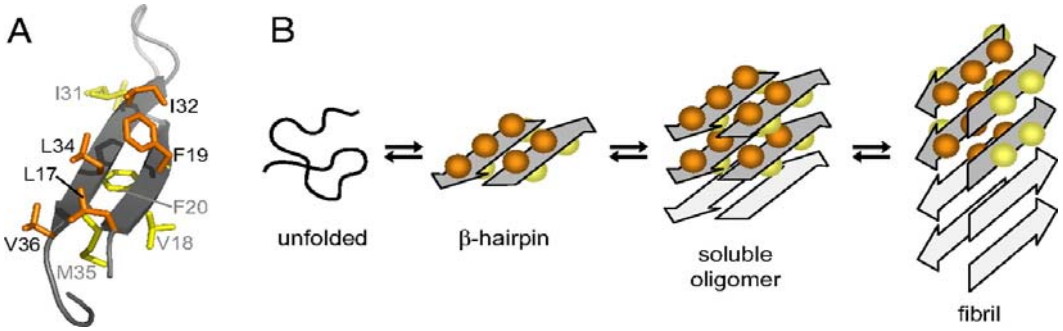

Figure 1-10. (**A**) The structure of Aβ（1-40）oligomers. (**B**) The structural transition from monomer to fiber.[48]

Similar study conducted by Scheidt et.al reveals intramolecular Glu22 and Ile 31 interaction only exist in Aβ(1-40) oligomers and protofibers but not within mature fibers, suggesting a

significant structural re-arrangement from an intermediate state to mature fibers (**Figure 1-11**).[49]

Figure 1-11. The structure of Aβ(1-40) intermediate(A) and mature fiber (B). Glu 22 and Ile 31 were highlighted. [49]

Many studies suggested that the oligomers have higher toxicity, and numerous reasons may account for it, including structural differences. Ahmed et.al studied Aβ (1-42) using solid state NMR, and revealed that oligomers (**Figure 1-12 B**) are pentamers (**Figure 1-12 C**) that possess a three turn structure centered at Leu17-Ala 21, Ile31-Val36 and the C-terminus; within mature fibers the C-terminus residues are extended (**Figure 1-12 A**). The β-turn region could pre-order the upcoming monomers to form parallel β-sheets, then the rest of resides extend out and form stable parallel β-sheets (**Figure 1-12 D,E**). [46]

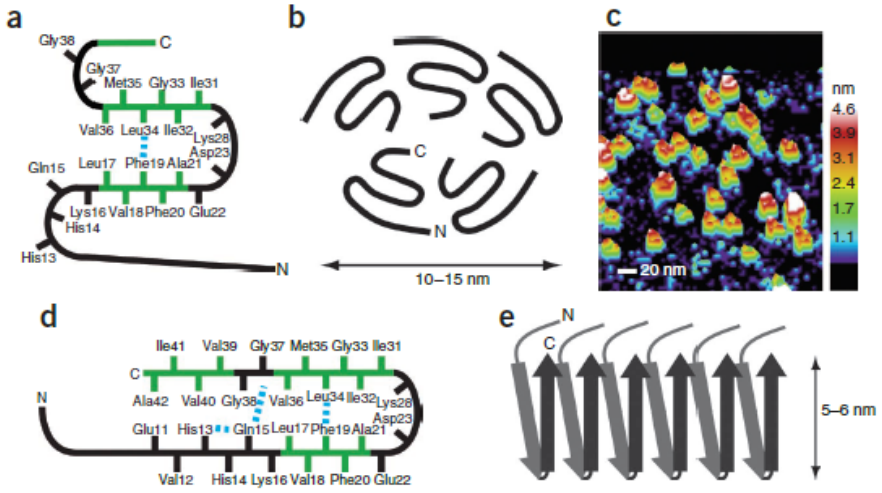

Figure 1-12. Molecular structure of Aβ (1-42) at (**A**) intermediate state. (**B**)Scheme of the pentamer and (**C**) 3D AFM image of oligomers.(**D**)structure and (**E**) scheme of mature fiber[46]

Intermediates beyond oligomer state

The transient oligomer state intermediates have several characteristic features, including weak Thioflavin (ThT) signal.[50] The environment within the oligomer is reported to be different than in solution, with a higher peptide concentration making it easier to preserve structures such as β-turns. Environmental changes have been used to prolong the lifetime of the metastable oligomers, and in other cases, the intermediates prove to be stable. If the intermediates' life time is long enough, the polymorphism phenomenon would emerge. Mechanisms for monitoring this polymorphic transition from metastable intermediates to other structure are much needed at this point.

Different mechanisms of conformational transition

Simultaneous formation

The nuclei of both transient intermediate (nuclei T) and the thermodynamically stable structure (nuclei S) can both exist within initial nucleation phase. Study on D23N Aβ (1-40) reveals an anti-parallel to parallel transition.[51] Unlike the case of polymorphism where different structures co-exist, the anti-parallel intermediate of Aβ (1-40) D23N is metastable and cannot elongate as effective as parallel conformation.

However, the nuclei S does not always form at the beginning of assembly, and only emerges after the intermediate. One of the mechanisms for sequential nucleation is secondary nucleation where the surface of the growing fiber serves as a surface for the nucleation of new nuclei. Jeong et.al revealed the structural transitions along amyloid pathway, occur mainly through secondary nucleation where the surface of an existing fiber can serve as a nucleation site for fibers to nucleate, generating an additional branch or allowing alignment of oligomers to form thicker fibers, [52] the former results in branching of fibers, and the latter results in fibers with wider widths. From the simple dipeptide, FF assemble as intermediate fibers before the final tube is selected as the thermodynamically stable product. The mechanism has been proposed to be secondary nucleation as trapping a droplet suppresses tube emergence.[53]

The alternative mechanism for conformational evolution is mutation. Peptide Aβ(16-22)E22Q, first forms anti-parallel out-of-register ribbons which grows in the particle and later transitioned into parallel fibers as the thermodynamically stable structure. Here nuclei S is formed as a result of "mismatch" between the template and incoming peptide, [54]due to the higher cross-strand Q track stability, the intermediates are completely dissolved and re-incorporated into the fiber.

However, for this mutation model, the intermediate does not always end up being converted into the thermodynamically stable confirmation. In the study conducted by Watanabe-Nakayama et.al of Aβ (1-42), amyloid switch morphology during elongation is observable by optical methods such as TEM or AFM.[55] The mutations occur along elongation and both spiral fiber (open circle) and straight fiber (closed circle) co-exist within the same fiber.

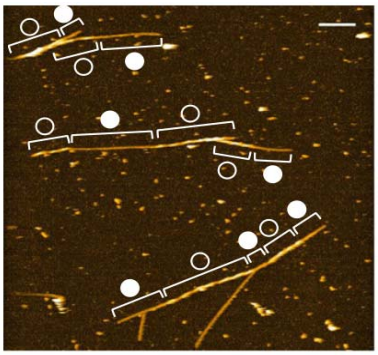

Figure 1-13. Different conformation exist within the same fiber. Open circles represents with spiral pattern and the closed circles represent straight fibers.[55]

Intermediates, necessary pathway or competitive distraction

Assigning the metastable intermediates as "on" or "off" the folding pathway remains a challenge. Are they a temporary "sink" for monomers or are they necessary intermediary steps for the stable nuclei to form?

The majority of nucleation events may occur in the particle, but not all oligomers are incubators of nucleation and fiber assembly. Study by Lasagna-Reeves, et.al showed that annular protofibers (APF) contained pore-like structures that, under the presence of fibers, did not convert into fibers but instead propagated independently. The data suggests that APF as an off-pathway temporary energy sink for monomers. [56]In addition, a segment of β-sheet forming αB

crystalline (ABC) reveals a cylindrical barrel with anti-parallel out-of-register strand orientation, termed cylindrin at the oligomer phase. [57] Such structures as intermediates are common for β-sheet forming peptides. Simulation and AFM studies revealed the mechanism of their toxicity could be membrane penetration. [58-60] Molecular dynamics simulation reveals the transition from out-of-register barrel to in-register fiber requires a complete disassociation and re-association of monomers, meaning the intermediate is an off-pathway product. [57]

On the other hand, intermediates could directly catalyze the formation of thermodynamic product, or in the case of secondary nucleation, serve as the template for fibers to nucleate upon. Therefore, intermediates can be an indispensable part for the formation of the thermodynamically more favored conformation.

Indeed, the β-sheet amyloid mimetic, BAM, reveals anti-parallel out-of-register β-barrel as intermediate or fibers. In BAM, two anti-parallel peptides are covalently attached to the end and the side chains can be modified to favor specific interactions. These BAM monomers first form β-barrel with alternating strong and weak interfaces, and later the weak interface overcomes a small energy barrier to open up and re-close into flat β-sheet, forming anti-parallel out-of-register fibers. [57]Such intermediate appear to be more common for longer peptides as part of the fiber would fold first to assist the folding of other residues. Buchana et.al discovered the FGAIL region of the human islet amyloid polypeptide (hIAPP) would form during the lag phase with parallel β-sheet in a region which later transitioned into partially disordered loop in the fiber. Macrocycles engineered to prevent the formation of parallel β-sheet block fiber

formation, suggesting the intermediate is crucial for the production of thermodynamically stable product.

Currently, no effective medication is available for Alzheimer's disease, and the drug development pipeline for Alzheimer's disease has been described as few candidates and frequent failures[61]. The recent failure of Eli Lillys' experimental drug solanezumab [62]again points out that our fundamental understanding of amyloid's behavior and the design strategy needs to be reconsidered. Current drug targets for Alzheimer's disease aims to remove or prevent β-amyloid accumulation by focusing on the reduction of amyloid β generation, such as β and γ-secretaase inhibitor, and reduction of pre-formed amyloid deposits with antibodies[63,64]. However, none of these methods led to effective therapeutics. Citing from the CEO of Eli Lilly said "No drug so far has been able to demonstrate that removing or preventing the amyloid plaque leads to a release of symptom".

These results raise doubt about the amyloid hypothesis as a result, but these design strategies treat amyloid beta as a generic and static entity. The reduction of amyloid beta by targeting enzymes could lead to impairment of normal neural functions and antibody treatments ignore the polymorphic and evolving nature of amyloid assembly. **Figure 1-14** summarizes three generations of assembly models, extending our current understanding of amyloid assembly.

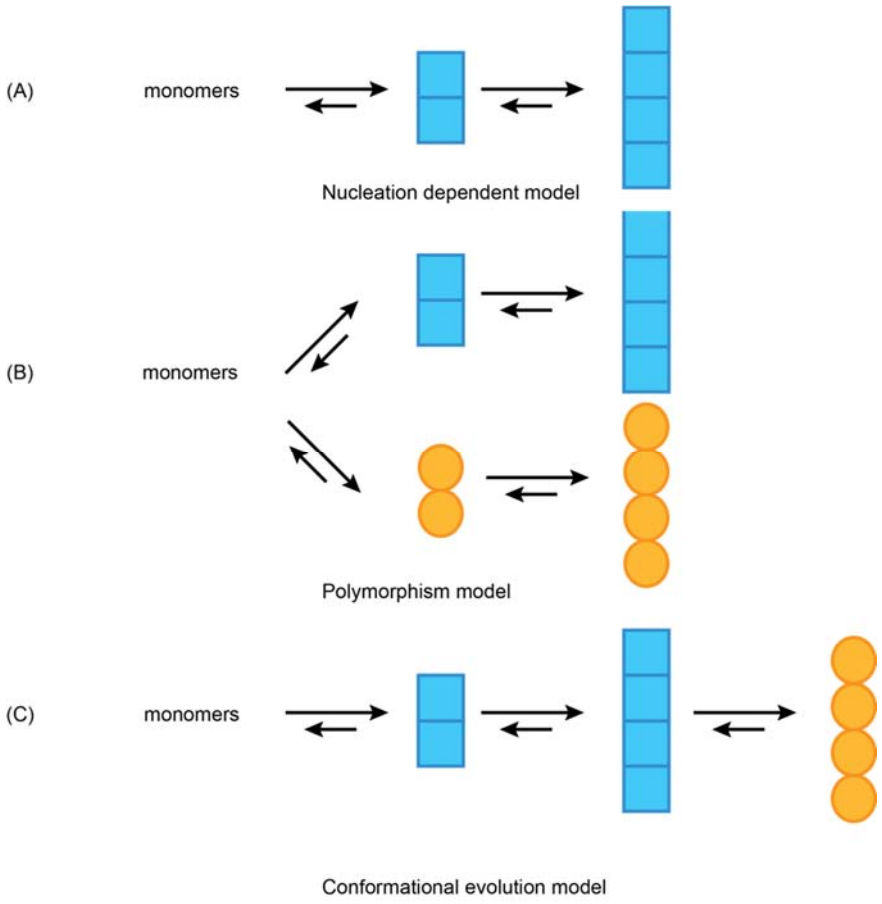

Figure 1-14. Overview of three models of assembly. (**A**) Nucleation dependent self-assembly defines the initial nucleation phase as pure determinant of the amyloid conformation and amyloid replication is simply a faithful replication of the nucleus structure. (**B**). Polymorphism model realized the same sequence could assembly into different conformations with equivalent thermostability and these different conformations can both exist for extended periods of time. (**C**) Conformational evolution model argues amyloid can change conformation during the assembly process. A kinetic intermediate could appear first, and replaced by a thermodynamically favorable conformation that emerged later in the assembly process.

This dissertation focuses on discussing the self-evolving conformations of amyloid and how both intrinsic and extrinsic factors might impact the kinetics and structure of amyloid. Methodologies are developed with solid-state NMR and isotope edited infrared spectroscopy to quantitatively monitor the process. This study extends our current understanding of the assembly process and reveals design strategy for more effective therapeutics.

References

(1) Fowler, D. M.; Koulov, A. V.; Balch, W. E.; Kelly, J. W. Functional amyloid--from bacteria to humans. Trends Biochem Sci 2007, 32, 217-224.

(2) Fitzpatrick, A. W.; Debelouchina, G. T.; Bayro, M. J.; Clare, D. K.; Caporini, M. A.; Bajaj, V. S.; Jaroniec, C. P.; Wang, L.; Ladizhansky, V.; Muller, S. A.; MacPhee, C. E.; Waudby, C. A.; Mott, H. R.; De Simone, A.; Knowles, T. P.; Saibil, H. R.; Vendruscolo, M.; Orlova, E. V.; Griffin, R. G.; Dobson, C. M. Atomic structure and hierarchical assembly of a cross-beta amyloid fibril. Proc Natl Acad Sci U S A 2013, 110, 5468-5473.

(3) Lynn, D.; Burrows, C.; Goodwin, J.; Mehta, A. Origins of chemical evolution. Acc Chem Res 2012, 45, 2023-2024.

(4) Issac, R.; Chmielewski, J. Approaching exponential growth with a self-replicating peptide. J Am Chem Soc 2002, 124, 6808-6809.

(5) Childers, W. S., Mehta, A.K., Bui, T.Q., Liang, Y. and Lynn, D.G. Toward intelligent materials. Molecular Self-Assembly: Advances and Applications 2012, 1.

(6) Childers, W. S.; Ni, R.; Mehta, A. K.; Lynn, D. G. Peptide membranes in chemical evolution. Curr Opin Chem Biol 2009, 13, 652-659.

(7) Boke, E.; Ruer, M.; Wuhr, M.; Coughlin, M.; Lemaitre, R.; Gygi, S. P.; Alberti, S.; Drechsel, D.; Hyman, A. A.; Mitchison, T. J. Amyloid-like Self-Assembly of a Cellular Compartment. Cell 2016, 166, 637-650.

(8) Egel, R.; Lankenau, D.-H.; Mulkidjanian, A. Y.: Origins of life : the primal self-

organization; Springer: Heidelberg, 2011.

(9) Marshall, K. E.; Vadukul, D. M.; Dahal, L.; Theisen, A.; Fowler, M. W.; Al-Hilaly, Y.; Ford, L.; Kemenes, G.; Day, I. J.; Staras, K.; Serpell, L. C. A critical role for the self-assembly of Amyloid-beta 1-42 in neurodegeneration. Sci Rep-Uk 2016, 6.

(10) Aguzzi, A.; Baumann, F.; Bremer, J. The prion's elusive reason for being. Annu Rev Neurosci 2008, 31, 439-477.

(11) Tkachenko, A. V.; Maslov, S. Spontaneous emergence of autocatalytic information-coding polymers. J Chem Phys 2015, 143, 045102.

(12) Chernoff, Y. O. Amyloidogenic domains, prions and structural inheritance: rudiments of early life or recent acquisition? Curr Opin Chem Biol 2004, 8, 665-671.

(13) Sanders, David W.; Kaufman, Sarah K.; Holmes, Brandon B.; Diamond, Marc I. Prions and Protein Assemblies that Convey Biological Information in Health and Disease. Neuron 2016, 89, 433-448.

(14) Chiti, F.; Dobson, C. M. Protein misfolding, functional amyloid, and human disease. Annu Rev Biochem 2006, 75, 333-366.

(15) Jucker, M.; Walker, L. C. Self-propagation of pathogenic protein aggregates in neurodegenerative diseases. Nature 2013, 501, 45-51.

(16) Carrillo-Mora, P.; Luna, R.; Colin-Barenque, L. Amyloid Beta: Multiple Mechanisms of Toxicity and Only Some Protective Effects? Oxid Med Cell Longev 2014.

(17) Liu, T. Y.; Bitan, G. Modulating Self-Assembly of Amyloidogenic Proteins as a Therapeutic Approach for Neurodegenerative Diseases: Strategies and Mechanisms. Chemmedchem 2012, 7, 359-374.

(18) Wang, J.; Liu, K.; Xing, R.; Yan, X. Peptide self-assembly: thermodynamics and kinetics. Chem Soc Rev 2016, 45, 5589-5604.

(19) Zhao, X. B.; Pan, F.; Lu, J. R. Recent development of peptide self-assembly. Prog Nat Sci 2008, 18, 653-660.

(20) Jacob, R. S.; Ghosh, D.; Singh, P. K.; Basu, S. K.; Jha, N. N.; Das, S.; Sukul, P. K.; Patil, S.; Sathaye, S.; Kumar, A.; Chowdhury, A.; Malik, S.; Sen, S.; Maji, S. K. Self healing hydrogels composed of amyloid nano fibrils for cell culture and stem cell differentiation. Biomaterials 2015, 54, 97-105.

(21) Loo, Y. H.; Lakshmanan, A.; Ni, M.; Toh, L. L.; Wang, S.; Hauser, C. A. E. Peptide Bioink: Self-Assembling Nanofibrous Scaffolds for Three-Dimensional Organotypic Cultures. Nano Letters 2015, 15, 6919-6925.

(22) Pan, Y. X.; Cong, H. P.; Men, Y. L.; Xin, S.; Sun, Z. Q.; Liu, C. J.; Yu, S. H. Peptide Self-Assembled Biofilm with Unique Electron Transfer Flexibility for Highly Efficient Visible-Light-Driven Photocatalysis. ACS Nano 2015, 9, 11258-11265.

(23) Eskandari, S.; Guerin, T.; Toth, I.; Stephenson, R. J. Recent advances in self-assembled peptides: Implications for targeted drug delivery and vaccine engineering. Adv Drug Deliv Rev 2016.

(24) Mehta, A. K.; Lu, K.; Childers, W. S.; Liang, Y.; Dublin, S. N.; Dong, J.; Snyder, J. P.; Pingali, S. V.; Thiyagarajan, P.; Lynn, D. G. Facial symmetry in protein self-assembly. J Am Chem Soc 2008, 130, 9829-9835.

(25) Sawaya, M. R.; Sambashivan, S.; Nelson, R.; Ivanova, M. I.; Sievers, S. A.; Apostol, M. I.; Thompson, M. J.; Balbirnie, M.; Wiltzius, J. J.; McFarlane, H. T.; Madsen, A. O.; Riekel,

C.; Eisenberg, D. Atomic structures of amyloid cross-beta spines reveal varied steric zippers. Nature 2007, 447, 453-457.

(26) Eichner, T.; Radford, S. E. A diversity of assembly mechanisms of a generic amyloid fold. Mol Cell 2011, 43, 8-18.

(27) Eisele, Y. S.; Obermuller, U.; Heilbronner, G.; Baumann, F.; Kaeser, S. A.; Wolburg, H.; Walker, L. C.; Staufenbiel, M.; Heikenwalder, M.; Jucker, M. Peripherally applied Abeta-containing inoculates induce cerebral beta-amyloidosis. Science 2010, 330, 980-982.

(28)Rosen, R. F.; Fritz, J. J.; Dooyema, J.; Cintron, A. F.; Hamaguchi, T.; Lah, J. J.; LeVine, H., 3rd; Jucker, M.; Walker, L. C. Exogenous seeding of cerebral beta-amyloid deposition in betaAPP-transgenic rats. J Neurochem 2012, 120, 660-666.

(29) Rohrig, U. F.; Laio, A.; Tantalo, N.; Parrinello, M.; Petronzio, R. Stability and structure of oligomers of the Alzheimer peptide Abeta16-22: from the dimer to the 32-mer. Biophys J 2006, 91, 3217-3229.

(30) Lam, B.; Masellis, M.; Freedman, M.; Stuss, D. T.; Black, S. E. Clinical, imaging, and pathological heterogeneity of the Alzheimer's disease syndrome. Alzheimers Res Ther 2013, 5, 1.

(31) Bousset, L.; Pieri, L.; Ruiz-Arlandis, G.; Gath, J.; Jensen, P. H.; Habenstein, B.; Madiona, K.; Olieric, V.; Bockmann, A.; Meier, B. H.; Melki, R. Structural and functional characterization of two alpha-synuclein strains. Nat Commun 2013, 4, 2575.

(32) Qiang, W.; Kelley, K.; Tycko, R. Polymorph-specific kinetics and thermodynamics of beta-amyloid fibril growth. J Am Chem Soc 2013, 135, 6860-6871.

(33) Tycko, R. Amyloid polymorphism: structural basis and neurobiological relevance.

Neuron 2015, 86, 632-645.

(34) Korevaar, P. A.; Newcomb, C. J.; Meijer, E. W.; Stupp, S. I. Pathway Selection in Peptide Amphiphile Assembly. Journal of the American Chemical Society 2014, 136, 8540-8543.

(35) Chimon, S.; Shaibat, M. A.; Jones, C. R.; Calero, D. C.; Aizezi, B.; Ishii, Y. Evidence of fibril-like beta-sheet structures in a neurotoxic amyloid intermediate of Alzheimer's beta-amyloid. Nature Structural & Molecular Biology 2007, 14, 1157-1164.

(36) Kayed, R.; Head, E.; Thompson, J. L.; McIntire, T. M.; Milton, S. C.; Cotman, C. W.; Glabe, C. G. Common structure of soluble amyloid oligomers implies common mechanism of pathogenesis. Science 2003, 300, 486-489.

(37) Kayed, R.; Head, E.; Sarsoza, F.; Saing, T.; Cotman, C. W.; Necula, M.; Margol, L.; Wu, J.; Breydo, L.; Thompson, J. L.; Rasool, S.; Gurlo, T.; Butler, P.; Glabe, C. G. Fibril specific, conformation dependent antibodies recognize a generic epitope common to amyloid fibrils and fibrillar oligomers that is absent in prefibrillar oligomers. Mol Neurodegener 2007, 2, 18.

(38) Tomic, J. L.; Pensalfini, A.; Head, E.; Glabe, C. G. Soluble fibrillar oligomer levels are elevated in Alzheimer's disease brain and correlate with cognitive dysfunction. Neurobiol Dis 2009, 35, 352-358.

(39) Cerf, E.; Sarroukh, R.; Tamamizu-Kato, S.; Breydo, L.; Derclaye, S.; Dufrene, Y. F.; Narayanaswami, V.; Goormaghtigh, E.; Ruysschaert, J. M.; Raussens, V. Antiparallel beta-sheet: a signature structure of the oligomeric amyloid beta-peptide. Biochem J 2009, 421, 415-423.

(40) Berthelot, K.; Ta, H. P.; Gean, J.; Lecomte, S.; Cullin, C. In vivo and in vitro analyses of toxic mutants of HET-s: FTIR antiparallel signature correlates with amyloid toxicity. J Mol

Biol 2011, 412, 137-152.

(41) Liu, C.; Zhao, M.; Jiang, L.; Cheng, P. N.; Park, J.; Sawaya, M. R.; Pensalfini, A.; Gou, D.; Berk, A. J.; Glabe, C. G.; Nowick, J.; Eisenberg, D. Out-of-register beta-sheets suggest a pathway to toxic amyloid aggregates. Proc Natl Acad Sci U S A 2012, 109, 20913-20918.

(42) Sandberg, A.; Luheshi, L. M.; Sollvander, S.; Pereira de Barros, T.; Macao, B.; Knowles, T. P.; Biverstal, H.; Lendel, C.; Ekholm-Petterson, F.; Dubnovitsky, A.; Lannfelt, L.; Dobson, C. M.; Hard, T. Stabilization of neurotoxic Alzheimer amyloid-beta oligomers by protein engineering. Proc Natl Acad Sci U S A 2010, 107, 15595-15600.

(43) Ahmed, M.; Davis, J.; Aucoin, D.; Sato, T.; Ahuja, S.; Aimoto, S.; Elliott, J. I.; Van Nostrand, W. E.; Smith, S. O. Structural conversion of neurotoxic amyloid-beta(1-42) oligomers to fibrils. Nat Struct Mol Biol 2010, 17, 561-567.

(44) Yu, L.; Edalji, R.; Harlan, J. E.; Holzman, T. F.; Lopez, A. P.; Labkovsky, B.; Hillen, H.; Barghorn, S.; Ebert, U.; Richardson, P. L.; Miesbauer, L.; Solomon, L.; Bartley, D.; Walter, K.; Johnson, R. W.; Hajduk, P. J.; Olejniczak, E. T. Structural characterization of a soluble amyloid beta-peptide oligomer. Biochemistry 2009, 48, 1870-1877.

(45) Hoyer, W.; Gronwall, C.; Jonsson, A.; Stahl, S.; Hard, T. Stabilization of a beta-hairpin in monomeric Alzheimer's amyloid-beta peptide inhibits amyloid formation. Proc Natl Acad Sci U S A 2008, 105, 5099-5104.

(46) Scheidt, H. A.; Morgado, I.; Huster, D. Solid-state NMR Reveals a Close Structural Relationship between Amyloid-beta Protofibrils and Oligomers. Journal of Biological Chemistry 2012, 287, 22822-22826.

(47) Kotler, S. A.; Brender, J. R.; Vivekanandan, S.; Suzuki, Y.; Yamamoto, K.; Monette,

M.; Krishnamoorthy, J.; Walsh, P.; Cauble, M.; Holl, M. M.; Marsh, E. N.; Ramamoorthy, A. High-resolution NMR characterization of low abundance oligomers of amyloid-beta without purification. Sci Rep 2015, 5, 11811.

(48) Qiang, W.; Yau, W. M.; Luo, Y. Q.; Mattson, M. P.; Tycko, R. Antiparallel beta-sheet architecture in Iowa-mutant beta-amyloid fibrils. P Natl Acad Sci USA 2012, 109, 4443-4448.

(49) Jeong, J. S.; Ansaloni, A.; Mezzenga, R.; Lashuel, H. A.; Dietler, G. Novel mechanistic insight into the molecular basis of amyloid polymorphism and secondary nucleation during amyloid formation. J Mol Biol 2013, 425, 1765-1781.

(50) Levin, A.; Mason, T. O.; Adler-Abramovich, L.; Buell, A. K.; Meisl, G.; Galvagnion, C.; Bram, Y.; Stratford, S. A.; Dobson, C. M.; Knowles, T. P.; Gazit, E. Ostwald's rule of stages governs structural transitions and morphology of dipeptide supramolecular polymers. Nat Commun 2014, 5, 5219.

(51) Liang, C.; Ni, R.; Smith, J. E.; Childers, W. S.; Mehta, A. K.; Lynn, D. G. Kinetic intermediates in amyloid assembly. J Am Chem Soc 2014, 136, 15146-15149.

(52) Watanabe-Nakayama, T.; Ono, K.; Itami, M.; Takahashi, R.; Teplow, D. B.; Yamada, M. High-speed atomic force microscopy reveals structural dynamics of amyloid beta1-42 aggregates. Proc Natl Acad Sci U S A 2016, 113, 5835-5840.

(53) Lasagna-Reeves, C. A.; Glabe, C. G.; Kayed, R. Amyloid-beta annular protofibrils evade fibrillar fate in Alzheimer disease brain. J Biol Chem 2011, 286, 22122-22130.

(54) Laganowsky, A.; Liu, C.; Sawaya, M. R.; Whitelegge, J. P.; Park, J.; Zhao, M.; Pensalfini, A.; Soriaga, A. B.; Landau, M.; Teng, P. K.; Cascio, D.; Glabe, C.; Eisenberg, D. Atomic view of a toxic amyloid small oligomer. Science 2012, 335, 1228-1231.

(55) De Simone, A.; Derreumaux, P. Low molecular weight oligomers of amyloid peptides display beta-barrel conformations: a replica exchange molecular dynamics study in explicit solvent. J Chem Phys 2010, 132, 165103.

(56) Jang, H.; Arce, F. T.; Ramachandran, S.; Capone, R.; Lal, R.; Nussinov, R. (AFM reveal pore formaiton)beta-Barrel topology of Alzheimer's beta-amyloid ion channels. J Mol Biol 2010, 404, 917-934.

(57) Quist, A.; Doudevski, I.; Lin, H.; Azimova, R.; Ng, D.; Frangione, B.; Kagan, B.; Ghiso, J.; Lal, R. (AFM of ion channel in all diff peptides)Amyloid ion channels: a common structural link for protein-misfolding disease. Proc Natl Acad Sci U S A 2005, 102, 10427-10432.

(58) Cummings, J. L.; Morstorf, T.; Zhong, K. Alzheimer's disease drug-development pipeline: few candidates, frequent failures. Alzheimers Research & Therapy 2014, 6.

(59) Belluck, P. Eli Lilly's experimental Alzheimer's drug fails in long trail. The New York Times 2016.

(60) Davies, P.; Koppel, J. Mechanism-based treatments for Alzheimer's disease. Dialogues Clin Neurosci 2009, 11, 159-169.

(61) Grill, J. D.; Cummings, J. L. Current therapeutic targets for the treatment of Alzheimer's disease. Expert Rev Neurother 2010, 10, 711-728.

Chapter 2. Defining conformational distribution of cross-β peptide assembly using isotope edited infrared spectroscopy

Background

From previous chapter, it has been confirmed that amyloid assembly has access to a variety of conformational diversity that is subject to conformational transitions. Such a process is regulated both by kinetic and thermodynamic factors [1] forming a dynamic conformational network containing β-sheet with different conformations. The eukaryotic cell provides a complex fluid system with complex surfaces and components that is likely to complicate such a transition process, therefore contributes significantly to amyloidogenic diseases. [2]

However, such a transitioning system has been challenging to study due to the properties of the material and limitation of biophysical methods. Attempts have been made to better understand this process, such as 1D[3] and 2D NMR method,[4] homonuclear and heteronuclear NMR[1], electron microscopy[5], crystallography[6],etc. These methods can acquire accurate structural information of amyloid, however, due to freezing in sample preparation and the large quantify of peptides in the sampling process, they are limited to observing evolving systems. Although

experiments such as anti-body binding experiment[7], ThT fluorescence[8] can be used to detect oligomers or analyze the complex systems, they failed to provide any specific regional structural information.

Isotope edited infrared spectroscopy (IE-IR) has been a useful tool to study evolving or polymorphic amyloid system and has been widely applied in the kinetic measurement of conformational change for self-assembly systems. The peak splitting pattern of ^{12}C and ^{13}C peak provides structural insight while allowing fast and multiple sampling of the solution[1,9]. Therefore, IE-IR is a good complementary method combined with solid-state NMR to follow and deconvolute a transitioning self-assembly system. Solid-state NMR provides the precise conformation, establishing basis sets for different conformations and IE-IR spectra can be acquired at various times and later distributed to different conformations.

Isotope edited infrared spectroscopy in the study of amyloid self-assembly

Within β-sheets, extensive arrays of hydrogen bonds are formed between adjacent peptide strands. Due to such formation, local modes (**Figure 2-1, red arrows**) along the carbonyl bonds are coupled, leading to exciton delocalization within the β-sheet, forming the normal modes of the system (**Figure 2-1**).Black arrows along fiber axis appear around 1620-1630cm^{-1} and is signature for β-sheet formation. Blue arrows parallel to peptide strand is the distinguishing factor between anti-parallel and parallel β-sheet. The anti-parallel β-sheet has a small peak around 1690cm^{-1}, which is absent in parallel β-sheet due to cancellation of local modes.

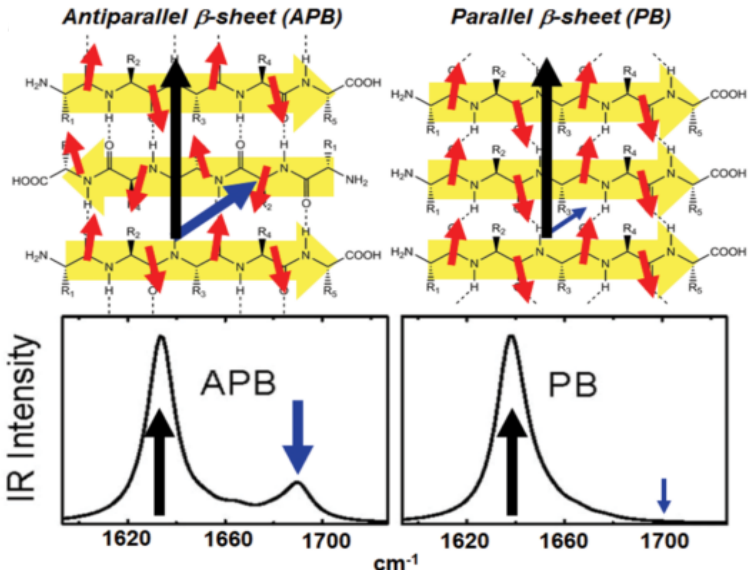

Figure 2-1. Amide I mode of anti-parallel and parallel β-sheet.
The red arrow represents normal modes generated by local carbonyls, the black and blue arrow signifies local modes generated as a result of vibrational coupling. The anti-parallel β-sheet has a small band around 1690cm^{-1} indicated by blue arrow. [10]

These signals are useful for differentiating different secondary strucutres yet limited for distinguishing between various types of β-sheets such as anti-parallel in-registery vs out-of-registery β-sheets. The introduction of $^{13}C=O$ isotope at a single amino acid provides significantly more rich information on molecular configuration. With the introduction of carbon C^{13} on C1 position of amino acid, an additional ^{13}C band appears and red-shifted to around 30 wave numbers relative to the rest of the ^{12}C band due to larger molecular weight. Meanwhile, the ^{12}C band is shifted to higher wavenumber due to the interruption of coupling between $^{12}C=O$ carbonyls. The comparison between natural abundance and enriched [1-^{13}C]F19 Aβ(16-22) Ac-KLVFFAQ-NH_2 is shown below(**Figure 2-2**).

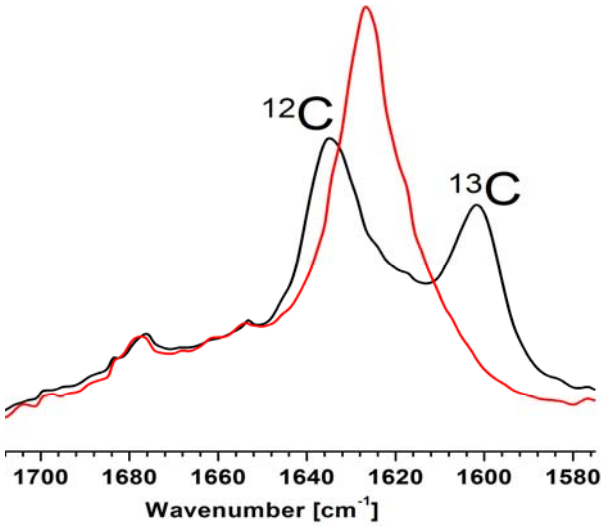

Figure 2-2. The comparison for IR signal of enriched (black) and non-enriched (red) Aβ (16-22). The enriched IE-IR has two bands; one around 1630cm^{-1} comes from interrupted ^{12}C carbonyls, the one around 1600cm^{-1} results from enriched carbonyl.

With the help of IE-IR fitting using mathematica, we can combine the accuracy of solid state NMR with the rapid data acquisition of IR spectroscopy to analyze the transitioning polymorphic amyloid self-assembling systems, by mapping out conformational phylogeny and assigning co-efficient to the contribution of different conformations. Examples are shown at the end to demonstrate how this method is applied in studying the kinetics and various factors influencing the transitioning self-assembly systems.

Methods

Fibril Assembly: Lyophilized [1-^{13}C]F19 Aβ(16-22), [1-^{13}C]F19 Aβ(16-22)E22Q, and [1-^{13}C]F19 Aβ(16-22)E22QNHCH$_3$ peptides were dissolved in 1,1,1,3,3,3-hexafluoro-2-propanol (HFIP, Sigma) and sonicated for 30 min, then dried under a stream of dry N_2 gas or under

vacuum. The resultant clear film was dissolved in 20% acetonitrile/water (0.1 vol% TFA), bath sonicated for at least 10 min and, unless indicated, incubated at room temperature for assembly. To produce unassembled [1-^{13}C]A (16-22) peptide, lyophilized [1-^{13}C]F19 Aβ(16-22) peptide was dissolved in 1,1,1,3,3,3-hexafluoro-2-propanol (HFIP, Sigma) and sonicated for 30 min and stored at room temperature in HFIP.

Fitting of Isotope-Edited FTIR Spectra: [1-^{13}C]F19 IR spectra were analyzed with Mathematica 10.0[31] with the NonlinearModelFitmodule that allowed for use of a model of the functional form: pC*parafn[x] + apC*antifn[x] + apoC*antiOutfn[x] + uC*unassemfn[x] + rC*ribbonfn[x], where pC, apC, apoC, uC and rC are scaling coefficients for the individual reference spectra.Although the fits are a linear combination of basis set spectra, the NonlinearModelFitmodule allowed for use of spectra that were interpolated as a function corresponding to the range from 1575 cm^{-1} to 1718 cm$^{-1.}$ In the fits, scaling coefficients were constrained to be ≥ 0.

Attenuated Total Reflectance Fourier Transform Infrared (AT-FTIR): Aliquots (10μL) of peptide solution were dried as thin films on an Pike GaldiATR (Madison, WI, USA) ATR diamond crystal. FT-IR spectra were acquired using a Jasco FT-IR 4100 (Easton, MD, USA) at room temperature and averaging 500 to 800 scans with 2 cm^{-1} resolution, using either an MCT or TGS detector, 5mm aperture and a scanning speed of 4mm/sec. Spectra were processed with zero-filling and a cosine apodization function. IE-IR spectra were normalized to the peak height of the ^{12}C band.

Transmission Electron Microscopy (TEM): A TEM copper grid with a 200 mesh carbon Support (Electron Microscopy Sciences) was covered with 10 μL of a diluted peptide solution (0.05 mM to 0.1 mM) for 1 min before wicking the excess solution with filter paper. 10 μL of the staining solution (2% uranyl acetate, Sigma-Aldrich or methylamine tungstate, Ted Pella, Inc) was added and incubated for 2 min, excess solution was wicked away, and the grids were placed in desiccators to dry under vacuum overnight.

Results

Experimental data of basis sets of various β-sheet conformations

Previously, our lab experimentally established basis sets for different Aβ(16-22)congeners with anti-parallel in-registery, anti-parallel out-of-registery[11], parallel [1]homogenous amyloid assemblies. Aβ (16-22) peptides assemble to homogenous anti-parallel out-of-register nanotubes in pH2, and anti-parallel in register fiber in neutral pH. [11]The congener Aβ (16-22) E22Q stabilized into parallel fibers. IR spectrum of [1-^{13}C]F19 Aβ(16-22) in anti-parallel out-of-register have ^{12}C and ^{13}C splitting of 43cm^{-1}, while anti-parallel in-register have a ^{12}C and ^{13}C splitting of 31 cm^{-1},With a ^{12}C / ^{13}C band intensity for both of 0.9. For [1-^{13}C]F19 Aβ(16-22)E22Q, the ^{12}C and ^{13}C splitting of 33cm^{-1} and ^{12}C / ^{13}C ratio is 1.3.

To complete the sets, the IR spectrum of unassembled peptides were obtained though pre-dissolving the [1-^{13}C]F19 Aβ(16-22) peptide in HFIP and dried on ATR diamond. The broad and low intensity ^{12}C and ^{13}C peaks are consistent with non-ordered peptides without extended vibrational coupling of carbonyl groups (**Figure 2-3, Table 2-1**).

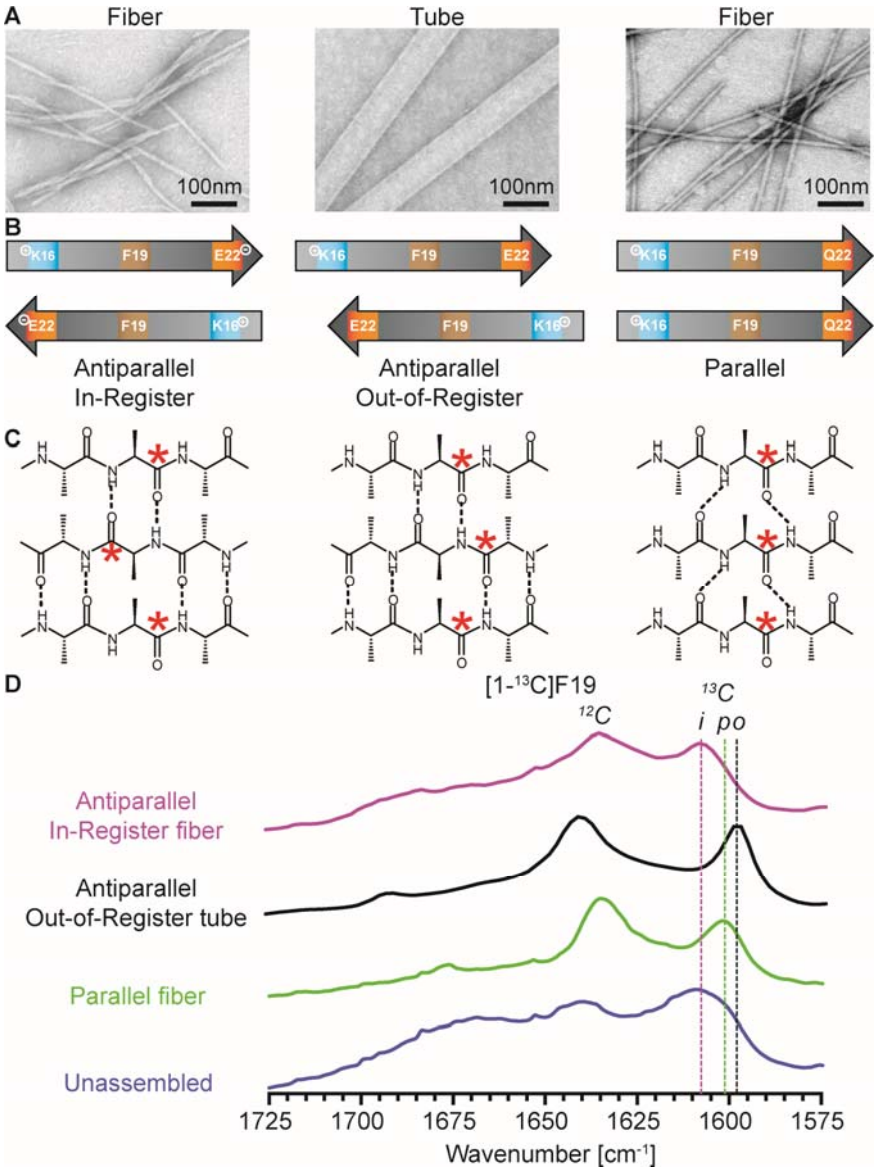

Figure 2-3. Illustration of peptide backbone with [1-^{13}C] F19 (red star) for Aβ(16-22) and its congeners.

(**A**). TEM Aβ(16-22) and its congeners with anti-parallel in-register, out-of-register and parallel strand orientation.

(**B**). Strand orientation of Aβ(16-22) and its congeners with anti-parallel in-register, out-of-register and parallel strand orientation.

(**C**). The alignment of ^{13}C enriched carbonyl when Aβ(16-22) and its congeners possess anti-parallel in-register, out-of-register and parallel strand orientation

(**D**) The IE-IR spectra of Aβ(16-22) and its congeners when assembled into anti-parallel in-register, out-of-register , parallel β-sheets and when unassembled.

Depending on various peptide strand orientation and registration, ^{13}C=O couples differently among the assembled peptide, creating drastically different patterns in their IE-IR spectrum as demonstrated by the ^{12}C/^{13}C peak ratio, peak splitting and ^{13}C peak position with i signifying

anti-parallel in-register, p signifying parallel and o signifying anti-parallel out-of-register β-sheet structure.

Table 2-1. Isotope-edited IR peaks for [1-^{13}C]F19 Aβ(16-22) congeners

Peptide sequence	**Anti-parallel signature [cm^{-1}]**	**Q-side chain [cm^{-1}]**	**^{12}C [cm^{-1}]**	**^{13}C [cm^{-1}]**	**[cm^{-1}]**	**^{12}C/^{13}C peak ratio**	β-strand arrangement determined by NMR
Aβ(16-22) tube	~1693	N/A	1637	1597	40	0.9	anti-parallel out-of-register[12]
Aβ(16-22) fiber	~1693	N/A	1635	1607	28	0.9	anti-parallel in-register[12]
Aβ(16-22)E22Q	N/A	1677	1633.9	1601.4	32.5	1.2	parallel
Aβ(16-22) monomer	N/A	N/A	1640.2	1608.8	31.4	0.85	N/A

The IE-IR spectra of [1-^{13}C]F19 Aβ(16-22) and its congeners during any time point is regarded as a linear combination of various basis sets. Since the absolute concentration of peptides is

inaccessible without more quantities information such as correlation with solid-state NMR, the molar absorptive for each conformation is not extracted. In our study, the signal is all normalized to the ^{12}C amide band intensity. Best fit of a certain data point can be de-convoluted with coefficients corresponding to the abundance of various structures.

The gap at the early stage of assembly

The experimental data of [1-^{13}C]F19 Aβ(16-22)E22Q was fitted into the basis sets using mathematica. However, such method only fits the later stages of assembly but a big gap of the best fit and experimental data exists (**Figure 2-4 A**). The best fit of various conformations could not capture the characteristics of 1hr assembly, especially the height of ^{13}C peak. Additionally, the best fit is blue-shifted compared to the actual data. This gap indicates an unaccounted for species at the beginning of assembly that's absent at the end of assembly.

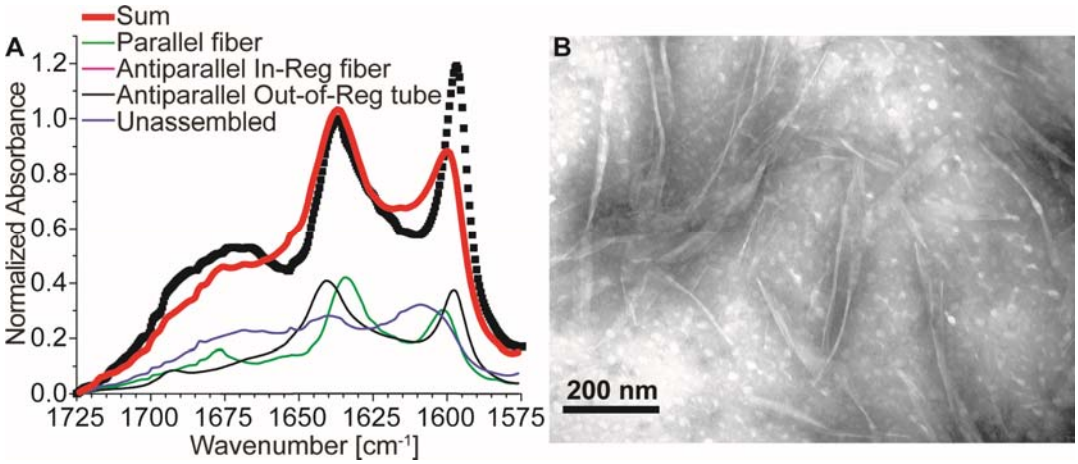

Figure 2-4. (**A**) The comparison between best fit and real data of the IE-IR spectrum of [1-^{13}C]F19 Aβ(16-22)E22Q in 1 hr. (**B**) The TEM of Aβ(16-22)E22Q assembled in 1hr with negative stain.

Defining the early time species

The 1hr Aβ(16-22)E22Q assemblies at room temperature consist of ~23 nm wide thin wispy ribbons and particles (**Figure 2-4B**) as visualized by electron microscopy, similar to populations directly imaged previously with fluorescence[13] and electron microscopy.[14]Prevous simulation works on IR of β-sheet predicted that as the number of β-sheet laminations increase and twist decreaes, IR spectrum blue-shifts[15]. This prediction is consistent with the experimental data of the difference between the 23nm twisted ribbons with an estimate of 12 twisted β-sheets and mature nanotubes with 54nm diameter and around 150 stacked，non-twisted β-sheets.[11,16]

To obtain the spectrum of twisted ribbons, [1-^{13}C]F19 Aβ(16-22) was incubated at 37°C(temperature that traps particle[14]) for 1 day, TEM and IR were taken (**Figure 2-5**). The morphology is similar to E22Q as thin wispy ribbons around 25nm width appeared. The IR spectra also captured the characteristics of 1hr [1-^{13}C]F19 Aβ(16-22)E22Q. The overlap of two spectrums shows identical position and intensity of ^{12}C and ^{13}C bands. The IR spectrum of [1-13C]F19 Aβ(16-22) 37°C IR spectrum was used to obtain the IE-IR spectra of the twisted ribbon at the initial phase of assembly. The 37°C assembly was fit with the 4 existing experimental spectra corresponding the mature , and additional constraint was added that the difference between the resulting fit and the experimental [1-^{13}C]F19 Aβ(16-22)E22Q 37°C spectrum must be positive (**Figure 2-5 C**). The resulting difference, (**Figure 2-5 D**) we hypothesize, corresponds to anti-parallel out-of-register twisted ribbons that emerge from the initial molten globule phase.

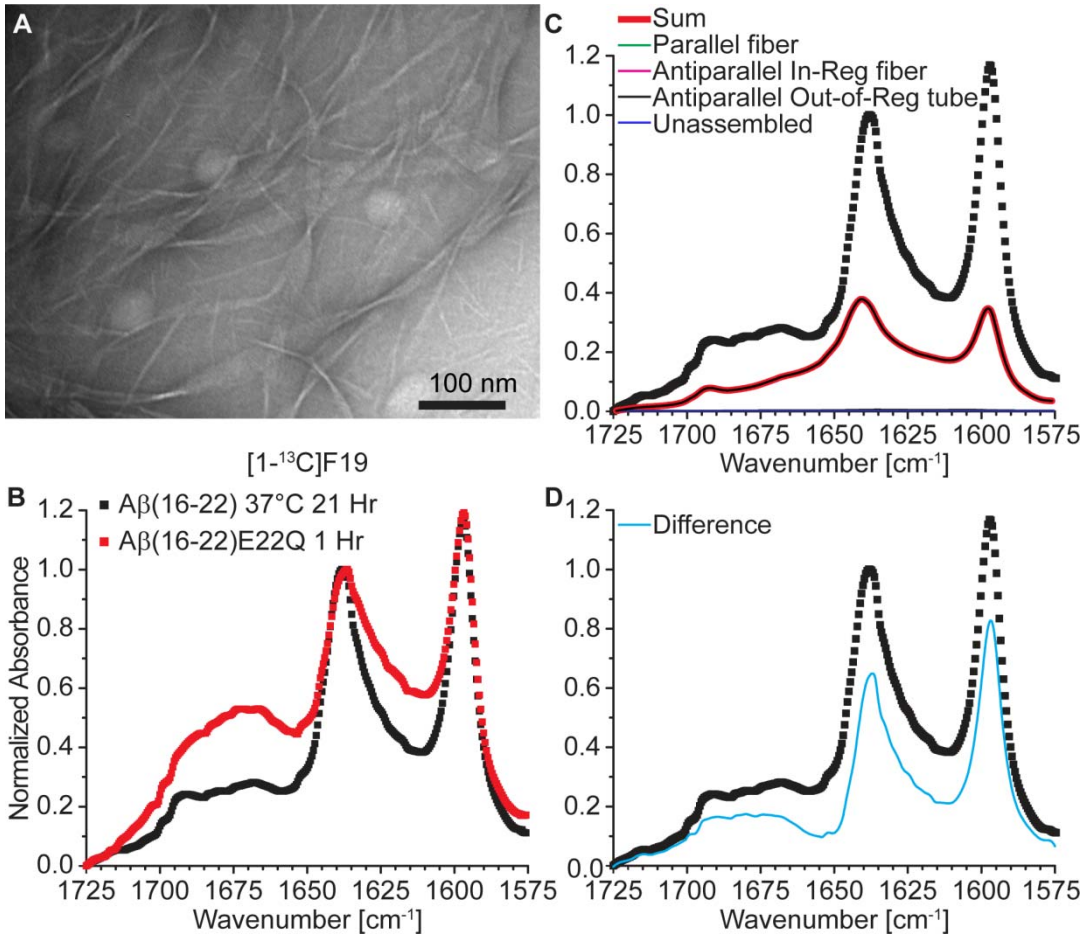

Figure 2-5. Defining the early time species

(**A**) TEM of Aβ(16-22) after 21hr in 37°C.(**B**) IE-IR spectrum of [1-^{13}C]F19 Aβ(16-22) after 21hr in 37°C(red) and [1-^{13}C]F19 Aβ(16-22)E22Q after 1hr in room temperature. Best fit (red line) to 21 hr, 37°C spectrum (black squares) with the constraint that the difference between the experimental is greater than zero. The coefficients for the resulting fit are: parallel = 0±0.20; anti-parallel in-registery = 0±0.19, anti-parallel out-of-registery = 0.38 ± 0.13, unassembled = 0 ± 0.09. (**D**) The difference between the constrained best fit (panel **C**, red line) and experimental data (black squares) resulted in a spectrum (cyan) attributed to the initial twisted ribbon intermediate.

Completion of the basis sets

The incorporation of the anti-parallel out-of-register ribbons from [1-^{13}C] F19 Aβ (16-22) to the IE-IR basis set completes the basis sets for Aβ (16-22) E22Q and its congeners, allowing

for identifying the conformational populations of dynamic self-assembly systems.

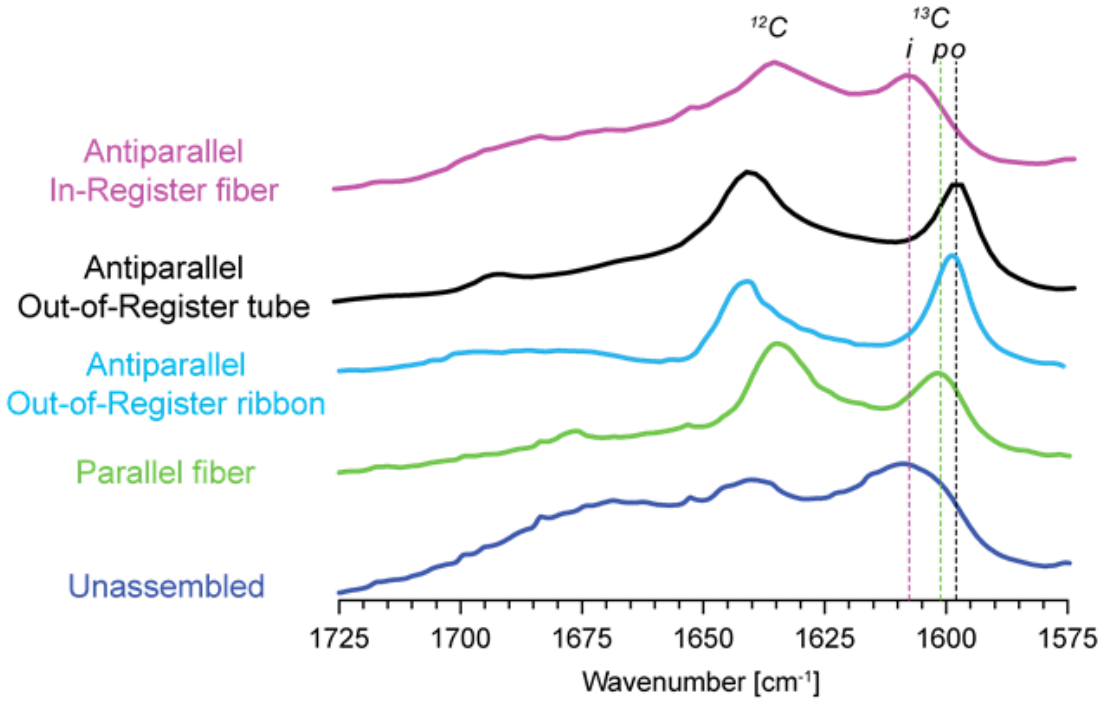

Figure 2-6. Complete basis sets for studying the population change of Aβ(16-22) and its congeners. i,p and o signifies anti-parallel in-registery β-sheet, parallel-β sheet and anti-parallel out-of-registery β-sheet separately.

Conclusion

The establishment of the basis sets for [1-^{13}C]F19 enriched Aβ (16-22) and congeners provides a robust and quick system of studying the dynamic nature of such a complex system. These basis sets allows for the de-convolution of mixed peptide systems with multiple conformations by simply measuring the IR spectrum of the system, then assigning a coefficient for the contribution of different conformations by fitting the IR spectrum into the basis sets.

The complexity of amyloid system is critical for understanding the disease progression especially after studies have shown the relevance of the conformational variation of polymorphs with toxicity[8]. Our method provides a new strategy for defining the conformational population within a polymorphic system. Such a method has the potential to be applied to longer sequences for longer peptides in various amyloidogenic diseases such as Aβ(1-40)[8,17], β2-microglobulin[18], Sup35[19], HAS[20], α-synuclein[17] and lyzozyme[21].

References

(1) Liang, C.; Ni, R.; Smith, J. E.; Childers, W. S.; Mehta, A. K.; Lynn, D. G. Kinetic intermediates in amyloid assembly. *J Am Chem Soc* **2014**, *136*, 15146-15149.

(2) Eichner, T.; Radford, S. E. A diversity of assembly mechanisms of a generic amyloid fold. *Mol Cell* **2011**, *43*, 8-18.

(3) Liu, G.; Gaines, J. C.; Robbins, K. J.; Lazo, N. D. Kinetic profile of amyloid formation in the presence of an aromatic inhibitor by nuclear magnetic resonance. *ACS Med Chem Lett* **2012**, *3*, 856-859.

(4) Tycko, R. Solid-state NMR studies of amyloid fibril structure. *Annu Rev Phys Chem* **2011**, *62*, 279-299.

(5) Smith, J. E.; Liang, C.; Tseng, M.; Li, N.; Li, S.; Mowles, A. K.; Mehta, A. K.; Lynn, D. G. Defining the Dynamic Conformational Networks of Cross- Peptide Assembly. *Isr J Chem* **2015**, *55*, 763-769.

(6) Colletier, J. P.; Laganowsky, A.; Landau, M.; Zhao, M.; Soriaga, A. B.; Goldschmidt,

L.; Flot, D.; Cascio, D.; Sawaya, M. R.; Eisenberg, D. Molecular basis for amyloid-beta polymorphism. *Proc Natl Acad Sci U S A* **2011**, *108*, 16938-16943.

(7) Kayed, R.; Head, E.; Thompson, J. L.; McIntire, T. M.; Milton, S. C.; Cotman, C. W.; Glabe, C. G. Common structure of soluble amyloid oligomers implies common mechanism of pathogenesis. *Science* **2003**, *300*, 486-489.

(8) Meisl, G.; Yang, X.; Hellstrand, E.; Frohm, B.; Kirkegaard, J. B.; Cohen, S. I.; Dobson, C. M.; Linse, S.; Knowles, T. P. Differences in nucleation behavior underlie the contrasting aggregation kinetics of the Abeta40 and Abeta42 peptides. *Proc Natl Acad Sci U S A* **2014**, *111*, 9384-9389.

(9) Petty, S. A.; Decatur, S. M. Intersheet rearrangement of polypeptides during nucleation of {beta}-sheet aggregates. *Proc Natl Acad Sci U S A* **2005**, *102*, 14272-14277.

(10) Moran, S. D.; Zanni, M. T. How to Get Insight into Amyloid Structure and Formation from Infrared Spectroscopy. *J Phys Chem Lett* **2014**, *5*, 1984-1993.

(11) Mehta, A. K.; Lu, K.; Childers, W. S.; Liang, Y.; Dublin, S. N.; Dong, J.; Snyder, J. P.; Pingali, S. V.; Thiyagarajan, P.; Lynn, D. G. Facial symmetry in protein self-assembly. *J Am Chem Soc* **2008**, *130*, 9829-9835.

(12) Mehta, A. K.; Lu, K.; Childers, W. S.; Liang, Y.; Dublin, S. N.; Dong, J.; Snyder, J. P.; Pingali, S. V.; Thiyagarajan, P.; Lynn, D. G. Facial Symmetry in Protein Self-Assembly. *J Am Chem Soc* **2008**, *130*, 9829-9835.

(13) Anthony, N. R.; Mehta, A. K.; Lynn, D. G.; Berland, K. M. Mapping amyloid-beta(16-22) nucleation pathways using fluorescence lifetime imaging microscopy. *Soft Matter* **2014**, *10*, 4162-4172.

(14) Childers, W. S.; Anthony, N. R.; Mehta, A. K.; Berland, K. M.; Lynn, D. G. Phase networks of cross-beta peptide assemblies. *Langmuir* **2012**, *28*, 6386-6395.

(15) Welch, W. R.; Keiderling, T. A.; Kubelka, J. Structural analyses of experimental 13C edited amide I' IR and VCD for peptide beta-sheet aggregates and fibrils using DFT-based spectral simulations. *J Phys Chem B* **2013**, *117*, 10359-10369.

(16) Childers, W. S.; Mehta, A. K.; Lu, K.; Lynn, D. G. Templating molecular arrays in amyloid's cross-beta grooves. *J Am Chem Soc* **2009**, *131*, 10165-10172.

(17) Qiang, W.; Kelley, K.; Tycko, R. Polymorph-specific kinetics and thermodynamics of beta-amyloid fibril growth. *J Am Chem Soc* **2013**, *135*, 6860-6871.

(18) Gosal, W. S.; Morten, I. J.; Hewitt, E. W.; Smith, D. A.; Thomson, N. H.; Radford, S. E. Competing pathways determine fibril morphology in the self-assembly of beta2-microglobulin into amyloid. *J Mol Biol* **2005**, *351*, 850-864.

(19) Serio, T. R.; Cashikar, A. G.; Kowal, A. S.; Sawicki, G. J.; Moslehi, J. J.; Serpell, L.; Arnsdorf, M. F.; Lindquist, S. L. Nucleated conformational conversion and the replication of conformational information by a prion determinant. *Science* **2000**, *289*, 1317-1321.

(20) Juarez, J.; Taboada, P.; Mosquera, V. Existence of different structural intermediates on the fibrillation pathway of human serum albumin. *Biophys J* **2009**, *96*, 2353-2370.

(21) Hill, S. E.; Miti, T.; Richmond, T.; Muschol, M. Spatial extent of charge repulsion regulates assembly pathways for lysozyme amyloid fibrils. *PLoS One* **2011**, *6*, e18171.

Chapter 3. Mapping the kinetic intermediates along amyloid self-assembly

Introduction

Traditionally, amyloid self-assembly process has been categorized into two stages: nucleation and elongation.[1,2] In the nucleation state, amyloid forms molten globules [3] within which a nucleus is formed. The conformation of the nucleus is decided collectively by many factors, such as peptide sequence, charge repulsion, side chain cross-strand paring, etc [4-8]. With the presence of the nucleus as a template, monomers can elongate along the end of the nucleus to form amyloid fibers, replicating the same conformation as the nucleus [1,2,9,10].

However, recent development has suggested the process of self-assembly is of more complexity [11].The first dimension of complexity is introduced as amyloid polymorphism. Under the same environment, peptide with the same sequence can assemble into different conformations and these conformations co-exist. The second dimension of complexity is defined by the dynamic nature of the self-assembly system. Despite the high thermostability of amyloid assemblies, the assembly often go through structural transition from an intermediate state to the final stable

conformation through molecular re-arrangements.[12] Several previous studies have demonstrated the emergence of such intermediates. Anti-parallel β sheet is cited as the most common intermediate for Aβ folding process [13,14]. R.A. Gangani D. Silva, etl.al studied the IE-IR transition of a segment of prion protein PrP^{c}. PrP^{C} (109-122) Ac-MKHMAGAAAAGAVV-NH_2. **Figure 3-1** shows the alignment of Ala 117 before and after the assembly. The increase of ^{13}C signal from [1-^{13}C] A117 indicates over time, the alanines are increasingly aligned.[15] These studies excel at monitoring the transition between unassembled or disorganized structures to β-sheets. However, detailed structural elucidation of the intermediates remains to be developed.

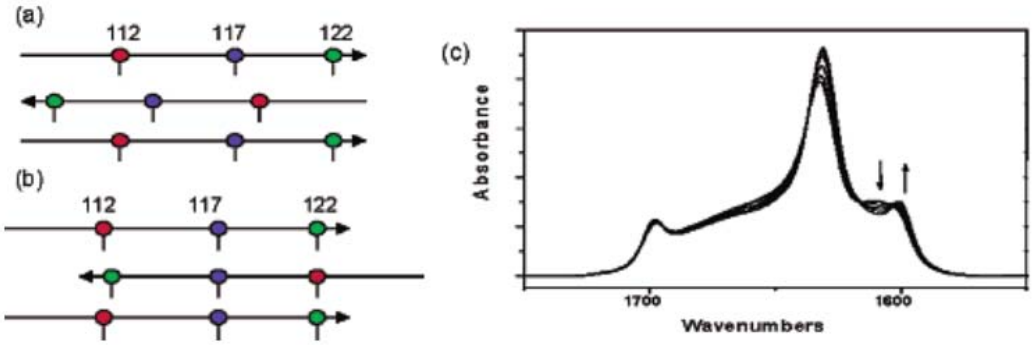

Figure 3-1. Strand alignment in the PrPc peptide. (**a**)The initial alignment of strands. (**b**)The strand alignment of mature peptides. (**c**) The change of IE-IR signal overtime

From previsou studies discussed in chapter 1, conformational change occurs frequently between the particle phase and amyloid phase. These two phases possess distinctive chemical enviroments: the internal enviroment of particle is highly desolvated and the peptides are concentrated, disorganized and under rapid exchange; the amyloid phase exposes the ends of all peptides to the solution and peptides are arrange in a paracrystallien way. As peptides are responsive to environment and environmental changes shifts conformaion distribution, a

peptide might change structure while transitioning from particle phase to amyloid phase (**Figure 3-2**).

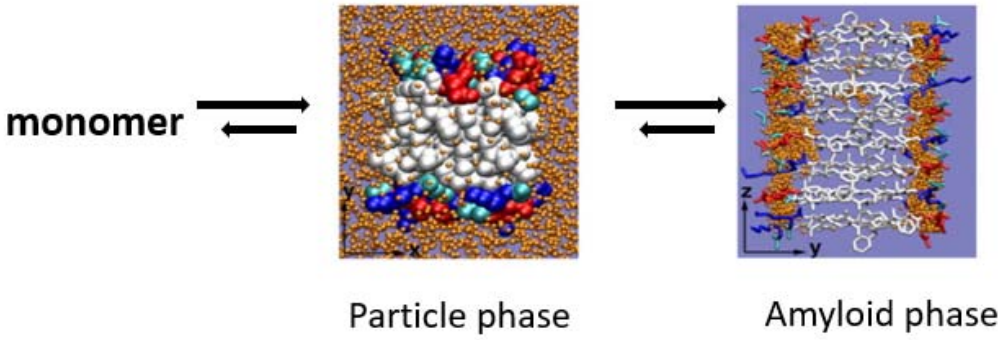

Figure 3-2. Peptides are exposed to different chemical environments when transitioning through particle phase to amyloid phase

To test this hypothesis, Aβ(16-22)E22Q is used where two physical forces dictating opposite strand orientations are incorporated to the same peptide. The electrostatic repulsion between lysine favors the anti-parallel β-sheet conformation, while the formation of inter-strand glutamine hydrogen bonding (Q track) favors the parallel strand orientation (**Figure 3-3**). In the particle phase, lysine-lysine repulsion is the strongest due to dehydrated environment and high peptide concentration. Such effect is significantly weakened at the amyloid phase as the electrostatic repulsion force is buffered by solvent. Such a shift of strength leads to a shift of energy landscape, which might dictate different structural formation.

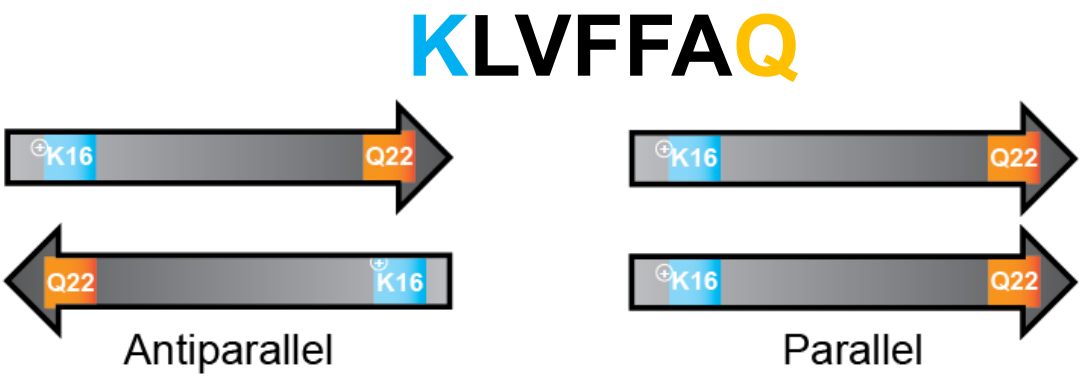

Figure 3-3. Physical forces dictating opposite strand orientation co-exist on Aβ (16-22) E22Q When lysine repulsion (light blue region) dominates the assembly, anti-parallel stand orientation is favored; when inter-strand glutamine hydrogen bonding (orange region) dominate the conformation, resulting in parallel β-sheet formation.

In this chapter, combining isotope edited-IR and solid-state NMR, I captured and characterized an intermediate of Ac-KLVFFAQ-NH_2, or Aβ (16-22)E22Q or simply E22Q, measured its life-time and mapped the process of its transition to the thermodynamic product. This result suggests an alternative self-assembly mechanism, illustrates the underlying physical factors influencing the structural transition during self-assembly and further demonstrates the dynamic nature of amyloid assemblies over time.

Methods

Peptide synthesis and purification: Peptides were synthesized using a Liberty CEM Microwave Automated Peptide Synthesizer (NC, USA) and a FMOC-Rink Amide MBHA Resin (AnaSpec, CA, USA). FMOC-Rink Amide MBHA Resin was swollen using dimethylformamide for 15 minutes. Microwave assisted FMOC deprotection was completed

using 20% piperdine in dimethylformamide at 45-55°C for 180 sec, followed by 3X dimethylformamide flushes. Each FMOC-amino acid coupling step was performed using 0.1M FMOC protected amino acid and activated with 0.1 M 2-(1H-Benzotriazole-1-yl)-1,1,3,3-tetramethyluronium hexafluorophosphate (HBTU), and 0.2 M N,N –Diisopropylethylamine (DIEA) in DMF. Coupling temperatures using microwave were maintained between 75-82°C for 300 sec, then rinsed with three aliquots of dimethylformamide. Phosphotyrosine and phosphoserine was double coupled with 6W power instead of 8W for other amino acids resulting in a final temperature for coupling of 75°C. Final acetylating of the N-terminus was achieved by addition 20% acetic anhydride in dimethylformamide. Resin was filtered and washed with dichloromethane and allowed to air dry. Peptides were cleaved from the resin using trifluoroacetic acid/thioanisole/1,2-ethanedithiol/anisole (90: 5 : 3 : 2, v/v/v/v) at room temperature for 3 hrs. The cleaved peptide-TFA solution was filtered, and precipitated by drop-wise addition to cold (-20°C) diethyl ether. Precipitated product was centrifuged at 3000 rpm for 10 min, and the pellet was further washed 3 times with cold diethyl ether. Dried peptide was dissolved in minimal volume of 40% acetonitrile/H_2O + 0.1% trifluoroacetic acid and purified by RP-HPLC using a C18-reverse phase column with an acetonitrile-water gradient. Molecular weight was confirmed by MALDI-TOF using a 2,5-dihydroxybenzoic acid matrix.

Transmission Electron Microscopy (TEM): A TEM copper grid with a 200 mesh carbon support (Electron Microscopy Sciences) was covered with 10 μL of a diluted peptide solution (0.05 mM to 0.1 mM) for 1 min before wicking the excess solution with filter paper. 10 μL of the staining solution, either (2% uranyl acetate, Sigma-Aldrich, or methylamine tungstate, Ted

Pella, Inc) was added and incubated for 2 min, excess solution was wicked away, and the grids were placed in desiccators to dry under vacuum overnight. Methylamine tungstate was used for early time point micrographs due to superior contrast of ribbons compared to uranyl acetate A Hitachi H-7500 transmission electron microscope was used to image the samples at 75 kV.

Circular Dichroism spectroscopy: Jasco-810 circular dichroism (CD) spectropolarimeter was used to record CD spectra in a 20 μL cell with a 0.1 mm path length at room temperature. The reported spectra represent the average of three scans between 260 nm to 190 nm with a stepsize of 0.2 nm and a speed of 100 nm/s. Ellipticity , θ, in mdeg was converted to Molar ellipticity [θ] with [θ] = θ/(10 x *c* x *l*), where *c* is the peptide concentration in moles/L and *l* is the path length in cm.

Attenuated Total Reflectance Fourier Transform Infrared (AT-FTIR): Aliquots (10μL) of peptide solution were dried as thin films on an Pike GaldiATR (Madison, WI, USA) ATR diamond crystal. FT-IR spectra were acquired using a Jasco FT-IR 4100 (Easton, MD, USA) at room temperature and averaging 500 to 800 scans with 2 cm^{-1} resolution, using either an MCT or TGS detector, 5 mm aperture and a scanning speed of 4mm/sec. Spectra were processed with zero-filling and a cosine apodization function. IE-IR spectra were normalized to the peak height of the ^{12}C band.

X-ray powder diffraction sample preparation: Mature fibrils were centrifuged at 16,100xg for 10 min and the pellet was frozen and lyophilized to yield a dry powder and used directly for

X-ray powder diffraction. The diffraction patterns were measured with Bruker APEX-II diffractometer with graphite monochromated Cu radiation K-alpha radiation, λ= 1.54184 Å, 40kV and 35 mA, with a 0.5 pinhole collimator and with exposure times of 300 s per frame. The sample was loaded into a 0.2 mm mylar capillary. The data integration software XRD2SCAN was used to convert the two dimensional data into a θ-2θ scan.

Seeded Assembly: 0.8 mM [1-^{13}C]F19 Aβ(16-22)E22Q monomers were dissolved in 20% acetonitrile/water with 0.1% TFA and bath sonicated for 10 min. 1% mature [1-^{13}C]F19 Aβ(16-22)E22Q fiber that had been confirmed as parallel by FT-IR were vortexed for 10 seconds to form seeds and added to the monomer solution.

Results

E22Q assembles through an anti-parallel to parallel β-sheet transition

Based on the structure-conformation relationship discussed in previous chapters, E22Q contains competing physical factors favoring opposite strand registry. To investigate which conformation would be the pre-dominant one at different stages of assembly, peptides were dissolved and assemble in 20% acetonitrile/water (20%MeCN/H_2O) with 0.1% trifluoroacetic acid (TFA) (v/v). The assembly process was monitored with Transmission Electron Microscopy (TEM) and Infrared Spectroscopy.

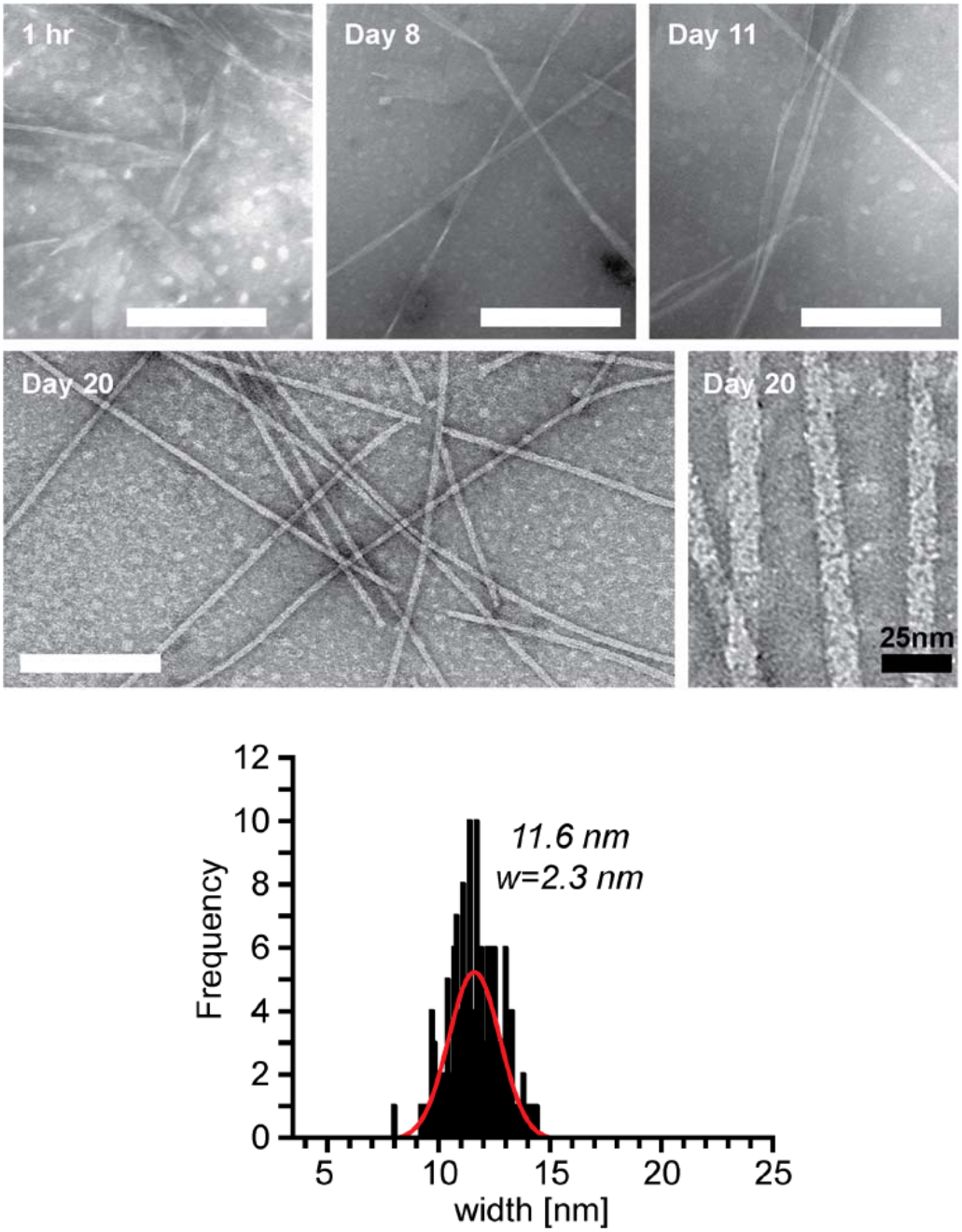

Figure 3-4. TEM of the morphological change of Ac-KLVFFAQ-NH_2. Upon dissolving, particles and twisted ribbons were observed. These ribbon kept elongating and becoming thinner over-time. After 20 days, peptide conformation shifted to fibers with 11.6±1.2nm (scale bar 200nm)

TEM result shows that upon dissolving of the peptides, particles and short twisted ribbons emerge (**Figure 3-4 A**). Overtime, these ribbons elongate and became thinner, meanwhile

straight, non-twisted fibers started to appear (**Figure 3-4 B**). Eventually, the whole system stabilized as homogenous, straight fibers (**Figure 3-4 C**) with diameter around 11nm (**Figure 3-4 D**).

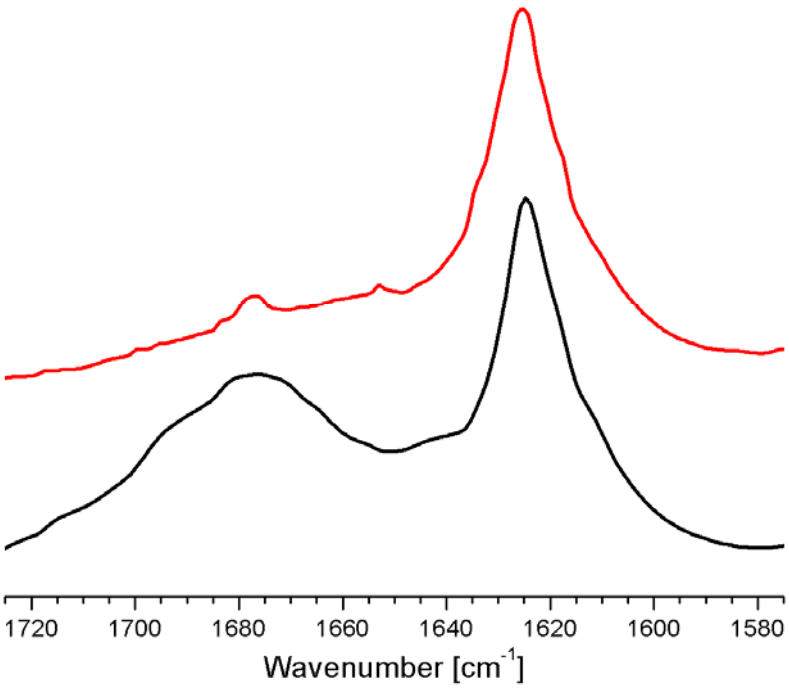

Figure 3-5. The FT-IR spectrum on the first (**Black**) and final day (**Red**)
They both exhibit a 1625cm^{-1} peak of β-sheet. On day 0, the broad peak around 1675 cm^{-1} comes from unassembled peptide, the weak peak at 1676 cm^{-1} suggested ordered glutamine side-chain or Q track.

FT-IR study proved that both the initial ribbon and end fiber state consist of β-sheet, consistent with amyloid formation (**Figure 3-5**). To better understand the structural details of these changes, isotope-edited IR experiment was conducted with ^{13}C=O enrichment on the central phenylalanine, forming [1-13C]F19 Aβ(16-22)E22Q, where ^{12}C/^{13}C coupling is strongest and the most diagnostic of β-strand orientation[5,7,16].

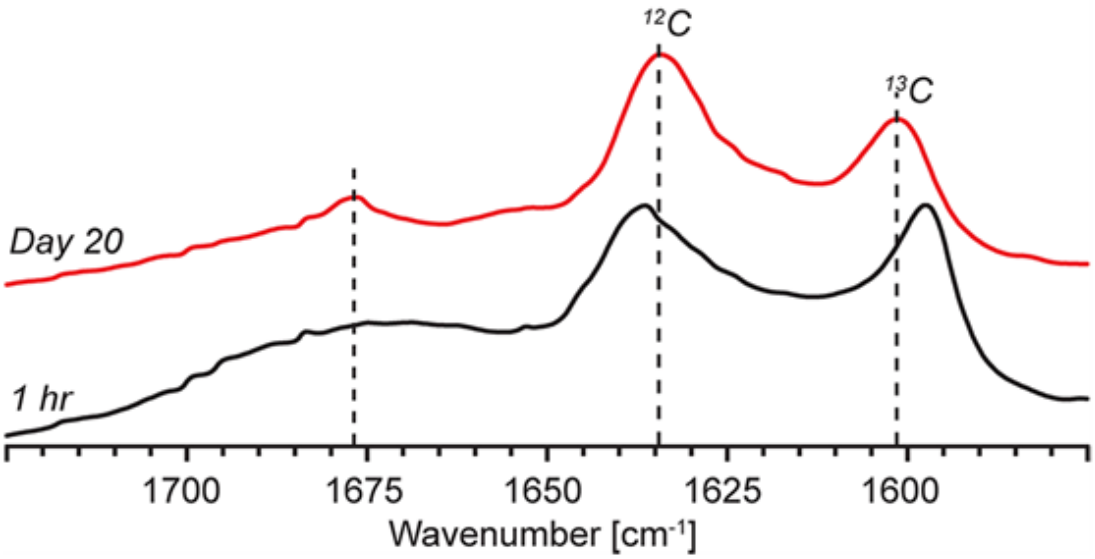

Figure 3-6. IE-IR spectrum of [1-^{13}C]F19 Aβ (16-22)E22Q at the beginning and end of assembly process.

Upon dissolving, the IE-IR (Black line) signal is consistent with anti-parallel out-of-register β-sheet with the ^{12}C-^{13}C splitting of 40cm^{-1} and ^{12}C/^{13}C peak ratio is less than 1. At the end of transition, the ^{12}C-^{13}C splitting has decreased to 33 cm^{-1} and the ^{12}C/^{13}C peak ratio is greater than 1.

IE-IR shows a band splitting of almost 40cm^{-1} and a ^{12}C/^{13}C peak ratio of ＜1 (**Figure 3-6, Black line**). This spectrum is consistent with what has been assigned to anti-parallel out-of-register β-sheet.[7] However, this conformation does not persist as at the end of the assembly where the conformation stabilized as non-twisted homogenous fibers, the ^{12}C peak is red-shifted while ^{13}C peak went through a blue shift. Meanwhile, the ^{12}C/^{13}C intensity has increased to 1.3 (**Figure 3-6, Red line**).

To confirm the structure of the fibers, circular dichroism (CD) and X-ray powder diffraction

(XRD) experiments were conducted. The 217 nm minimum of CD signal and the d-spacing reflections of 4.76 and 10.1 Å confirmed the cross-β structure of the fiber as the thermodynamic conformation. (**Figure 3-7**)

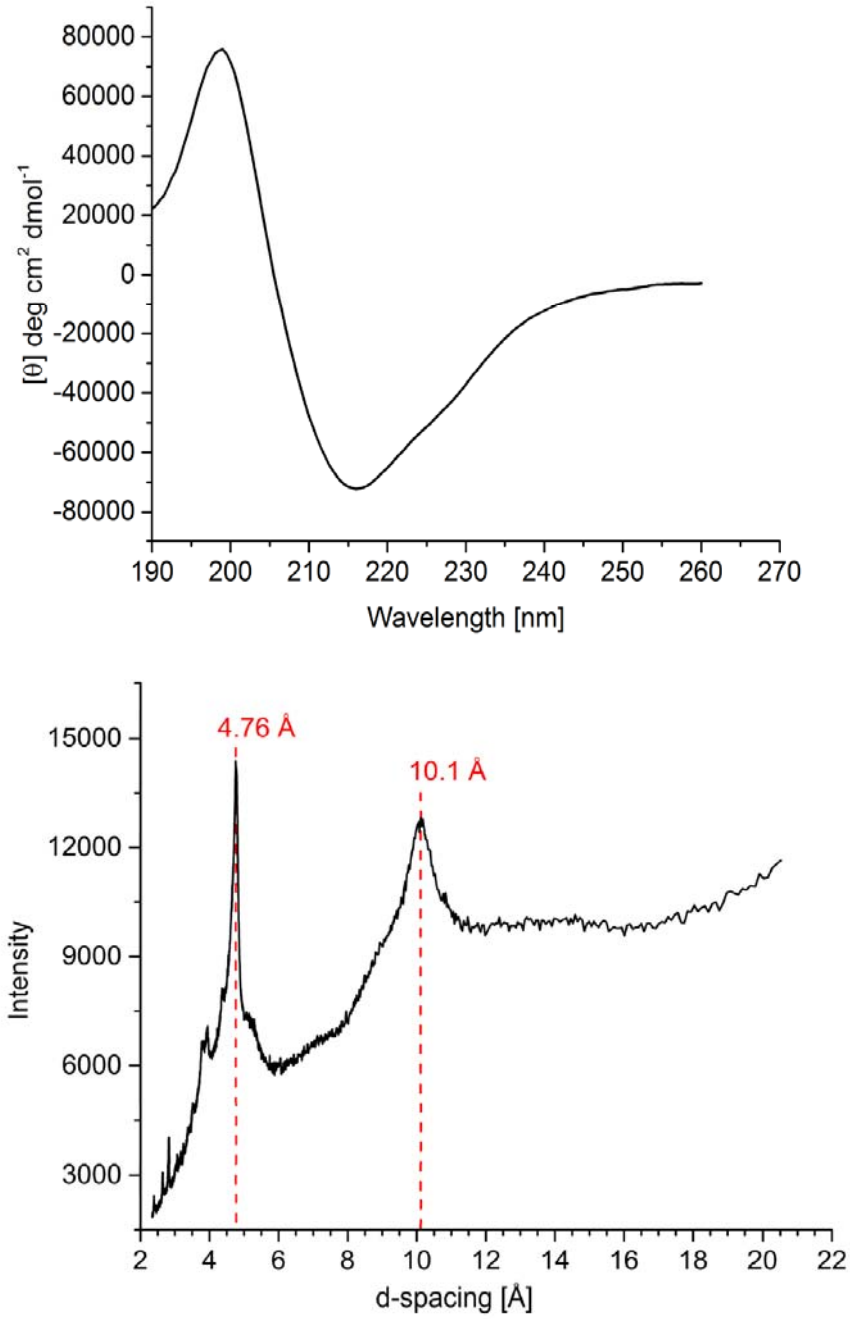

Figure 3-7. CD and XRD of [1-^{13}C]F19Aβ(16-22)E22Q fibers when conformation transition is complete. The CD (upper) data shows an ellipticity minimum at 217nm, consistent with a β-sheet conformation. XRD diffraction pattern (bottom) exhibit classical cross-βconformation with reflections at 4.76 Å representing hydrogen-bonding between peptide strands and 10.1 Å showing distance in between β-sheets.

The orientation and registery of the final orientation is determined through the rate of double-quantum coherence build-up through homonuclear dipolar coupling in ^{13}C DQF-DRAWS solid-state NMR experiment with [1-^{13}C] label on L17. Using the infinite array approximation (**Figure 3-8**) and including the effects of double quantum relaxation, T_2DQ=11.7ms (**Figure 3-9**). The buildup of [1-^{13}C]L17 intensity fits a parallel in-register strand arrangement Figure (**Figure 3-10**),

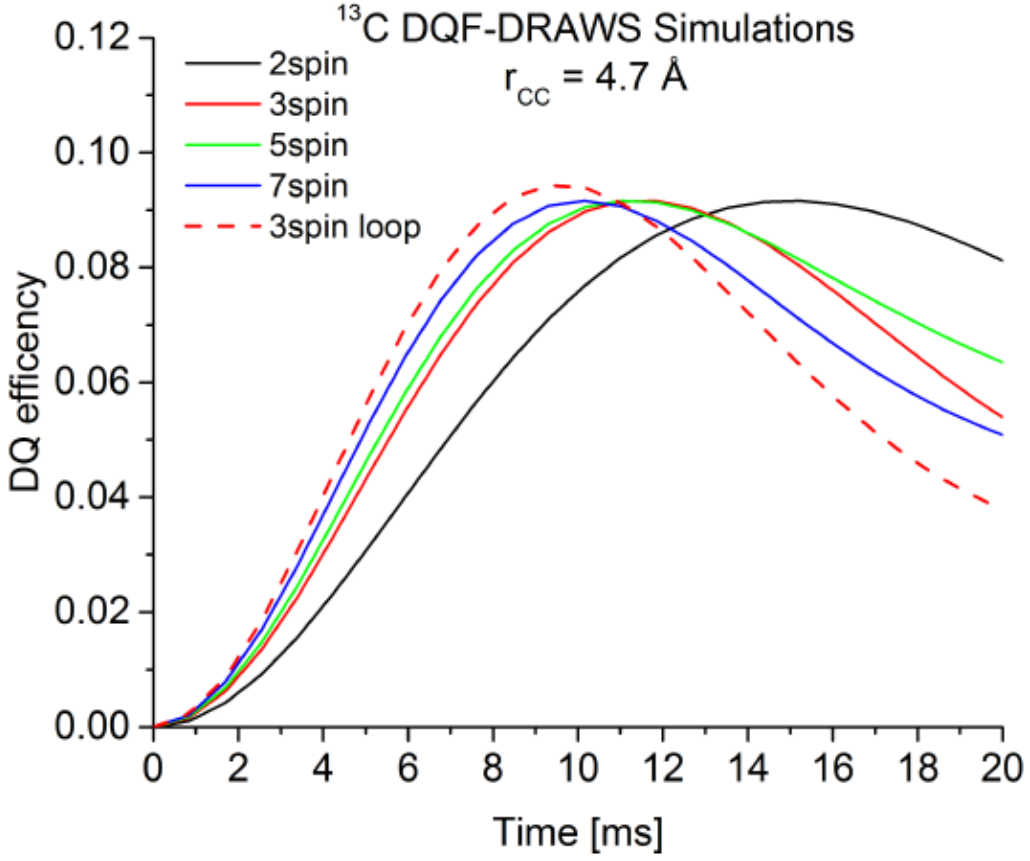

Figure 3-8. ^{13}C Double-Quantum Filtered DRAWS calculated build-up curves comparing linear arrays of ^{13}C spins to a 3-spin loop. The DQ build-up for the linear array of spins appears to be asymptotically approaching the 3-spin loop.

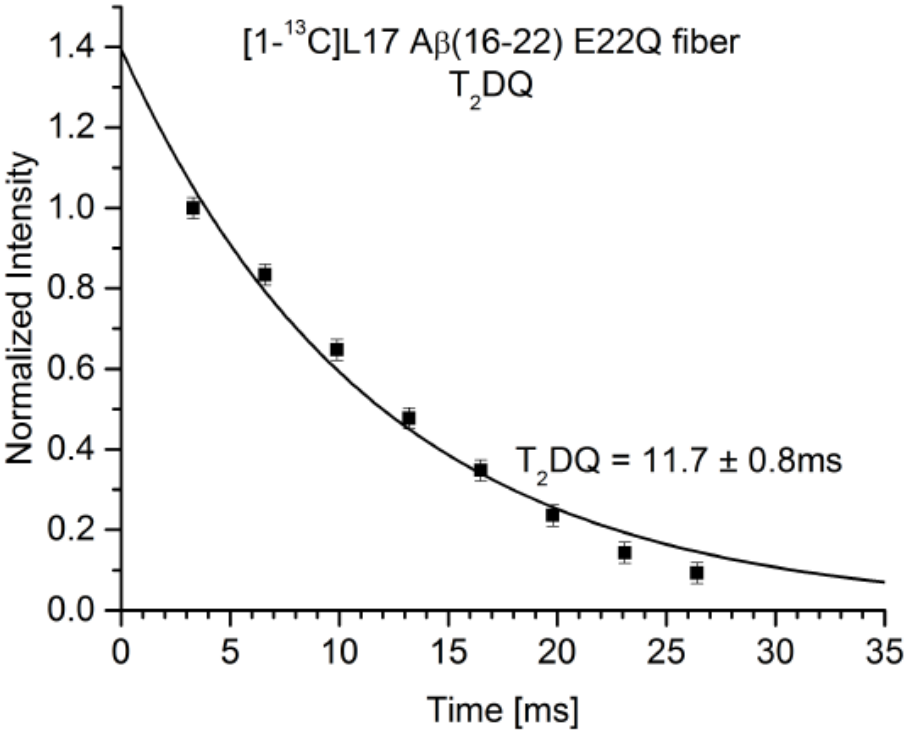

Figure 3-9. ^{13}C Double Quantum relaxation (T2DQ) of [1-^{13}C]L17 Aβ(16-22)E22Q. T_2DQ was measured by inserting a composite 180°pulse between DRAWS pulses.[17] Solid line is best fit of a monotonically decaying exponential to the experimental data points.

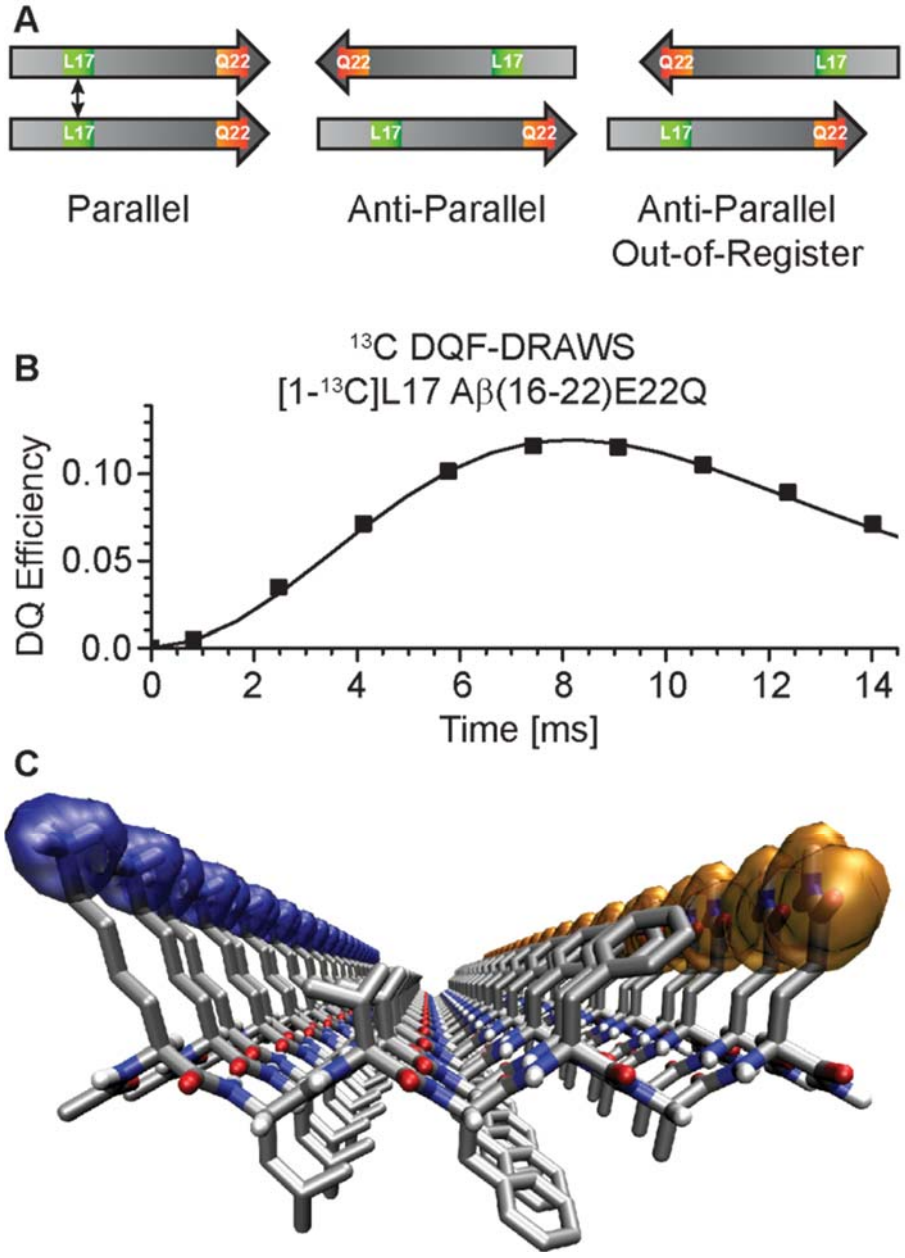

Figure 3-10. Determination of β-sheet conformation of [1-13C] L17 Aβ(16-22)E22Q fibers. (**A**)Cartoon showing the relative position of [1-13C] L17 (green) when peptide adopt various β-sheet conformations.
(**B**) Peak intensity (data points) for double-quantum buildup divided by total 13C signal intensity. The beset fit to DQ buildup is with a 4.7 Å 13C-13C distance.
(**C**) Peptide model built according to DRAWS data with parallel in-register β-sheet. Lysine and glutamine were colored blue and orange respectively.

Measuring the kinetics of conformational transition

Based on data collected during the transition process, a transition from anti-parallel out-of-register to parallel in-register β-sheet can be observed, especially through the ^{13}C peak position. To better understand the mechanism of such a transition, the kinetics of such transition can is measured by the ^{12}C-^{13}C peak splitting and $^{12}C/^{13}C$ peak ratio of the IE-IR spectrum of [1-^{13}C]F19 Aβ(16-22)E22Q over time (**Figure 3-12**).

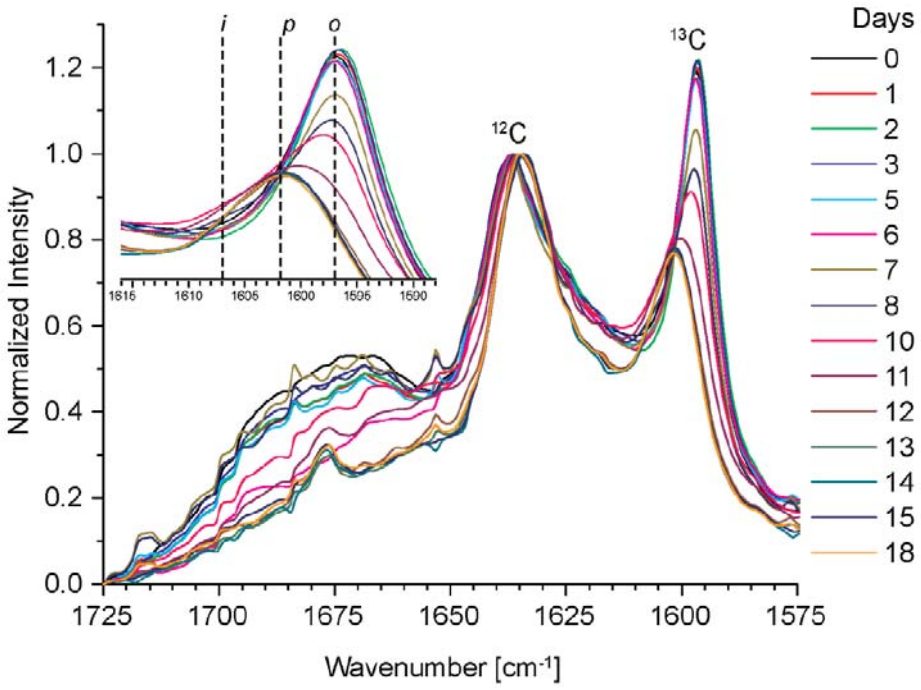

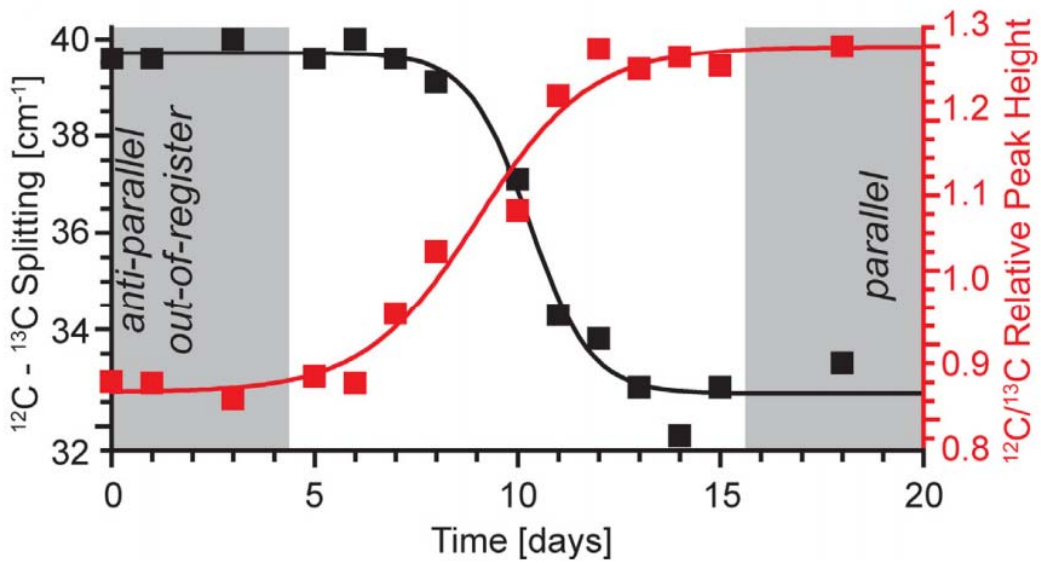

Figure 3-11. Time dependence of the assembly of 1mM [1-^{13}C]F19 Aβ(16-22)E22Q at acidic pH in 20% MeCN/H2O containing 0.1% TFA monitored by isotope-edited IR analysis with ^{12}C/^{13}C splitting (**black**) and relative peak height (**red**) for assemblies collected at multiples

It can be observed that the assembly started as anti-parallel out-of-register and maintained in that conformation for about five days. Later, the transition started and the sigmoidal line shape for both ^{12}C/^{13}C peak ratio and ^{12}C-^{13}C peak splitting indicated a self-catalytic process. In the first five days, no IR change can be observed as peptides initially assemble into anti-parallel out-of-register ribbons and that conformation persists for a while. Then later, in day 5, parallel β-sheet was formed and upon its formation, a self-catalytic process was initiated, therefore the whole system goes through a sigmoidal transition into parallel structure and stabilized into thermodynamically most stable structure.

Mapping conformational changes with IE-IR fitting

The IE-IR fitting established in the previous chapter enables us to understand the species distribution, which is one step further than simply measuring the splitting in last chapter. The IE-IR data taken for [1-^{13}C]F19 Aβ(16-22)E22Q was fitted into the basis sets using mathematica and the corresponding coefficients of different spectra are plotted against time.

From the data (**Figure 3-12**), we can see that upon dissolving, the solution contains predominantly twisted ribbons (blue line) and unassembled peptide (purple line). This state persisted for around seven days before the emergence of parallel species (green line).Along with the seeding experiment mentioned before, this graph further substantiates the statement that there is no parallel fiber during the first week of assembly and parallel nucleus appears within the middle. Upon the appearance of parallel fiber on day 7, a rapid and cooperative increase of the parallel species is observed till it reaches full completion. The increase of parallel species and the decrease of anti-parallel out-of-register peptide are clearly observed in panel B. Additionally, there is negligible amount of anti-parallel in-register during the process. This is in drastic contrast from the salt sample and mono-methylated sample in later studies. [18]The development of IR fitting basis sets enables us to monitor population changes of a polymorph system over time therefore can be further applied to investigating various internal (sequence, concentration, side chain) and external (salt, pH, dielectric and agitation, etc.) factors' influence on a self-transitioning amyloid system.

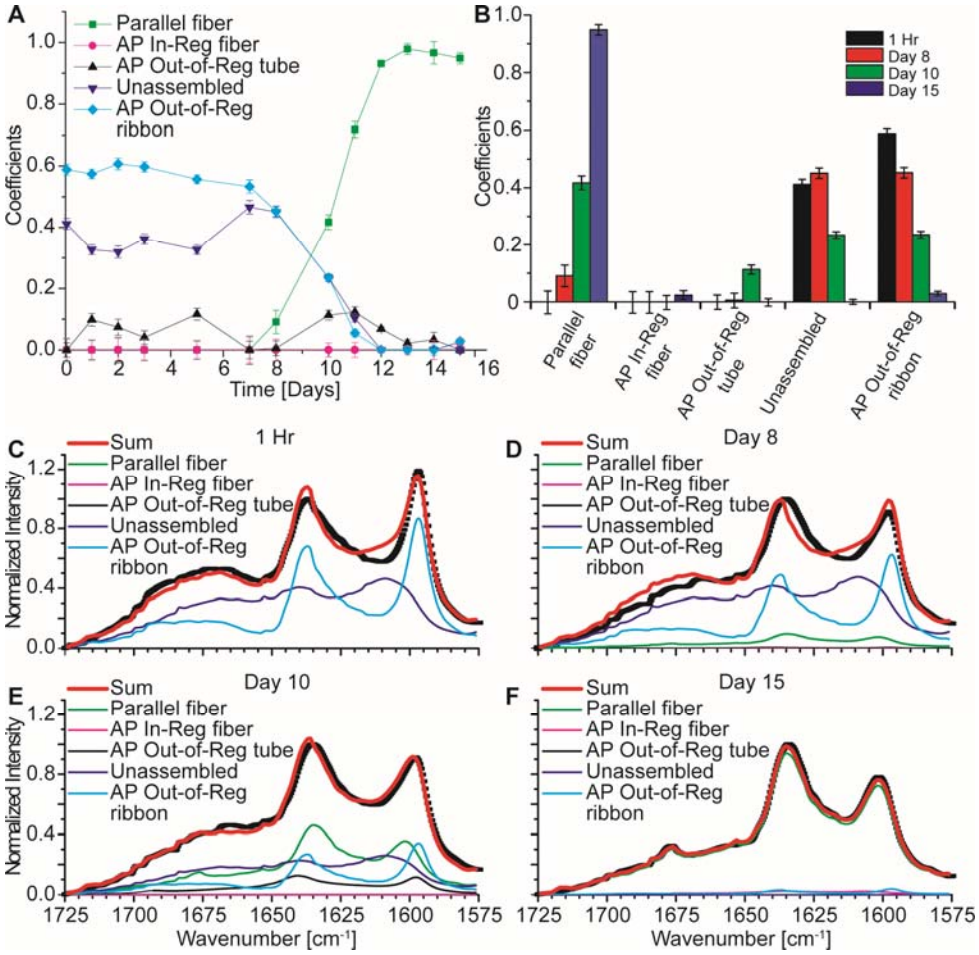

Figure 3-12. Fitting of the IE-IR spectrum of [1-^{13}C]F19 Aβ(16-22)E22Q over time.
(**A**) The change of various populations overtime.
(**B**) The trend of various population change for various conformations.
(**C-F**) Best fits (red line) to individual IE-IR specta of [1-^{13}C]F19 Aβ(16-22)E22Q (black squares) at different time. Spectra of the basis set are scaled according to their coefficient and coloured as in panel A.

Glutamine side chain is the determining factor of the structural transition

Based on the results, the electrostatic repulsion and inter-strand hydrogen dominates different stages of the assembly process. In the nucleation phase, due to the high concentration of peptides, lysine-lysine repulsion is the dominating force, driving an anti-parallel strand orientation. During elongation, the aqueous environment around the elongating ends attenuates

the repulsing forces, allowing the Q-Q hydrogen bonding to dominate the assembly and leads to a parallel sheet formation.

To test the hypothesis that Q-Q interaction is the crucial factor for formation of parallel-β sheet, we methylated the two hydrogen on glutamine side chain and observe the peptide's behavior. Results show that interruption of hydrogen bond formation by methylation prevents the structural transition.

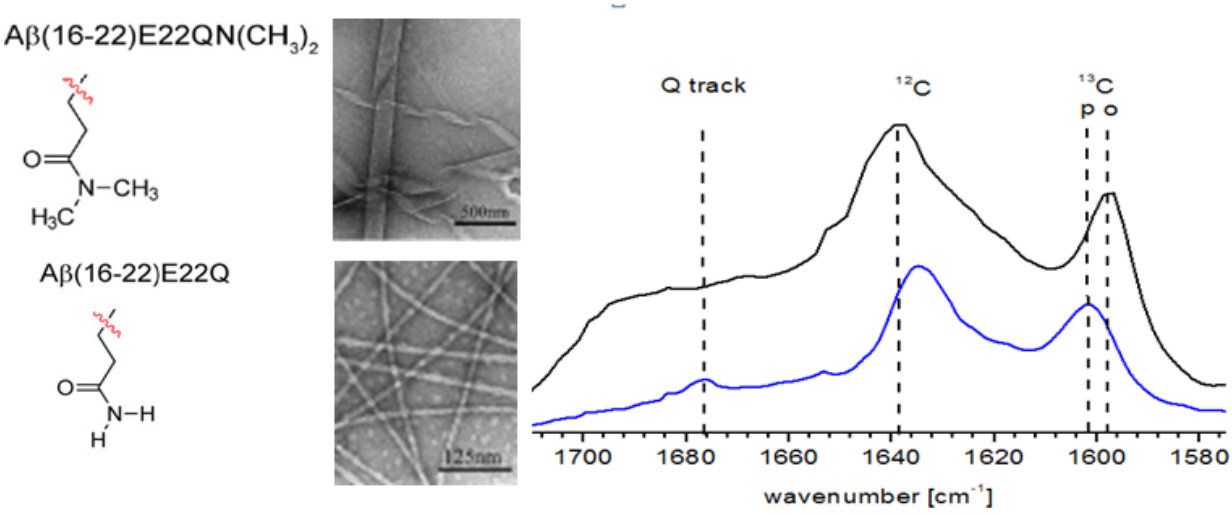

Figure 3-13. Impact of methylation the glutamine side chain on Aβ (16-22)E22Q. TEM shows the conformation of different side-chain modifications (**left**). IE-IR of stabilized E22Q (Blue) vs di-methylated E22Q (Black) (**right**).

As indicated in **figure 3-13**. Aβ(16-22)E22Q assembles into parallel non-twisted fibers with ^{13}C peak at 1062cm^{-1} and Q band at ~1677 cm^{-1}. The di-methylated Aβ(16-22)E22QN$(CH_3)_2$ mutant remains in anti-parallel out-of-register state without transitioning, as indicated in the broad splitting of IE-IR spectrum and the ~40cm^{-1}and a weak band at ~1695 cm^{-1}.[7]

This experiment proves the formation of parallel β-sheet is dictated by the Q track formed

through inter-strand hydrogen bonding between neighboring glutamines, without which no transition can be observed as only anti-parallel out-of-register strand orientation is only observed with the methylated mutant. Additionally, the typical d spacing of 10.1Å obtained through X-ray crystallography proves the formation of Q track is within one layer of β-sheet instead of between sheets. Because inter-sheet hydrogen bonding would decrease the distance between β-sheet and decrease the sheet-stacking(lamination) distance by 2Å as is seen in polyglutamine peptides[19].

The impact of pathway barrier adjustment on amyloid conformational transition

With IE-IR fitting, the transition kinetics can be mapped and a more detailed conformational distribution analysis can be conducted, especially for the mono-methylated glutamine sample. Mono-methylation of glutamine attenuates the Q track hydrogen bonds. The resulting congener samples a wider range of intermediates, and transitions more than 10 times slower than regular E22Q. The result is shown in **Figure 3-14**. After IR fitting, the slightly more hydrophobic N terminus congener shows less unassembled peptide upon dissolution of the monomers. Additionally, species such as anti-parallel in-register (colored in pink) is higher than E22Q. The emergence of parallel fiber is earlier despite the longer transition time. This indicates a different and more complex pathway of transitioning for mono-methylated E22Q mutant. Additionally, the TEM of 3 weeks' sample shows more bundled morphologies, suggesting alternative ways of fiber association. This could serve as the reason for different transition kinetics. Despite the

difference in the middle, at long times, fits of the IR spectra show virtually exclusive parallel β-strand orientation with the same smooth, straight fibers dominating the electron micrographs (**Figure 3-14 C and G**).

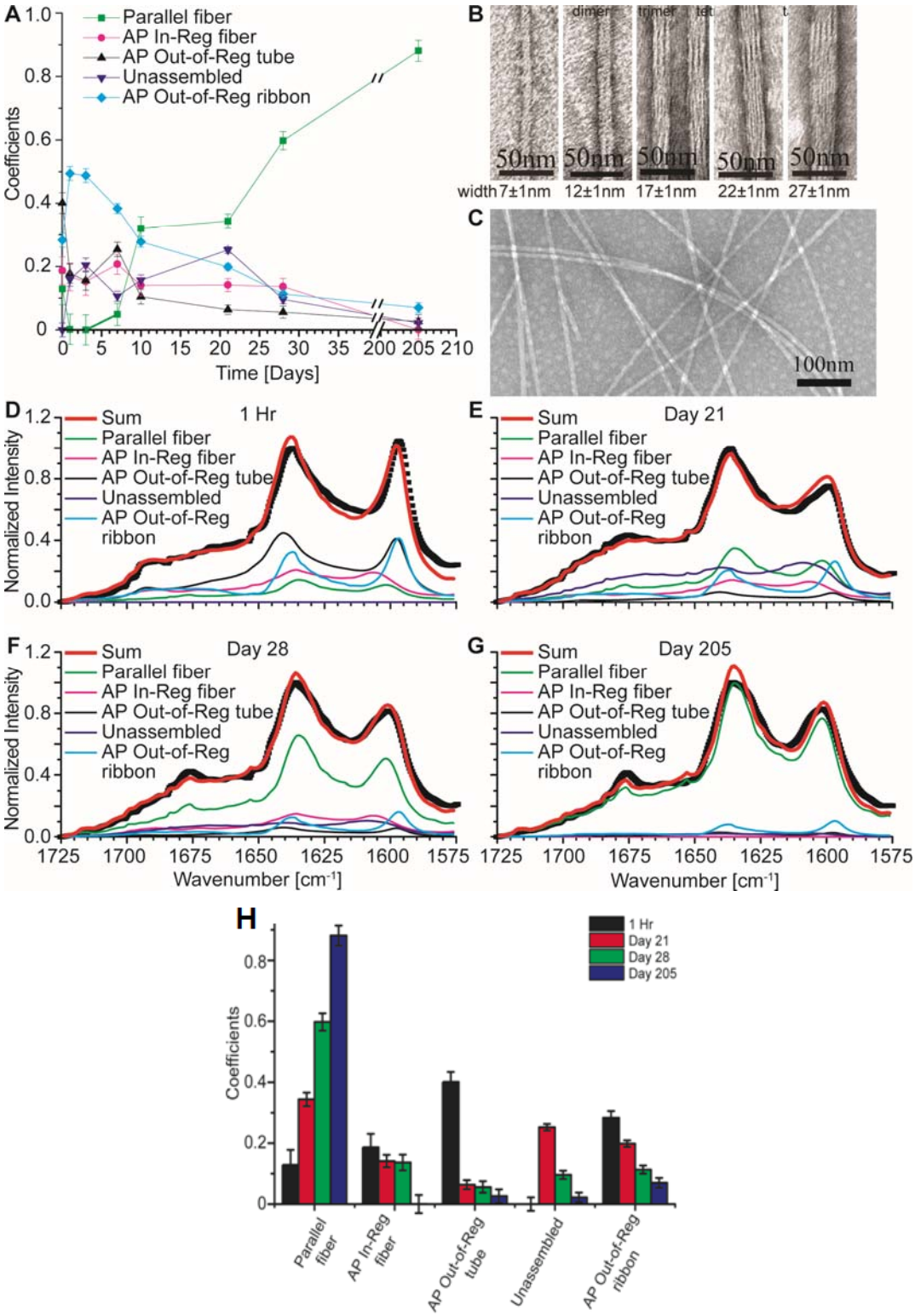

Figure 3-14. IR fitting of mono-methylated E22Q over time.

(**A**) Compared to E22Q, the congener has higher ratio of anti-parallel intermediates and takes longer to transition.

(**B**) Negatively stained TEM of 21 day is heterogeneously bundled.

(**C**) On day 205, straight smooth fibers are the dominant morphology observed.

(**D-G**) IE-IR fitting of different time points.

(**H**) The trend of various population change for various conformations.

Seeding experiment supports the lack of parallel nuclei at the beginning of assembly

To better support the argument of a self-catalytic process, 1% parallel seeds were added at the beginning of the assembly. IE-IR and TEM are taken to monitor the transition of the assembly. From **figure 3-15**, the 0hr IE-IR represents anti-parallel out-of-register, which means the peptides still form the kinetic intermediate first. Additionally, it also proves that 1% parallel fiber's signal is too weak and therefore negligible in the IE-IR spectrum. However, unlike pure sample where there was a five day waiting time, the transition from anti-parallel to parallel happens immediately for the seeded sample and the whole process is completed in 8 hours.

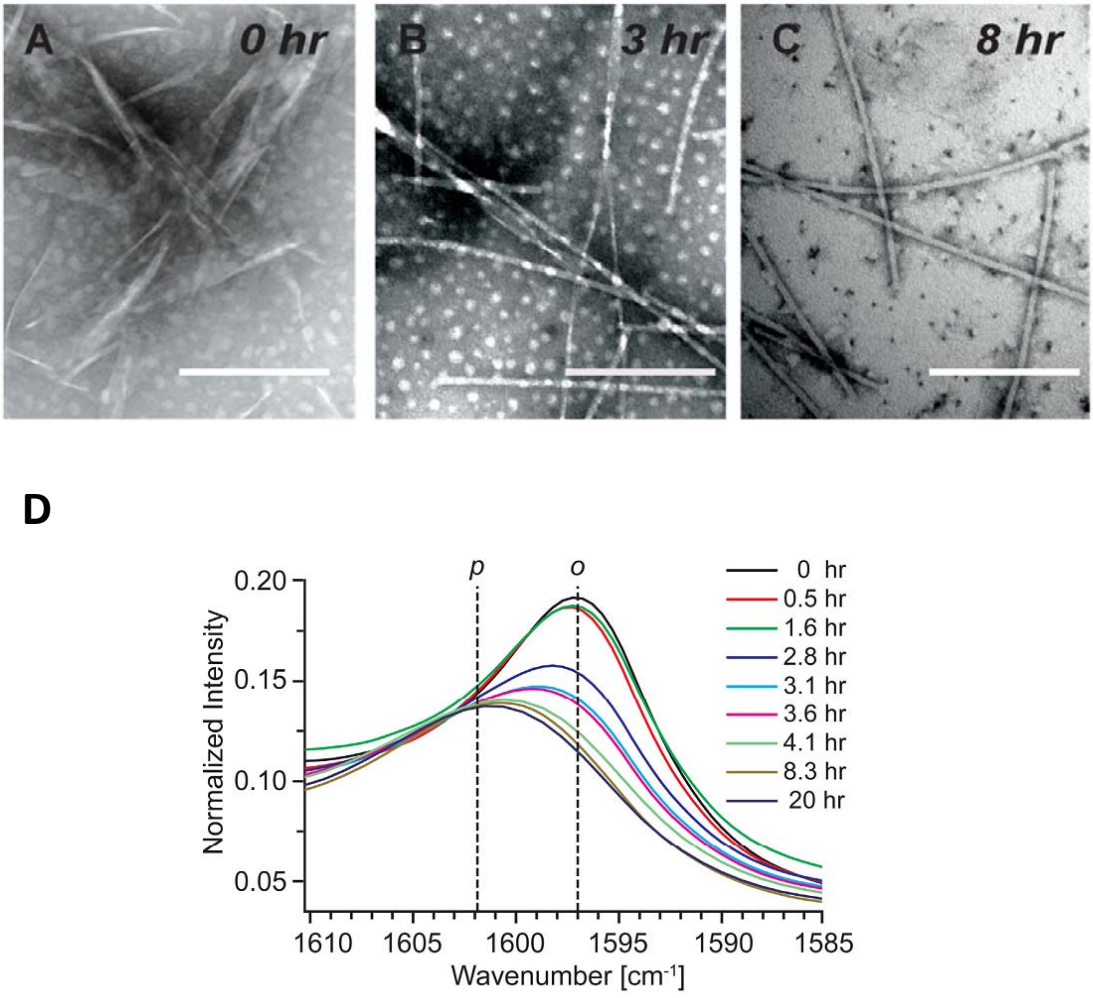

Figure 3-15. Conformational change of [1-^{13}C]F19 Aβ(16-22)E22Q seeded by 1% parallel fiber as seeds.

At 0 hr, the assembly still maintains an anti-parallel out-of-register conformation as shown by the ribbon on (**A**)TEM and the peak position on IE-IR. The transition is much faster as in (**B**) 3hr fibers can be observed and ^{13}C peak has dramatically shifted; in (**C**) 8hr, only homogenous non-twisted fibers can be seen and the ^{13}C peak is at parallel position. (**D**) FT-IR spectra of ^{13}C amide I band of 0.8mM [1-^{13}C]F19 Aβ(16-22)E22Q seeded with mature [1-^{13}C]F19Aβ(16-22)E22Q. ^{13}C band positions for anti-parallel out-of-register (o) and parallel assemblies (p) are indicated with dashed lines.

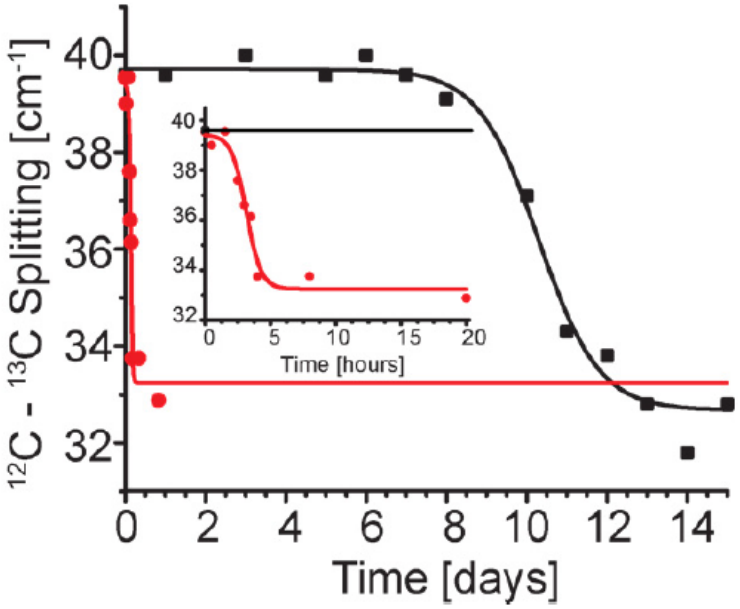

Figure 3-16. Comparison of transition kinetics of seeded vs unseeded Aβ (16-22) E22Q

As can be observed from **Figure 3-16**, the presence of parallel fiber would immediately trigger the transition process and the process would complete in about 8 hours. This result further confirmed parallel β-sheet as the thermodynamic product. Additionally, this result further proves the absence of parallel fibers in the first five days of the assembly, and that the parallel β-sheet only emerges in the middle of the assembly process.

Parallel nuclei is likely to emerge from mutation

After the establishment of parallel emerging only in the middle of the assembly, the next question is on the origin of parallel nuclei. Did they emerge at the surface of the elongating intermediate or the end of the intermediate? The former process utilizes the surface of the anti-parallel amyloid as a nucleation cite for the new structures to emerge; the latter is a result of

"mismatch" during elongation where the Q of incoming monomer first contacts the Q on template, driving the rest of the peptide to a parallel strand alignment.

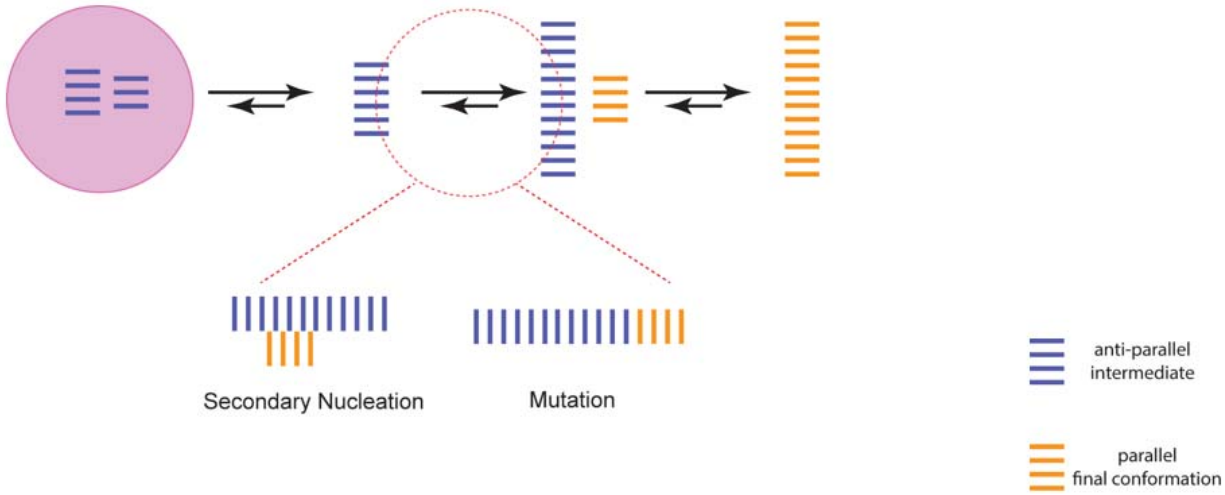

Figure 3-17. Potential mechanism for parallel nuclei formation.

To differentiate between these forces, shear force was applied to the solution. A magnetic stirrer was stirring at 250 rounds per minute. Under the mutation model, stirring will segment the pre-formed anti-parallel amyloids, generating more ends for a higher rate of mutation; yet the secondary nucleation model depends on the surface area, which won't be increased by stirring. Therefore, an increase of mutation rate indicates the assembly is likely to result from mutation.

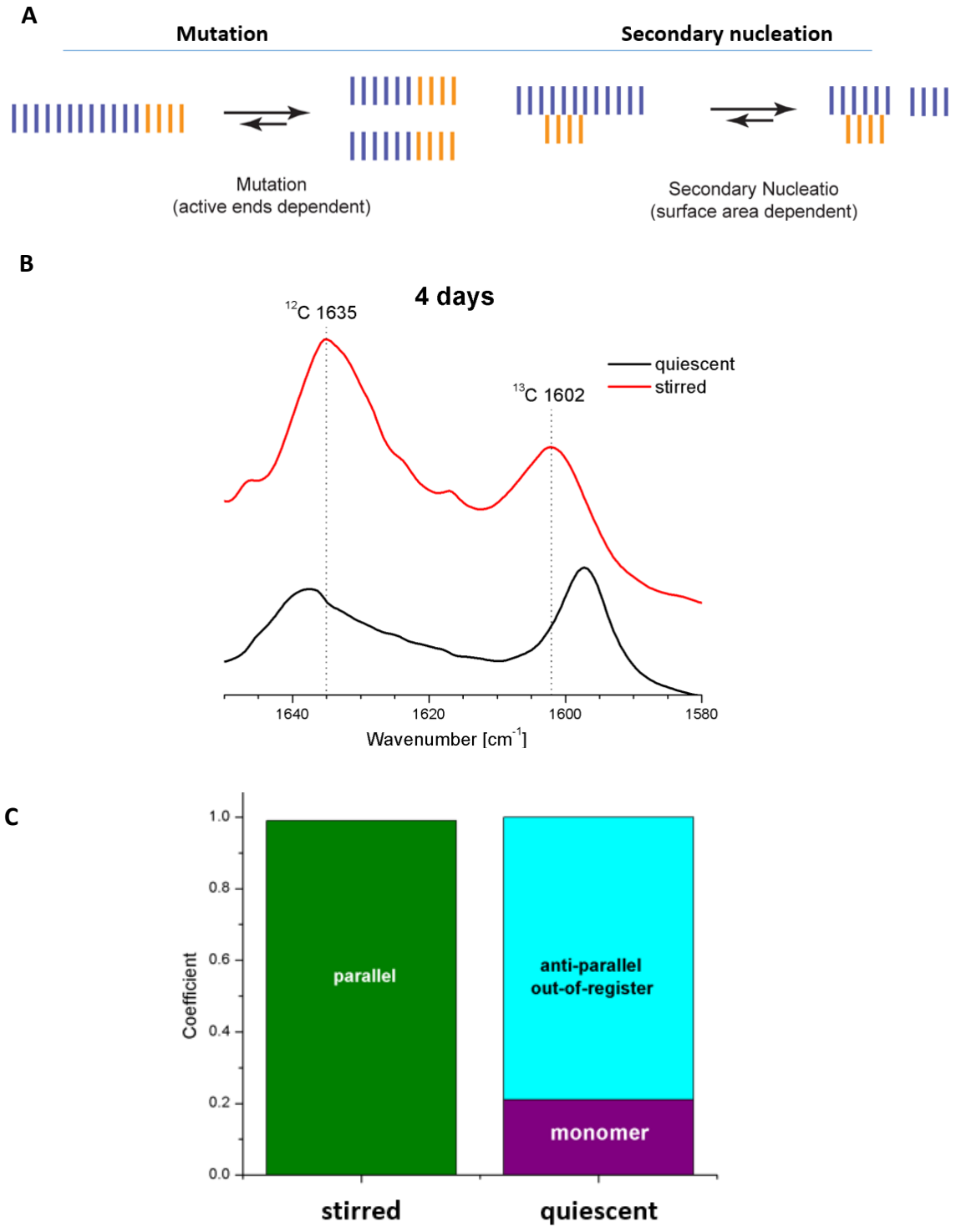

Figure 3-18. Stirring experiment supports mutation mechanism. (**A**)The impact of active ends and surface area under stirring (**B**) The IE-IR spectra of stirred (red) and quiescent (black) sample on day 4.(**C**) IE-IR fitting result of the day 4 IE-IR spectra of stirred and quiescent sample.

Conclusion

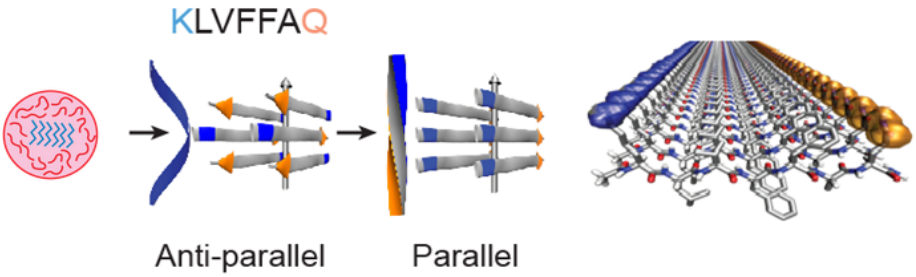

Figure 3-19. The assembly process of Aβ(16-22)E22Q

In this chapter, the assembly process of the nucleating core of Aβ Dutch mutant Aβ (16-22) E22Q is mapped out experimentally. As in **Figure 3-19**, once dissolved, peptide collapses into particles due to hydrophobic side chains of the peptide. Within the particle, paracrystalline amyloid structures start to form and anti-parallel nucleus are formed as kinetic product. In this phase, lysine-lysine repulsion is the dominating force due to the high concentration of peptides within the particle and the hydrophobic environment within the particle. After elongation, peptide ends a more exposed to the aqueous environment that could buffer the electrostatic repulsion between lysines. Meanwhile, the upcoming peptide that attaches to the end of amyloid could form a "mismatch" of parallel strand orientation that is stabilized by inter-strand glutamine hydrogen bonding, which is a stronger force than the repulsive tendency introduced by lysines. Such a thermodynamically more stable parallel structure starts to accumulate into a critical concentration, and then goes through a self-propagating process by seeding and eventually assimilate peptide monomer and dominate the whole assembly.

Our study demonstrated that the nucleating core of amyloid Dutch mutant Aβ(16-22)E22Q can be established as a system to study the competing tensions of thermodynamic and kinetic control of the amyloid assembly process. The whole sequence Aβ and other amyloidogenic proteins would have a more dynamic and diverse assembly pathways, especially in a more complex fluid environment[20] of cells.

As one of the dominating factor for the kinetic transition of Aβ(16-22)E22Q, glutamine increases the propensity for the formation of parallel strands and generates a more diverse and dynamic amyloid network. This might explain the mechanism for the high toxicity[21] and earlier onset[22] of Alzheimer's patients carrying the Dutch mutant.

Reference

(1) Liang, Y.; Guo, P.; Pingali, S. V.; Pabit, S.; Thiyagarajan, P.; Berland, K. M.; Lynn, D. G. Light harvesting antenna on an amyloid scaffold. *Chem Commun (Camb)* **2008**, 6522-6524.

(2) Kumar, S.; Walter, J. Phosphorylation of amyloid beta (A beta) peptides - A trigger for formation of toxic aggregates in Alzheimer's disease. *Aging-Us* **2011**, *3*, 803-812.

(3) Childers, W. S.; Anthony, N. R.; Mehta, A. K.; Berland, K. M.; Lynn, D. G. Phase networks of cross-beta peptide assemblies. *Langmuir* **2012**, *28*, 6386-6395.

(4) Hernandez-Guzman, J.; Sun, L.; Mehta, A. K.; Dong, J.; Lynn, D. G.; Warncke, K.

Copper(II)-bis-histidine coordination structure in a fibrillar amyloid beta-peptide fragment and model complexes revealed by electron spin echo envelope modulation spectroscopy. *Chembiochem* **2013**, *14*, 1762-1771.

(5) Liang, Y.; Pingali, S. V.; Jogalekar, A. S.; Snyder, J. P.; Thiyagarajan, P.; Lynn, D. G. Cross-strand pairing and amyloid assembly. *Biochemistry* **2008**, *47*, 10018-10026.

(6) Liu, P.; Ni, R.; Mehta, A. K.; Childers, W. S.; Lakdawala, A.; Pingali, S. V.; Thiyagarajan, P.; Lynn, D. G. Nucleobase-directed amyloid nanotube assembly. *J Am Chem Soc* **2008**, *130*, 16867-16869.

(7) Mehta, A. K.; Lu, K.; Childers, W. S.; Liang, Y.; Dublin, S. N.; Dong, J.; Snyder, J. P.; Pingali, S. V.; Thiyagarajan, P.; Lynn, D. G. Facial symmetry in protein self-assembly. *J Am Chem Soc* **2008**, *130*, 9829-9835.

(8) Bertolani, A.; Pirrie, L.; Stefan, L.; Houbenov, N.; Haataja, J. S.; Catalano, L.; Terraneo, G.; Giancane, G.; Valli, L.; Milani, R.; Ikkala, O.; Resnati, G.; Metrangolo, P. Supramolecular amplification of amyloid self-assembly by iodination. *Nat Commun* **2015**, *6*, 7574.

(9) Jucker, M.; Walker, L. C. Self-propagation of pathogenic protein aggregates in neurodegenerative diseases. *Nature* **2013**, *501*, 45-51.

(10) Westermark, G. T.; Westermark, P. Prion-like aggregates: infectious agents in human disease. *Trends Mol Med* **2010**, *16*, 501-507.

(11) Eichner, T.; Radford, S. E. A diversity of assembly mechanisms of a generic amyloid fold. *Mol Cell* **2011**, *43*, 8-18.

(12) Chen, S. W.; Drakulic, S.; Deas, E.; Ouberai, M.; Aprile, F. A.; Rivas, G.; Abramov,

A. Y.; Valpuesta, J. M.; Dobson, C. M.; Cremades, N. Structural characterization of toxic oligomers that are kinetically trapped during alpha-synuclein fibril formation. *Protein Sci* **2015**, *24*, 136-136.

(13) Necula, M.; Kayed, R.; Milton, S.; Glabe, C. G. Small molecule inhibitors of aggregation indicate that amyloid beta oligomerization and fibrillization pathways are independent and distinct. *J Biol Chem* **2007**, *282*, 10311-10324.

(14) Cerf, E.; Sarroukh, R.; Tamamizu-Kato, S.; Breydo, L.; Derclaye, S.; Dufrene, Y. F.; Narayanaswami, V.; Goormaghtigh, E.; Ruysschaert, J. M.; Raussens, V. Antiparallel beta-sheet: a signature structure of the oligomeric amyloid beta-peptide. *Biochem J* **2009**, *421*, 415-423.

(15) Silva, R. A.; Barber-Armstrong, W.; Decatur, S. M. The organization and assembly of a beta-sheet formed by a prion peptide in solution: an isotope-edited FTIR study. *J Am Chem Soc* **2003**, *125*, 13674-13675.

(16) Welch, W. R.; Keiderling, T. A.; Kubelka, J. Structural analyses of experimental 13C edited amide I' IR and VCD for peptide beta-sheet aggregates and fibrils using DFT-based spectral simulations. *J Phys Chem B* **2013**, *117*, 10359-10369.

(17) Gregory, D. M.; Benzinger, T. L.; Burkoth, T. S.; Miller-Auer, H.; Lynn, D. G.; Meredith, S. C.; Botto, R. E. Dipolar recoupling NMR of biomolecular self-assemblies: determining inter- and intrastrand distances in fibrilized Alzheimer's beta-amyloid peptide. *Solid State Nucl Magn Reson* **1998**, *13*, 149-166.

(18) Smith, J. E.; Liang, C.; Tseng, M.; Li, N.; Li, S.; Mowles, A. K.; Mehta, A. K.; Lynn, D. G. Defining the Dynamic Conformational Networks of Cross- Peptide Assembly. *Isr J Chem* **2015**, *55*, 763-769.

(19) Sikorski, P.; Atkins, E. New model for crystalline polyglutamine assemblies and their connection with amyloid fibrils. *Biomacromolecules* **2005**, *6*, 425-432.

(20) Fuller, G. G.; Vermant, J. Complex fluid-fluid interfaces: rheology and structure. *Annu Rev Chem Biomol Eng* **2012**, *3*, 519-543.

(21) Wang, Z.; Natte, R.; Berliner, J. A.; van Duinen, S. G.; Vinters, H. V. Toxicity of Dutch (E22Q) and Flemish (A21G) mutant amyloid beta proteins to human cerebral microvessel and aortic smooth muscle cells. *Stroke* **2000**, *31*, 534-538.

(22) Davis, J.; Xu, F.; Deane, R.; Romanov, G.; Previti, M. L.; Zeigler, K.; Zlokovic, B. V.; Van Nostrand, W. E. Early-onset and robust cerebral microvascular accumulation of amyloid beta-protein in transgenic mice expressing low levels of a vasculotropic Dutch/Iowa mutant form of amyloid beta-protein precursor. *J Biol Chem* **2004**, *279*, 20296-20306.

Chapter 4. Ionic effect on the conformational transition of amyloid

Introduction

In previous chapters, using the nucleating core of Aβ Dutch mutant, Ac-KLVFFAQ-NH_2 or E22Q, we mapped out its structural transition from anti-parallel within the particle to parallel in the elongation phase, highlighting the intermediate state emerged due to the microenvironment in particle phase. In dry particle phase, high peptide concentration prevents parallel peptide orientation, giving rise to anti-parallel nuclei. After elongating into solution phase, the solvent shields the electrostatic repulsion of lysine and Q-Q hydrogen bonding favors the parallel strand orientation. Ions have been known to regulate amyloid self-assembly by altering the dielectric constant or direct shielding of charges on peptide. Here, we demonstrate the first example of fully quantified transitioning amyloid system both in terms of kinetics and conformation distribution. Our study shows that salts impacts the process differently by state: in the particle phase, salt increases the degree of assembly but do not alter the conformation; in the elongation phase, salt speeds up the emergence of parallel nuclei and introduces heterogeneity.

The self-assembly process for peptides and proteins to self-assemble into cross-β structures have been intensely studied since the discovery that insoluble protein fibrils are implicated in the molecular etiology of many human diseases. Peptides derived from the nucleating core of Aβ sequence associated with Alzheimer's disease assemble into robust nano-artitectures, including fibers, ribbons and nanotubes with different strand orientation and registration.[1]

From monomer to supramolecular structure, peptides go through phase transitions of oligomerization, nucleation and propagation into paracrystalline assemblies. The process is complex, with both kinetic and thermodynamic factors contributing to the final structure over time. Environmental effects are infinite, with changes in pH, mechanical stress, ionic strength, solvent, and temperature contributing significantly to observed changes in protein folding and amyloid assembly pathways.[2] Of these, ionic strength, or the presence of salts, is extensively characterized.

Ion effects are specific and ubiquitous in chemical and biological systems and have demonstrated significant influences in amyloid self-assembly[3].Salt has been known to interact with Aβ peptide's self-assembly and alter assembly mechanisms, [4,5]accelerate assembly[6], the gelation process[7] and their conformation transitions. [8] So far, salts' impact is categorized into the following mechanisms:

1. Lower dielectric constant

Coulomb's law dictates the electric force is dictated by the distance of two charges and their distance.

$$r = \frac{k \times Q1 \times Q2}{d^2}$$

Where Q1 and Q2 represent the charge and d indicates the distance. Coulomb's constant k is dependent on the medium. In air, its value is 9.0×10^9 N • m^2 / C^2.

The dielectric constant is used to measure the resistance of solvent to Coulombic interaction between two charges. Water has high dielectric constant as it decreases charge interaction. Its relative dielectric constant against vacuum is around 80. Solvents with high dielectric constant become less permeable to charge interaction. The presence of salt limits water's distribution, therefore decreasing water's dielectric constant and limiting its disturbance of charge interaction in solution between ions. Inorganic solvents are also known to lower the dielectric constant. The dielectric constant for acetonitrile is around 37.5.

2. Hofmeister series

The Hofmeister series is used to measure the effects of ions on protein solubility and stability. It was first introduced as a ranking of the capacity of different ions to precipitate egg white proteins. Those that increase solubility and decrease stability are called chaotropes; others are named kosmotropes. Its mechanism is speculated to alter protein-water interaction through ion hydration, recent studies also proposed the mechanism is direct ion-macromolecule interaction.[9,10]

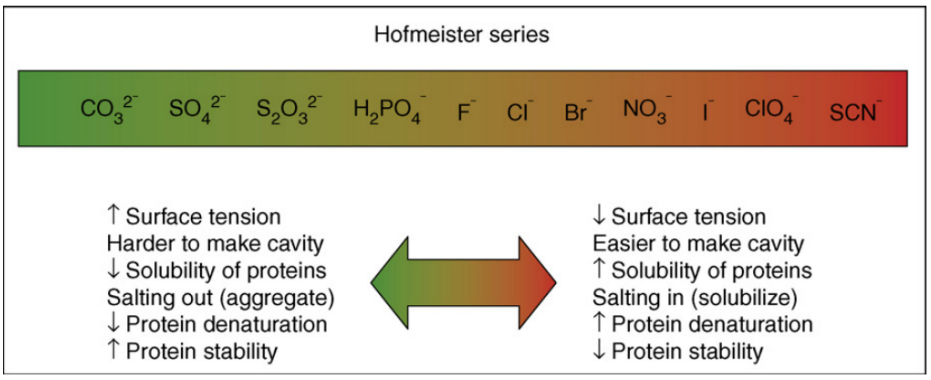

Figure 4-1. Hofmeister series and their physical effects

3. Debye−Hückel effects

Ions cluster nonspecifically around charged protein groups, weakening the protein's charge interaction. [11] This screening can destabilize attractive forces and mitigate repulsive forces as well.

4. Electroselectivity series

Ions specifically interact with charged or polar group of a peptide. Its strength is measured by the affinity to ion-exchange resins. [11]

No single mechanism determines salts' impact on self-assembly. Mostly, salt acts through an interplay of different patterns, which is strongly influenced by peptide, solvent, ion and salt concentration. The decoding of these mechanism depends on studying the effect of salt on assembly at various salt concentration for different ions. Marek et.al revealed that salt's impact

on IAPP differs with salt concentration. At lower concentration, the identity of anion impacts the rate of assembly, yet at high concentrations the rate scales with Hofmeister type ion-specific sequence. [11]

The Dutch mutant of this model peptide, Aβ(16-22) E22Q, Ac-KLVFFAQ-NH2, carries a substitution of glutamine for glutamic acid at the C-terminal position. Liang et al.[7] observed that different para-crystalline structures could form during the course of assembly. After the initial particle phase, anti-parallel out-of-register ribbons and twisted fibers emerged from within the particles. This was argued to arise from the charge repulsion of the N-terminal lysine inside the low dielectric environment of the particles. However, this was the kinetic product of the assembly, as propagation in solution gave rise to the parallel in-register fibers via template-directed mutations. The thermodynamic product, the parallel structure, was stabilized by hydrogen bonds formed between glutamines of the adjacent strands. Once the concentration of the parallel fibers reached a certain threshold, strand breakage would generate more catalytic templates such that the parallel structure propagates auto-catalytically.[12]

The conformational distribution of various β-sheet intermediates over time can be measured by IE-IR fitting experiment with the establishment of basis sets through solid state NMR[1], making it an ideal system to study the environments' influence on the self-assembly pathway. In this chapter we utilize the self-transitioning system of E22Q to decipher salt's effect on different stages of self-assembly.

Methods

Fibril Assembly in the presence of salt: [1-^{13}C]F19 Ac-KLVFFAQ powder was dissolved in 1,1,1,3,3,3-hexafluoro-2-propanol (HFIP, Sigma) and sonicated for 30min and then dried in a vacuum desiccator for 48 hours to form a clear film of monomerized peptide. The film was dissolved in 20% acetonitrile/water with 0.1 vol% TFA, bath sonicated for 10 min and different concentration of NaCl was added into each sample from a 4M stock solution. The samples were incubated at room temperature to assemble.

Attenuated Total Reflectance Fourier Transform Infrared (AT-FTIR): Aliquots (10μL) of peptide solution were dried as thin films on a Pike GaldiATR (Madison, WI, USA) ATR diamond crystal. FT-IR spectra were acquired using a Jasco FT-IR 4100 (Easton, MD, USA) at room temperature and averaging 500to 800 scans with 2 cm^{-1} resolution, using either an MCT or TGS detector, 5mm aperture and a scanning speed of 4mm/sec. Spectra were processed with zero-filling and a cosine apodization function. IE-IR spectra were normalized to the peak height of the ^{12}C band.

Fitting of Isotope-Edited FTIR Spectra:[1-^{13}C]F19 IR spectra were analyzed with Mathematica 10, with the NonlinearModelFitmodule that allowed for use of a model of the functional form: pC*parafn[x] + apC*antifn[x] + apoC*antiOutfn[x] + uC*unassemfn[x] + rC*ribbonfn[x], where pC, apC, apoC, uC and rC are scaling coefficients for the individual

reference spectra.Although the fits are a linear combination of basis set spectra, the NonlinearModelFitmoduleallowed for use of spectra that were interpolated as a function corresponding to the range from 1575 cm^{-1} to 1718 $cm^{-1.}$ In the fits, scaling coefficients were constrained to be ≥ 0.

Solid state NMR: Assembled amyloid was centrifuged at 14000 rpm under 4℃ for 20min to form a pellet. The pellet was then lyophilized to yield dry powder. TEM confirmed the presence of fibers. The NMR sample was packed into a 4 mm solid-state NMR rotor and centered using boron nitride spacers.

All NMR spectra were collected with a Bruker (Billerica, MA) Avance 600 spectrometer and a Bruker 4 mm HCN biosolids magic-angle spinning (MAS) probe. The pulse sequence for $^{13}C\{^{15}N\}$ rotational-echo double-resonance (REDOR)[13-15] consists of two parts, an S sequence that contains both ^{13}C and ^{15}N pulses, and the S_0 sequence which is identical but does not contain any ^{15}N dephasing pulses. Pulsing the dephasing ^{15}N spins interferes with the averaging of the ^{13}C-^{15}N dipolar coupling due to magic-angle spinning. This is observed in the REDOR S spectrum, where the signal decays according to both T_2 (spin-spin relaxation) and the heteronuclear ^{13}C-^{15}N dipolar coupling. Maximum dephasing occurs when the spacing between the -pulses is equal to ½ of the rotor-cycle. The sequence without any ^{15}N dephasing -pulses gives the REDOR full-echo or S_0 spectra, where the magnetization decays according to only T_2. The difference between the REDOR S and S_0 signal (ΔS) is directly proportional to the dipolar coupling, hence the distance between the two spins.

To compensate for pulse imperfections, xy8 phase cycling[16] of $^{13}C\{^{15}N\}$REDOR[13-15] 4 and 8 μs rotor-synchronized ^{13}C and ^{15}N π-pulses, respectively, and EXORCYCLE phase cycling[17,18] of the final ^{13}C Hahn-echo refocusing pulse were applied with 128 kHz Spinal64[19] ^{1}H decoupling. To minimize the effects of RF inhomogeneity[18,20], ^{13}C π-pulse power level was arrayed in the REDOR S_0 pulse sequence at long REDOR evolution times (54.4 ms, corresponding to ~544 4 μs ^{13}C π pulses) and choosing the power level that corresponded to the maximum signal intensity.[21] Similarly, ^{15}N π pulses were determined by arraying the ^{15}N power level using the REDOR S experiment at REDOR evolution times corresponding to a S/S_0 between 0.3 and 0.5.[21] To normalize for the decay due to T_2, individual REDOR curves are plotted as $\Delta S/S_0$. REDOR data points are the integrated sum of center- and sideband peaks. Error bars were calculated using the noise of each spectrum as the maximum peak height deviation. REDOR data points were fit with an analytical function[22] that describes the REDOR dephasing as a function of the heteronuclear dipolar coupling, the number of rotor cycles and the rotor period for a single observe spin in the presence of multiple dephasing spins[23]. ^{15}N dephasing spins were fixed at a distance of 9.4 Å, corresponding the distance from XRD, and REDOR curves were calculated as a function of the ^{13}C position.

MAS frequency was kept under active control at 10 kHz ± 2 Hz. The cooling and spinning air exit temperature was maintained below -1 °C to ensure MAS and RF heating did not denature the samples. ^{13}C (150.8 MHz) and ^{15}N (60.8 MHz) CP-MAS spectra before and after ^{13}C $\{^{15}N\}$ REDOR experiments confirmed that the samples did not change during the experiment.

Results

E22Q assembly is dissolved in 20%MeCN/H_2O with 0.1% TFA and the assembly process monitored in the presence of 0mM, 10mM, 25mM and 50mM, 100mM NaCl to evaluate the dependence of assembly on the dielectric of the media. The results are categorized according to different phases of self-assembly. A higher concentration of sodium chloride and divalent salt such as sodium sulfate are not included due to precipitation of peptides (data not shown).

Particle phase

To investigate the influence of sodium chloride on E22Q within the particle phase, IE-IR, CD and TEM were measured for samples with different salt gradients and these data were compared to samples without additional salt.

From TEM (**Figure 4-2 A**), all samples formed particles. The particle size increases with NaCl concentration. When zoomed in into the particle, ribbon nuclei could be observed. For the 25-100mM samples, the elongation initiated upon dissolving. CD trend (**Figure 4-2 C**) is consistent with TEM. CD shows a positive peak of 202nm and a negative peak at 233nm, corresponding to β-sheet formation. When ellipticity was plotted against the NaCl concentration at 202nm, a linear relation was observed. Within bigger particles, larger and more extended ribbons could form. When NaCl concentration was above 50mM, ribbons were seen

to be extended out of the sphere of particle within hours.

Despite the change in degree of assembly, the structure of nuclei remains constant. From IE-IR spectra (**Figure 4-2 B**), different concentrations of sodium chloride did not alter the structure of nuclei, the splitting and peak ratio correspond to anti-parallel out-of-register β-sheet. This indicates the presence of anion could not negate the electrostatic repulsion within the particle phase to directly lead to parallel nuclei formation, likely due to the inaccessibility of ion into the particle. Therefore, despite the presence of anion, within particle phase amyloid conformation is still governed predominantly by lysine-lysine repulsion.

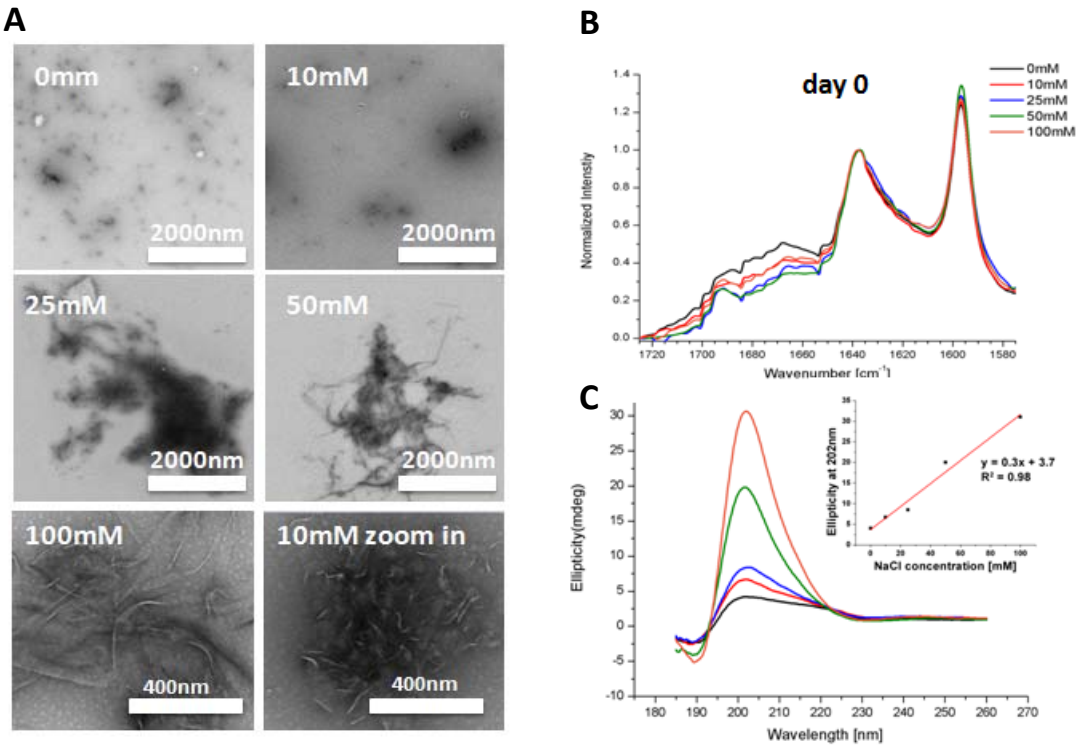

Figure 4-2. TEM, CD and IE-IR of assembly under different NaCl concentrations.
(**A**) TEM image taken 1hr after assembly. At day 0, for 0mM and 10mM salt, round particles can be observed. When zoomed in, these particles contain ribbon structures. For samples with 25mM-100mM NaCl ribbons have grown out of particle sphere and extended into the solution.
(**B**) The IE-IR signal shows these samples have identical secondary structure, which is anti-parallel out-of-register ribbon.
(**C**) CD has the same peak position for all gradients with peak at 202nm and a negative peak at 233nm. The peak intensity increases linearly with concentration of salt, meaning salt promotes the assembly.

Elongation and conversion

NaCl speeds up emergence of parallel β-sheet

Previously[12], we argued that the onset of parallel β-sheet results from a "mismatch" during the elongation process. With the presence of NaCl, ionic screening effect could lower the energy barrier of parallel β-sheet formation. Additionally, NaCl speeds up elongation rate, which is the

number of peptides adding to the end of existing template per unit time. Therefore, we hypothesize that the emergence of parallel structure would be accelerated with an increase of NaCl concentration. From previous paper, the splitting between ^{12}C and ^{13}C band decreases as the transition happens; this is used as a parameter to measure transition kinetics. For all IR spectra taken from day 1 to day 18 of the assembly under one specific NaCl condition, the splitting between ^{12}C peak (at roughly 1638 cm^{-1}) and the ^{13}C peak (at roughly 1600 cm^{-1}) was fitted to the Boltzmann function. The fitting curves at 0 mM, 10 mM, 25 mM, 50 mM and 100mM NaCl concentration are displayed in **Figure 4-3**.

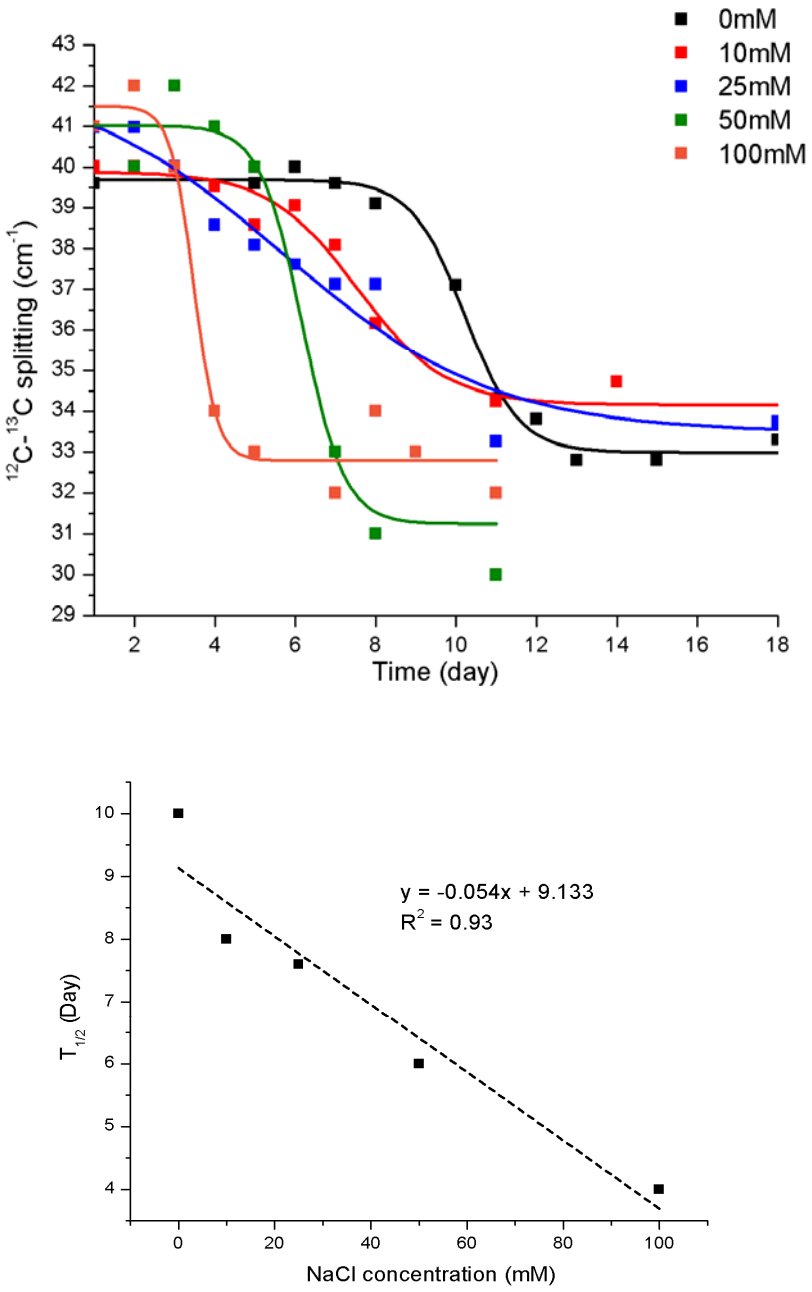

Figure 4-3. Transition kinetics of assembly under different NaCl concentrations. (A) ^{12}C-^{13}C splitting as a function of NaCl concentration fitted to Boltzmann function. (B) The half time of transition under different NaCl concentrations.

From the data, we could see the onset of conformational transition is earlier as more NaCl is present. Additionally, the transition process is speeded up by NaCl. As a result, the T1/2 of transition for 0mM, 10mM, 25mM and 50mM are 10, 7, 6, 4, 1 days separately. When the half

time of transition is plotted against NaCl concentration, a linear relationship can be observed. A higher salt concentration precipitates the peptide and is not included in the data (data not shown).

NaCl introduces heterogeneity

However, the effect of NaCl does not favor parallel conformation exclusively. Although the transition is speeded up by increased ionic strength; the transition is not as complete as the control sample. From TEM (**Figure 4-4**) and IE-IR (**Figure 4-5**), the ^{12}C and ^{13}C bands are broadened with the presence of NaCl. From previous paper, we developed IE-IR de-convolution to sort out populations of different conformations; we used that method to analyze the content of the sample and discovered that as the NaCl concentration increases, the percentage of parallel peptide decreases and anti-parallel in-register appeared to increase. Additionally, anti-parallel in-register population, which had no presence in 0mM sample, increased significantly. There is a reverse of trend for 100mM NaCl sample. The higher percentage of parallel β-sheet in 100mM sample results from the early appearance of parallel fiber whose presence dominates the assembly and replicates at a higher rate than competing conformations. It's worth noticing that the coefficient of different conformation is not known so the graph does not stand for actual percentage. Even though the beginning of the assembly process can be characterized by CD, as the assembly continues, peptides stated to form gel-like particles and the CD signal disappeared

due to diffraction (data not shown).

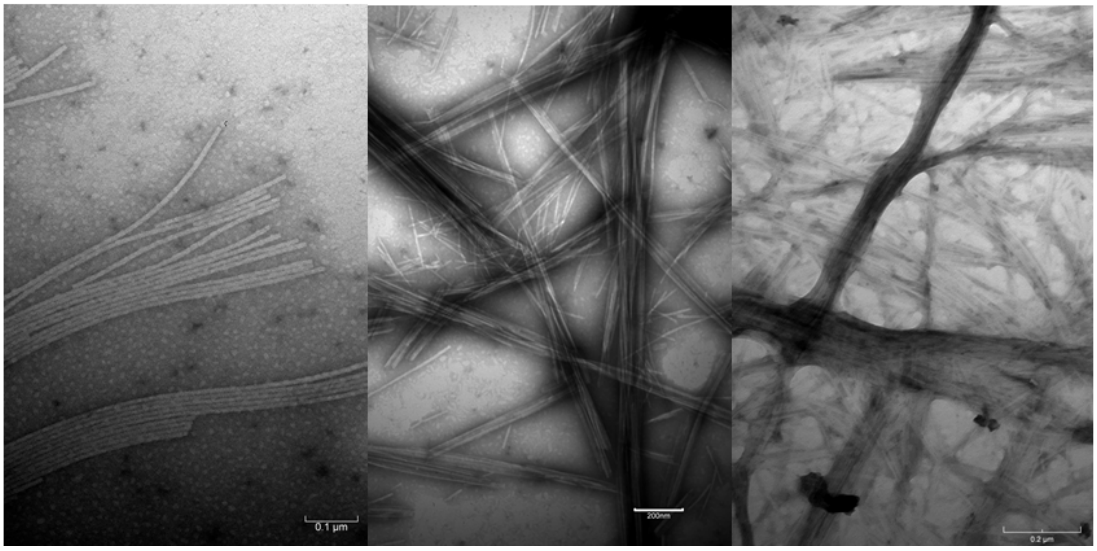

Figure 4-4. TEM image of stabilized fiber under 0mM, 50mM, and 100mM NaCl

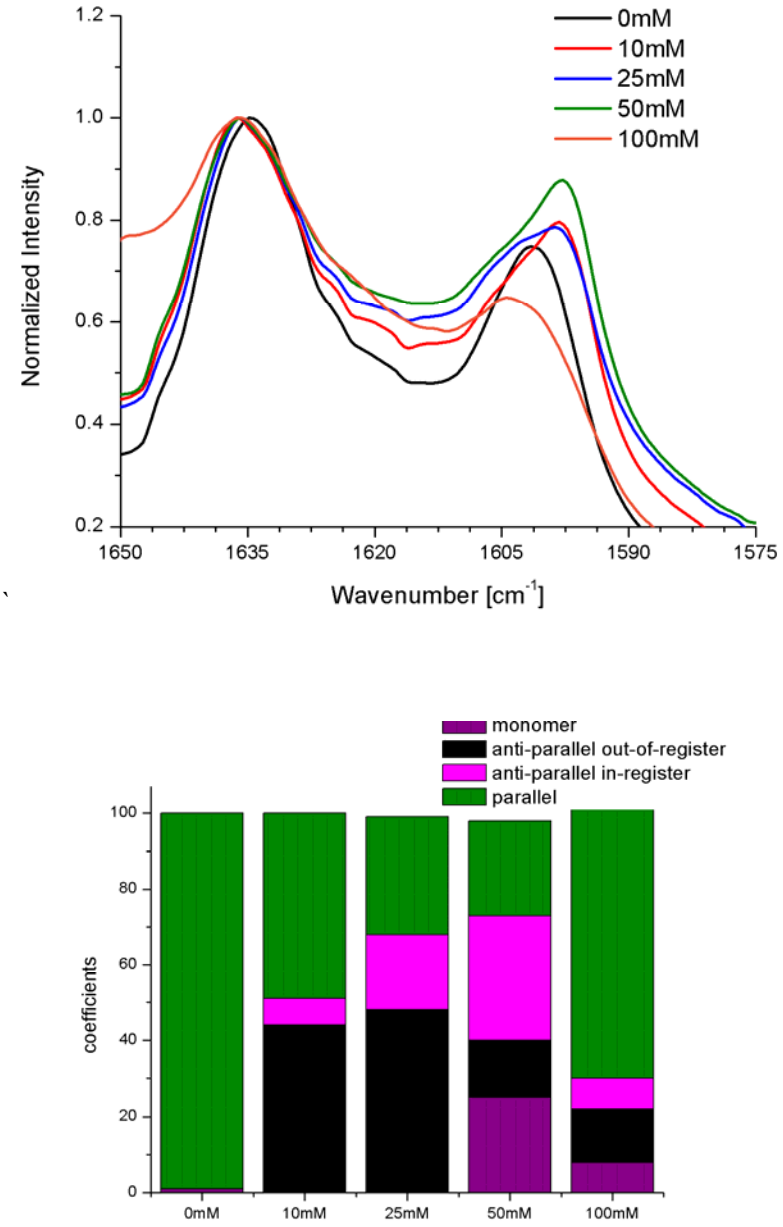

Figure 4-5. IE-IR of the stabilized sample under different NaCl concentrations (top). Distribution of various conformations under different NaCl concentrations (bottom).

The IE-IR data provides a fast and economic way to examine different conformations yet the accuracy is limited. The IE-IR spectra of high NaCl samples exhibit low signal and high noise, therefore is less reliable than no-salt sample. Data had to go through water elimination and sometimes smoothing on Jasco FT-IR 4100 software. Therefore, IE-IR and IR fitting can be used to observe a pattern but to obtain more accurate conformation distribution data and

substantiate IR fitting result, REDOR and DRAWS solid-state NMR experiments need to be conducted on E22Q assembled under NaCl. We chose 100mM concentration to increase the concentration of peptide and salt helps the preparation of the sample.

The specific registry can be defined via the rate of double-quantum coherence dissipation through homonuclear dipolar coupling in ^{13}C DQF-DRAWS solid –state NMR experiments. [12]Using infinite array approximation and double quantum relaxation T_2DQ = 11.7ms, the solid-state NMR data for [1-^{13}C] enriched L17 peptide assemblies defined the percentage of parallel in-register strand within the bulk assembly. From **figure 4-6 C**, the ^{13}C DRAWS DQ efficiency of sample with 100mM NaCl (red curve in **figure 4-6 A**) is reduced by 26 ± 3% compared to the no salt sample (black curve in **figure 4-6 A**), indicating the reduced percentage of parallel β-sheet when the assembly system reaches equilibrium. and solid-state NMR $^{13}C\{^{15}N\}$REDOR[13] analyses with [1-^{13}C]L17 and [^{15}N]A21 enriched peptides showing out-of-register (9 ± 3%) and in-register (7 ± 3%) anti-parallel assemblies, leaving 10% of the peptide existing in other forms (natural abundance). The solid-state NMR experiment supports IR fitting in deciphering conformational distribution of different confirmations and substantiate the existence of anti-parallel strand orientation.

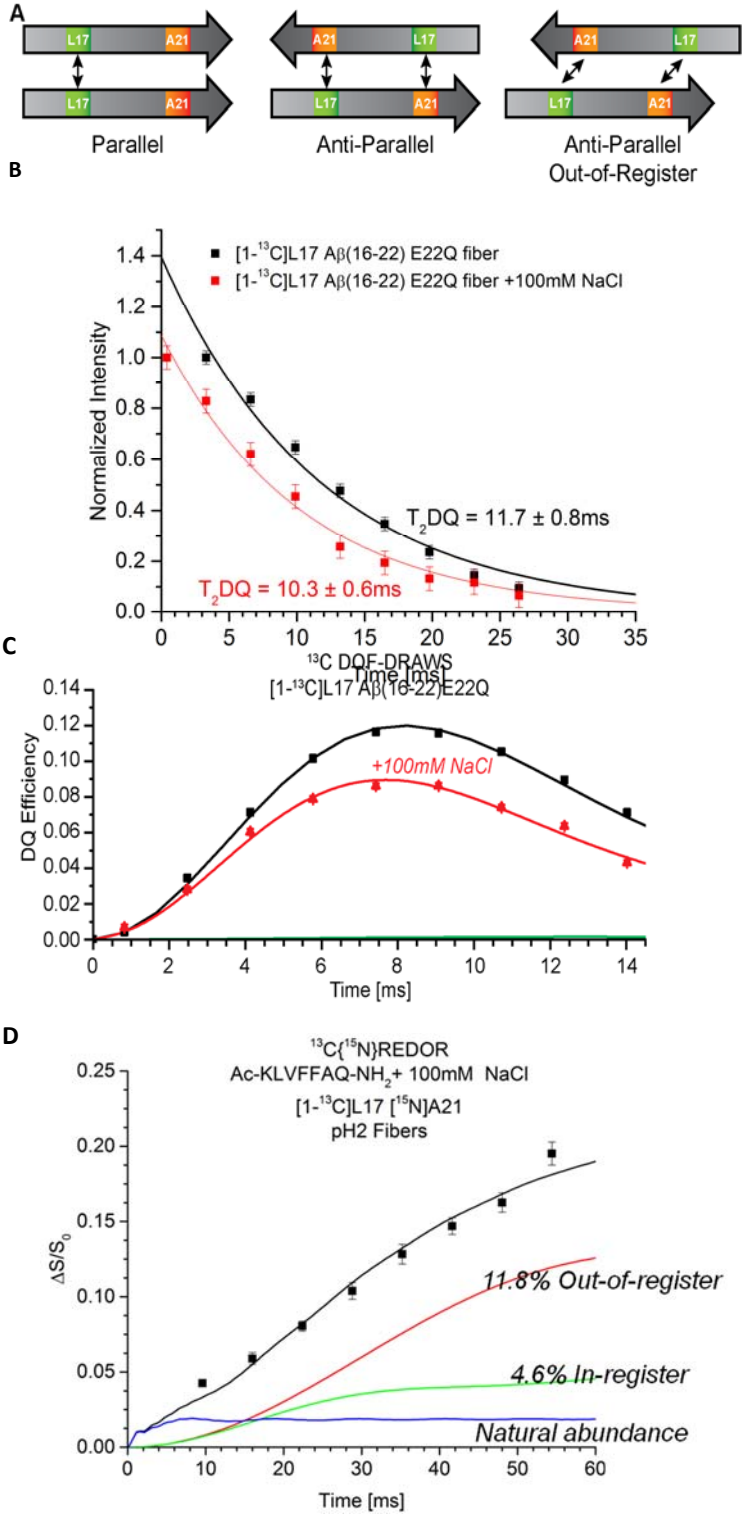

Figure 4-6. β-sheet registry in Aβ(16-22)E22Q assemblies.
(**A**) Cartoons showing positions of ^{13}C (green) and ^{15}N (orange) enriched residues in β-sheet registry.
(**B**) ^{13}C Double Quantum relaxation (T_2DQ) of [1-^{13}C]L17 Aβ(16-22)E22Q assembled at acidic pH (black) and [1-^{13}C]L17 [^{15}N]A21 Aβ(16-22)E22Q assembled at acidic pH in the presence of 100 mM NaCl (red). T_2DQ was measured by inserting a composite 180° pulse between DRAWS pulses. Solid line is best fit of a monotonically decaying exponential to the data points.

(**C**) ^{13}C DQF-DRAWS for [1-^{13}C]L17 Aβ (16-22)E22Q assembled without (black) and with (red) 100mM NaCl.
(**D**) ^{13}C{^{15}N}REDOR dephasing for [1-^{13}C]L17 [^{15}N]A21 Aβ (16-22)E22Q assembled in the presence of 100mM NaCl. Solid line is calculated dephasing for anti-parallel β-strands that are in-register (7%) and out-of-register (9%). REDOR plateau is consistent with 16% of peptides assembled as anti-parallel β-sheets.

Discussion

The data suggests that NaCl impact assembly at different phases. At the nucleation phase, NaCl doesn't impact the secondary structure of nuclei but increases particle size and nucleation rate. For samples with NaCl concentration higher than 50mM, elongation happened within an hour and long extended ribbons can be observed. The degree of assembly measured by CD is in direct proportion to NaCl concentration. The increase in assembly kinetics is likely a result of Hofmeister effect as a linear relationship exist between NaCl concentration and degree of assembly, meaning the NaCl is impacting the property of solution instead of around solutes. Other mechanisms involving salt's impact on amyloid should plateau due to saturation.

Within elongation phase, due to charge screening, NaCl speeds up transition from anti-parallel to parallel β-sheet. Previously, we reported the appearance of parallel nucleus is from a mismatch or mutation during the elongation process. As amyloids elongate through a dock and lock mechanism in which a peptide approaches an existing amyloid template, searches through energy landscape and eventually lock into the structure of the template. [25]With the presence of NaCl, the formation of parallel structure is less energetically costly due to screening.

Additionally, the elongation rate is faster. Therefore, the possibility of a peptide docking as parallel is higher than that from no NaCl condition. Therefore, the data substantiates our original hypothesis.

However, despite the higher rate of higher NaCl samples, the transition is incomplete: at equilibrium, anti-parallel out-of-register conformation stills remained and a new conformation: anti-parallel in-register emerged. The heterogeneity with the introduction of NaCl is in line with multiple studies.[4,26,27] Heterogeneity triggered by NaCl could result from multiple factors. The increase of structural variety could result from alternative assembly pathway or secondary nucleation. Salt disrupts multiple forces leading to nucleation including hydrogen bond, electrostatic repulsion, dielectric constant of the solution, and particle size therefore alternative assembly mechanism could occur. The bundling could easily serve as a surface to induce secondary nucleation. With NaCl screening the charge, peptide precipitation could also occur and the disorganized structure could be detected as corresponding to multiple conformations.

Kinetic trapping mechanism can be used to explain the preservation of different confirmations. The high strain energy of changing conformation within the amyloid fiber, conformational transition must go through disassociation and re-association of monomer with amyloid fiber. Therefore, conformational transition requires free monomer in solution as well as free-ends from both intermediate and thermodynamic products. The preservation of structural intermediates can be explained accordingly: the lower dielectric constant shifts the equilibrium to favor amyloid and decrease free monomer concentration. It has been reported that the monomer of β2-Microglobulin is depleted by salt above 40mM NaCl [24]; additionally, the

bundling of fibers could decrease solvent exposed surface of amyloid, increasing stability of pre-formed amyloid. The precipitated peptide is known to trap amyloid and monomers don't disassociate back into solution. These factors trapped the intermediates and increasing heterogeneity within the system.

IE-IR provides significant amount of information on transition kinetics and the shape of transition is of interest: for 0mM, 50mM and 100mM, a sigmoidal growth pattern is observed with clear flat region at the beginning and end, yet for 25mM and 50mM, no clear lag phase is observed and the transition is not as corporative. This can be explained by the interplay of multiple functions of salt. First, a pattern can only be observed when the transition is predominately from one conformation to the other. The appearance of multiple species complicates the conformation landscape. For samples with 0 and 10mM NaCl, the anti-parallel out-of-register ribbon persists for a long time, creating the initial lag phase, and the transition is mainly from anti-parallel out-of-register to parallel. The pattern is not as obvious in 25mM and 50mM sample as more NaCl promotes the emergence of different conformations whose impact broadens ^{12}C and ^{13}C. With 100mM NaCl sample, parallel conformation nucleates at an earlier time point. This thermodynamically most stable product dominates the assembly and elongates self-catalytically, reducing the percentage of other intermediates, therefore restoring the splitting pattern to a sigmoidal change.

Conclusion

E22Q system with isotope enrichment on F19 position is a robust system to be used to quantifiably characterize the conformation composition of amyloid. The splitting distance between ^{12}C and ^{13}C bands serves as the parameter easy to obtain. Here the system is used to study how environmental factors influence amyloid self-assembly.

Our data showed that the presence of NaCl could facilitate oligomerization and the onset of conformational transition of E22Q system. However, the transition could not be completed and heterogeneity arises with NaCl. We demonstrate under specific conditions the effect of kinetic and thermodynamic modulators can be biased leading to the formation of different products and provide a better understanding of how environmental factors impact amyloid self-assembly.

References

(1) Smith, J. E.; Liang, C.; Tseng, M.; Li, N.; Li, S.; Mowles, A. K.; Mehta, A. K.; Lynn, D. G. Defining the Dynamic Conformational Networks of Cross- Peptide Assembly. *Isr J Chem* **2015**, *55*, 763-769.

(2) Morris, R. J.; Eden, K.; Yarwood, R.; Jourdain, L.; Allen, R. J.; Macphee, C. E. Mechanistic and environmental control of the prevalence and lifetime of amyloid oligomers.

Nat Commun **2013**, *4*, 1891.

(3) Goldblatt, G.; Matos, J. O.; Gornto, J.; Tatulian, S. A. Isotope-edited FTIR reveals distinct aggregation and structural behaviors of unmodified and pyroglutamylated amyloid beta peptides. *Phys Chem Chem Phys* **2015**, *17*, 32149-32160.

(4) Jain, S.; Udgaonkar, J. B. Salt-induced modulation of the pathway of amyloid fibril formation by the mouse prion protein. *Biochemistry* **2010**, *49*, 7615-7624.

(5) Owczarz, M.; Arosio, P. Sulfate anion delays the self-assembly of human insulin by modifying the aggregation pathway. *Biophys J* **2014**, *107*, 197-207.

(6) Muzaffar, M.; Ahmad, A. The mechanism of enhanced insulin amyloid fibril formation by NaCl is better explained by a conformational change model. *PLoS One* **2011**, *6*, e27906.

(7) Ozbas, B.; Kretsinger, J.; Rajagopal, K.; Schneider, J. P.; Pochan, D. J. Salt-triggered peptide folding and consequent self-assembly into hydrogels with tunable modulus. *Macromolecules* **2004**, *37*, 7331-7337.

(8) Ahmed, M.; Davis, J.; Aucoin, D.; Sato, T.; Ahuja, S.; Aimoto, S.; Elliott, J. I.; Van Nostrand, W. E.; Smith, S. O. Structural conversion of neurotoxic amyloid-beta(1-42) oligomers to fibrils. *Nat Struct Mol Biol* **2010**, *17*, 561-567.

(9) Baldwin, R. L. How Hofmeister ion interactions affect protein stability. *Biophys J* **1996**, *71*, 2056-2063.

(10) Zhang, Y. J.; Cremer, P. S. Interactions between macromolecules and ions: the Hofmeister series. *Curr Opin Chem Biol* **2006**, *10*, 658-663.

(11) Marek, P. J.; Patsalo, V.; Green, D. F.; Raleigh, D. P. Ionic strength effects on amyloid

formation by amylin are a complicated interplay among Debye screening, ion selectivity, and Hofmeister effects. *Biochemistry* **2012**, *51*, 8478-8490.

(12) Liang, C.; Ni, R.; Smith, J. E.; Childers, W. S.; Mehta, A. K.; Lynn, D. G. Kinetic intermediates in amyloid assembly. *J Am Chem Soc* **2014**, *136*, 15146-15149.

(13) Gullion, T.; Schaefer, J. Rotational-Echo Double-Resonance NMR. *J Magn Reson* **1989**, *81*, 196-200.

(14) Gullion, T.; Schaefer, J. Detection of Weak Heteronuclear Dipolar Coupling by Rotational-Echo Double-Resonance NMR. *Adv Magn Reson* **1989**, *13*, 57-84.

(15) Christensen, A. M.; Schaefer, J. Solid-state NMR determination of intra- and intermolecular ^{31}P-^{13}C distances for shikimate 3-phosphate and [1-^{13}C]glyphosate bound to enolpyruvylshikimate-3-phosphate synthase. *Biochemistry* **1993**, *32*, 2868-2873.

(16) Gullion, T.; Baker, D. B.; Conradi, M. S. New, Compensated Carr-Purcell Sequences. *J Magn Reson* **1990**, *89*, 479-484.

(17) Rance, M.; Byrd, R. A. Obtaining High-Fidelity Spin-1/2 Powder Spectra in Anisotropic Media - Phase-Cycled Hahn Echo Spectroscopy. *J Magn Reson* **1983**, *52*, 221-240.

(18) Sinha, N.; Schmidt-Rohr, K.; Hong, M. Compensation for pulse imperfections in rotational-echo double-resonance NMR by composite pulses and EXORCYCLE. *J Magn Reson* **2004**, *168*, 358-365.

(19) Fung, B. M.; Khitrin, A. K.; Ermolaev, K. An improved broadband decoupling sequence for liquid crystals and solids. *J Magn Reson* **2000**, *142*, 97-101.

(20) Weldeghiorghis, T. K.; Schaefer, J. Compensating for pulse imperfections in REDOR. *J Magn Reson* **2003**, *165*, 230-236.

(21) Ni, R.; Childers, W. S.; Hardcastle, K. I.; Mehta, A. K.; Lynn, D. G. Remodeling Cross-β Nanotube Surfaces with Peptide/Lipid Chimeras. *Angew Chem, Int Ed* **2012**, *51*, 6635-6638.

(22) Mueller, K. T.; Jarvie, T. P.; Aurentz, D. J.; RobertS, B. W. The REDOR transform: direct calculation of internuclear couplings from dipolar-dephasing NMR data. *Chem. Phys. Lett.* **1995**, *242*, 535-542.

(23) Goetz, J. M.; Schaefer, J. REDOR Dephasing by Multiple Spins in the Presence of Molecular Motion. *J Magn Reson* **1997**, *127*, 147-154.

(24) Yanagi, K.; Sakurai, K.; Yoshimura, Y.; Konuma, T.; Lee, Y. H.; Sugase, K.; Ikegami, T.; Naiki, H.; Goto, Y. The monomer-seed interaction mechanism in the formation of the beta2-microglobulin amyloid fibril clarified by solution NMR techniques. *J Mol Biol* **2012**, *422*, 390-402.

(25) Esler, W. P.; Stimson, E. R.; Jennings, J. M.; Vinters, H. V.; Ghilardi, J. R.; Lee, J. P.; Mantyh, P. W.; Maggio, J. E. Alzheimer's disease amyloid propagation by a template-dependent dock-lock mechanism. *Biochemistry* **2000**, *39*, 6288-6295.

(26) Gosal, W. S.; Morten, I. J.; Hewitt, E. W.; Smith, D. A.; Thomson, N. H.; Radford, S. E. Competing pathways determine fibril morphology in the self-assembly of beta2-microglobulin into amyloid. *J Mol Biol* **2005**, *351*, 850-864.

(27) Morel, B.; Varela, L.; Azuaga, A. I.; Conejero-Lara, F. Environmental conditions affect the kinetics of nucleation of amyloid fibrils and determine their morphology. *Biophys J* **2010**, *99*, 3801-3810.

Chapter 5 Positional dependence of Q on amyloid self-assembly

Introduction

In natural proteins, single mutation in amino acid sequence could lead to significant differences in structure and function, and so is the case with amyloid self-assembly[1-3]. Previously we have published that Q track causes Aβ (16-22) E22Q to go through anti-parallel intermediate before transitioning to parallel conformation. . Here we show the position of Q in peptide sequence impacts dramatically transition times and structures of amyloid aggregates. The difference is detected by isotope edited infrared spectroscopy (IE-IR), demonstrating that IE-IR is not only sensitive to amyloid secondary structures but also to large scale structural differences.

Aβ Dutch mutant, with a single mutation of glutamic acid (E) to glutamine (Q) mutation, causes significantly increase of toxicity of the protein. Studies have shown a higher proteolysis resistance, enhanced cellular binding, and lowered efflux transporter affinity of Dutch mutant, resulting in a cerebral accumulation.[4] Patients with Aβ Dutch mutant show severe hereditary cerebral hemorrhage.

The fact that a single amino acid point mutation changes the toxicity of Aβ so much is worth

significant attention. Models have shown that the E22–K28 salt bridge could stabilize the internal β-sheet structure[5] and the replacement of E with uncharged Q, could cause structural shift. Additionally, Q present in the side chain can form inter-sheet hydrogen bonds, adding more conformational constrains to the final structure of amyloid[6].

In previous chapters I have shown how Q hydrogen bonds can outweigh the electrostatic forces in dictating a parallel β-sheet formation. Here I study the effect of the position of Q on along the peptide strand impacts the transition and kinetics of the amyloid growth Kinetics of transition are mainly measured using IE-IR and studying the structure of E22Q using TEM and powder diffraction.

Methods

Fibril Assembly: Lyophilized Peptides were dissolved in 1,1,1,3,3,3-hexafluoro-2-propanol (HFIP, Sigma) and sonicated for 30 min, then dried under a stream of dry N_2 gas or under vacuum. The resultant clear film was dissolved in 20% acetonitrile/water (0.1 vol% TFA), bath sonicated for at least 10 min and, unless indicated, incubated at room temperature for assembly. To produce unassembled peptide, lyophilized peptide was dissolved in 1,1,1,3,3,3-hexafluoro-2-propanol (HFIP, Sigma) and sonicated for 30 min and stored at room temperature in HFIP.

Attenuated Total Reflectance Fourier Transform Infrared (AT-FTIR): Aliquots (10μL) of peptide solution were dried as thin films on an Pike GaldiATR (Madison, WI, USA) ATR

diamond crystal. FT-IR spectra were acquired using a Jasco FT-IR 4100 (Easton, MD, USA) at room temperature and averaging 500 to 800 scans with 2 cm-1 resolution, using either an MCT or TGS detector, 5mm aperture and a scanning speed of 4mm/sec. Spectra were processed with zero-filling and a cosine apodization function. IE-IR spectra were normalized to the peak height of the 12C band.

Transmission Electron Microscopy (TEM): A TEM copper grid with a 200 mesh carbon support (Electron Microscopy Sciences) was covered with 10 μL of a diluted peptide solution (0.05 mM to 0.1 mM) for 1 min before wicking the excess solution with filter paper. 10 μL of the staining solution, either (2% uranyl acetate, Sigma-Aldrich, or methylamine tungstate, Ted Pella, Inc) was added and incubated for 2 min, excess solution was wicked away, and the grids were placed in desiccators to dry under vacuum overnight.

Results

Morphology and transition kinetics of different mutants

Using Aβ(16-22) as model system, three different congeners of Aβ(16-22)E22Q were designed : L17Q ([1-^{13}C]F19 Ac-^{16}KQVFFA^{22}E-NH_2), V18Q ([1-^{13}C]F19 Ac-^{16}KLQFFA^{22}E-NH_2), and A21Q ([1-^{13}C]F19 Ac-^{16}KLVFFQ^{22}E- NH_2). [1-^{13}C]F19 Aβ(16-22) E22Q itself serves as the control. (**Figure 5-1**)

Figure 5-1. Peptide's design of glutamine scan. Red signifies the position of [1-^{13}C] isotope enrichment, glutamine is colored by orange.

Each sample was pre-HFIP treated, dissolved in 20% acetonitrile/water with 0.1% TFA at 1mM concentration and monitored daily at room temperature. The changes in the assemblies overtime were monitored using both transmission electron microscopy (TEM) and isotope edited Infrared spectroscopy (IE-IR).

From IE-IR data in **figure 5-2**, all mutants go through a conformation transition demonstrated by drastic shift in wavenumber and band intensity. Additionally, they stabilized into fibers with width around 10nm. These traits resemble E22Q's transition in earlier chapters. Therefore it's highly likely all congeners go through a similar transition from anti-parallel to parallel.

On the other hand, various assemblies differ drastically both in transition kinetics and final IE-IR spectra. The transition time of L17Q is over three weeks, which doubles that of E22Q while A21Q and V18Q takes a few days to finish transition. [1-^{13}C]F19 L17Q has two bands similar to [1-^{13}C] F19 E22Q yet the ^{12}C band for L17Q is more red shifted and the ^{13}C band is more blue-shifted. The ^{13}C/^{12}C band ratio of [1-^{13}C] F19 A21Q is 1.17 while the ratio is less than 1 for the rest of congeners. V18Q exhibit an additional small band around 1620cm^{-1}.

Despite the ^{13}C enrichment being on the same position and the possibility that all peptides go through an anti-parallel to parallel transition, the IE-IR spectra of different variants are drastically different, indicating a structural difference above strand orientation or secondary structure. Differences on a higher order molecular order could result from bundling, twisting and β-sheet stacking. Such differences manifest from TEM images.

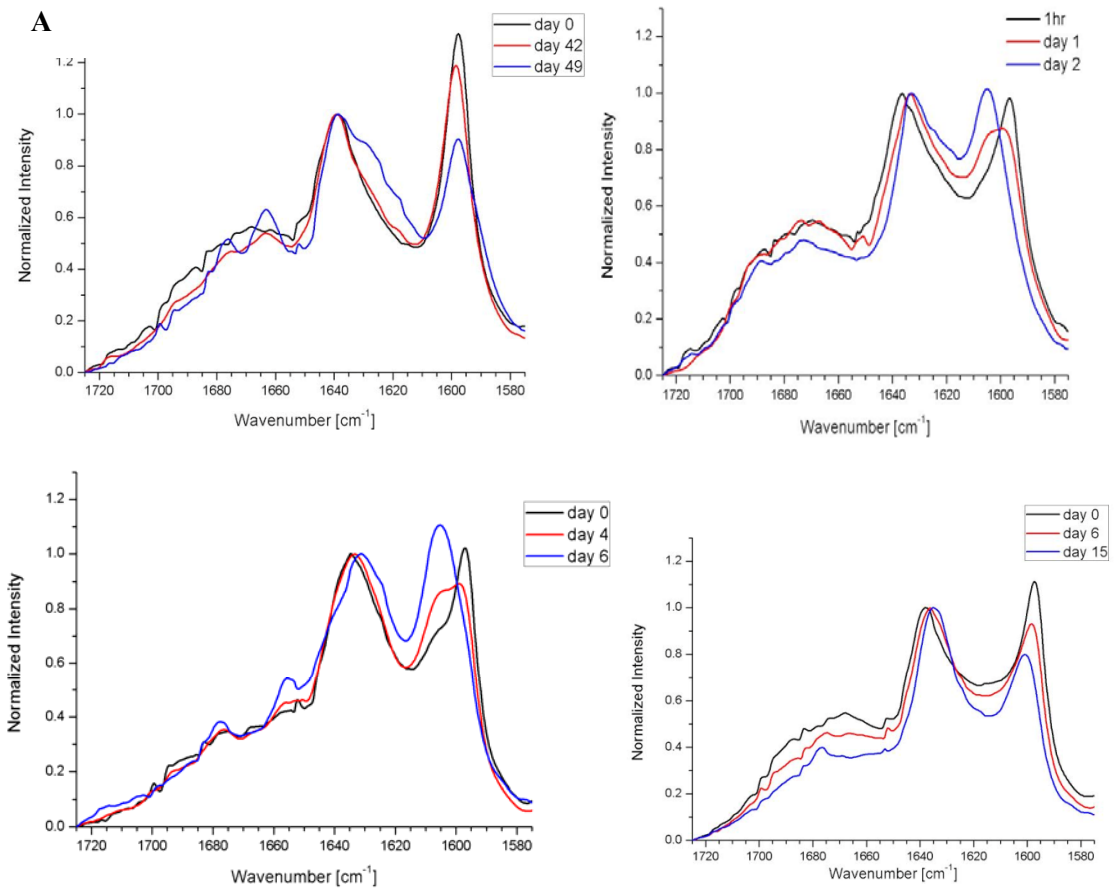

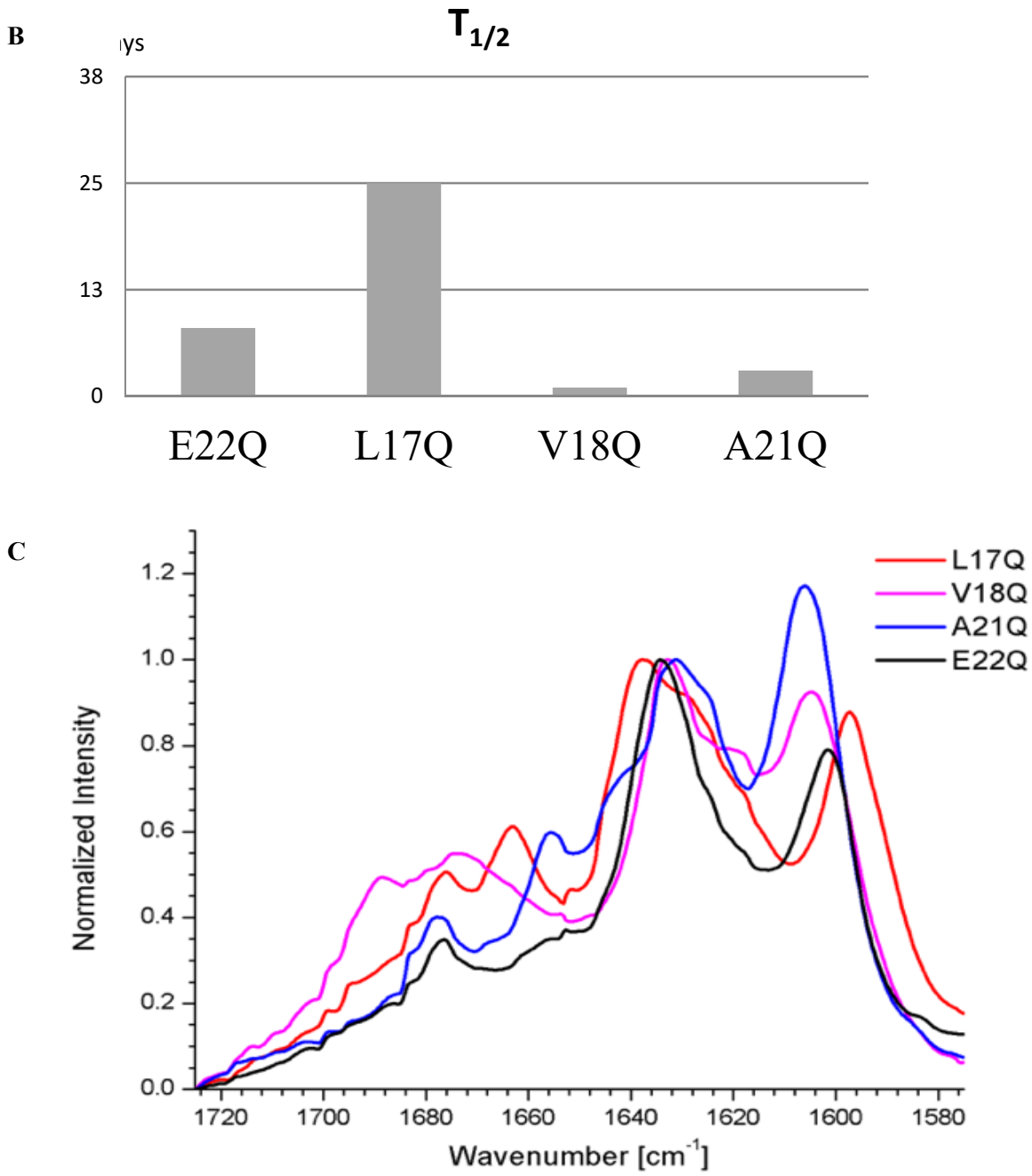

Figure 5-2. (**A**)IE-IR transition of [1-^{13}C]F19 L17Q, [1-^{13}C]F19 V18Q, [1-^{13}C]F19 A21Q and [1-^{13}C]F19 E22Q. (**B**) $T_{1/2}$ of different mutants. (**C**) Comparison of IE-IR signal of different mutants.

TEM was taken for mature assemblies of different variants. **Figure 5-3** shows that, both L17Q and V18Q can form individual fibers with width around 10nm, identical to E22Q. A21Q does

not form individual fibers but instead form bundled aggregates with a high degree of lateral association. A zoom-in of the fibers reveals more structural details: For E22Q, a rough surface is shown and fibers are separated into two populations of distinctive widths: 5nm and 11nm, yet no clear bundling and twisting can be observed; for L17, bundled, twisted trimers are clearly seen on stained images; for V18 mutants, largely dimers and occasionally tetramers are observed. These data support a higher level structural difference in terms of protofiber association. This shows the sensitivity of IE-IR on amyloid beta structures as the influence of twisting and bundling could also be shown on the spectra.

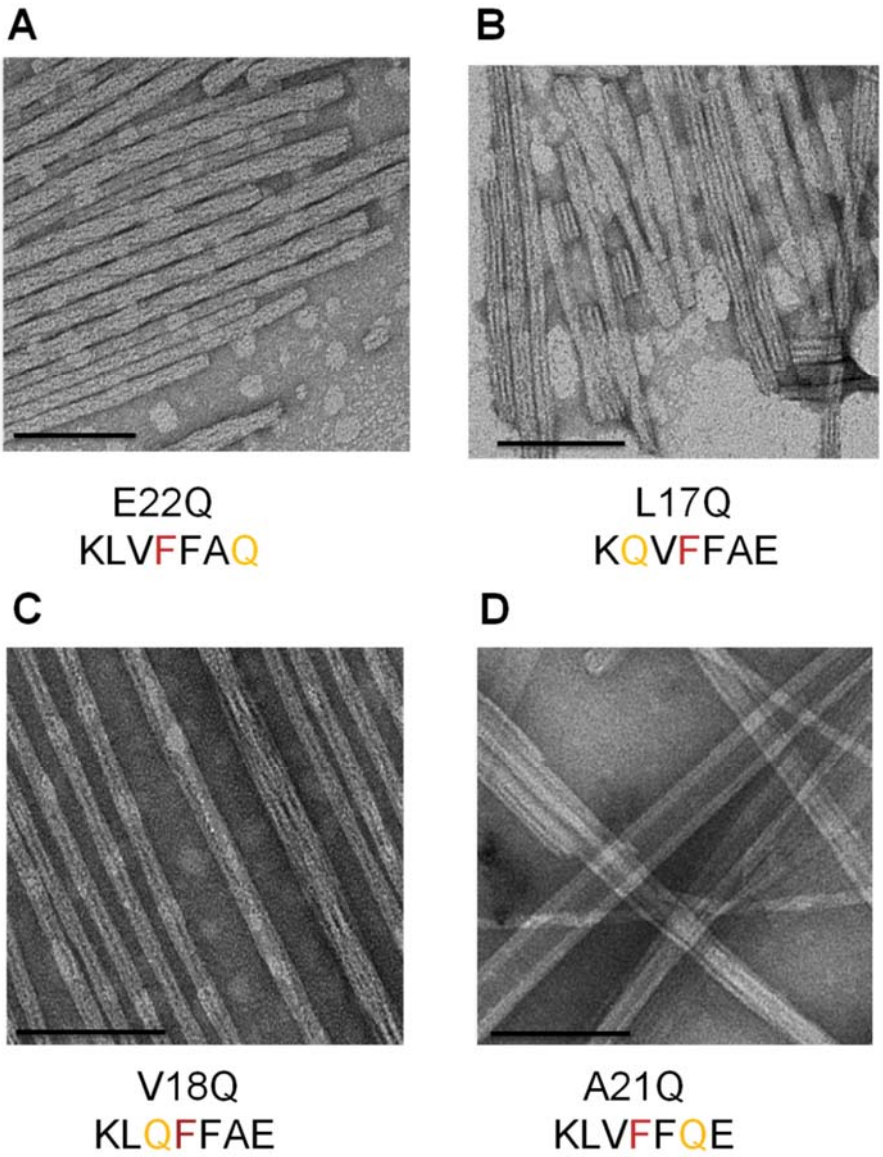

Figure 5-3. Different mutants exhibit various structures. TEM picture of (**A**) KLVFFAQ, (**B**) KQVFFAE (**C**) KLQFFAE (**D**) KLVFFQE. Scale bar 100nm

The difference in structure can be explained by understanding Q as a "zipper" to lock peptides position. The most rigid part of the peptide is around glutamine and the conformational restrain exerted by Q-track is likely to control the alignment of the peptide. This effect is enhanced over the long range of the fiber. Such difference could also result from β-sheet stacking, where different sheet stacking patterns could result from drastically different structural features.

The difference in T1/2 can be explained by competing forces between electrostatic interaction between lysines and hydrogen bonding formation between glutamines.

For L17Q, the lysine and glutamine are placed in close proximity. The hydrogen bond formation between glutamines can be constantly blocked by the electrostatic repulsion from lysines, which could decrease the collision rate between glutamines and destabilize the newly formed hydrogen bonds, prolonging the transition time.

It's likely the faster transition kinetics of V18Q and A21Q result from their proximity to central di-phenylalanine (FF). The assembly is largely driven by the F-F interaction, therefore bringing higher collision rate for the 18^{th} and 21^{st} position of Aβ (16-22). This increases the collision rate for the glutamines of V18Q and A21Q, shortening the transition time.

Mutation at the nucleating core of Aβ(16-22): F19Q and F20Q

Di-phenylalanine has been extensively studied and is the crucial driving force for Aβ (16-22) assembly[7-9]. Deletion of Phenylalanine would lead to de-stabilization of assembly and inhibited growth. Replacing central F with Q would replace van der Waals force between phenylalanines with inter-strand H bonding of glutamines. Here two mutants were designed, F19Q and F20Q. For F19Q, the isotope cannot be enriched on glutamine as it's impossible to selectively enrich side backbone carbonyl but not side chain.

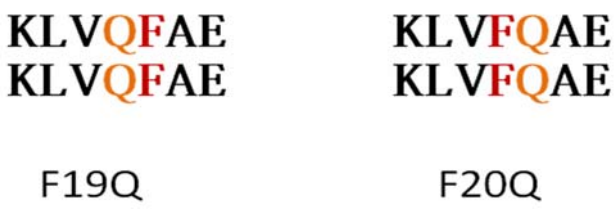

Figure 5-4. Molecular sequence of F19Q and F20Q. Red signifies the position of [1-^{13}C] isotope enrichment, glutamine is colored by orange.

Despite the identical chemical composition and replacement at similar positions, F19Q and F20Q possess drastically different transition kinetics. F19Q that underwent HFIP treatment remained monomer and didn't transition for over months (**Figure 5-6 A**). The kinetics shown below is from a sample without HFIP treatment, which transitioned after 40 days (**Figure 5-6 B**). On the other hand, F20Q that went through HFIP treatment assemble into final conformation immediately (**Figure 5-6 C**). The IR of image B and C is normalized to amide A which is least impacted by conformation and reflects the degree of assembly. The high intensity of F20Q's IR band on day zero also supports its rapid rate of assembly. The transition time of F19Q compared to F20Q is shown in **Figure 5-6 D**.

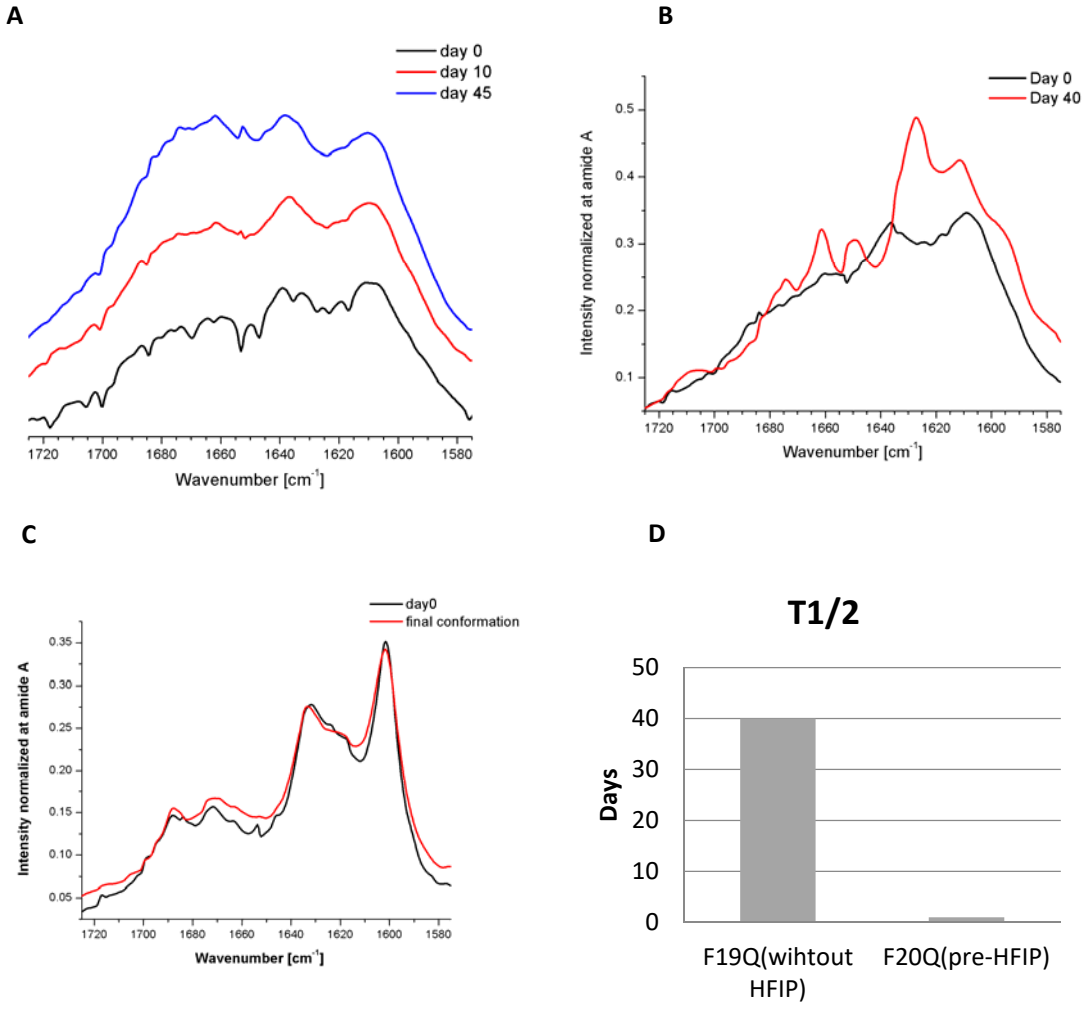

Figure 5-5. IE-IR shows different transition kinetics for F19Q and F20Q.
(**A**)F19Q with pre-HFIP treatment doesn't transition into thermodynamic conformation for months.
(**B**)F19Q without HFIP transitions into thermodynamic conformation after over 1 month.
(**C**) F20Q assembles into thermodynamic product immediately.
(**D**) Comparison of T1/2 for F19Q and F20Q.

TEM images also reveal their distinct morphological transition. For F19Q (**Figure 5-6 A**), instead of forming ribbons, the intermediate state remains bundled and heterogeneous. Such bundling explains the long period of transition time for F19Q as it prevents the intermediates from dissolving and assembling into thermodynamically stable conformations. After transition, its morphology is similar to E22Q with 10nm width and lack of clear striation. Mature fibers

of F20Q exhibits clear striation and twist (**Figure 5-6 D**). The diameter various with the number of protofibers within each bundle. This pattern can be observed on day 0 (**Figure 5-6 C**) whose IR spectrum is almost identical to mature fibers. TEM shows loose ends of fiber bundling, suggesting the maturation process for F20Q is bundle formation instead of β-sheet arrangements.

Such difference is surprising as both mutants possess such high similarity and the interaction would not differ within β-sheet level. It's likely that the difference lies in the β-sheet stacking.

A

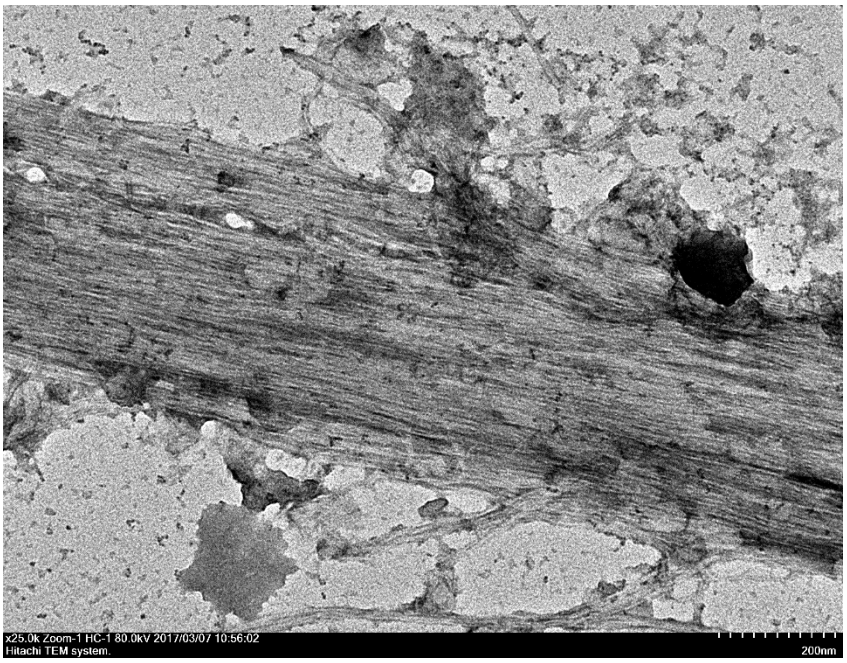
x25.0k Zoom-1 HC-1 80.0kV 2017/03/07 10:56:02
Hitachi TEM system.
200nm

B

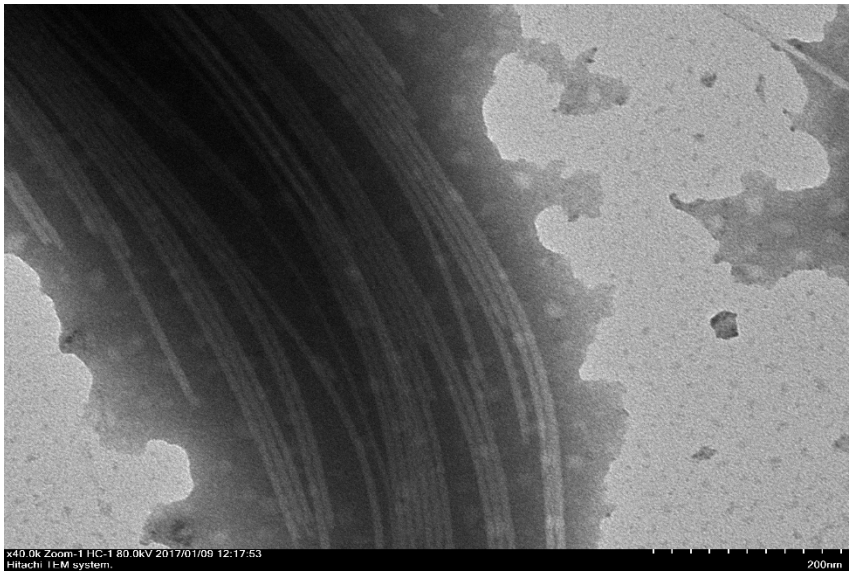
x40.0k Zoom-1 HC-1 80.0kV 2017/01/09 12:17:53
Hitachi TEM system.
200nm

C

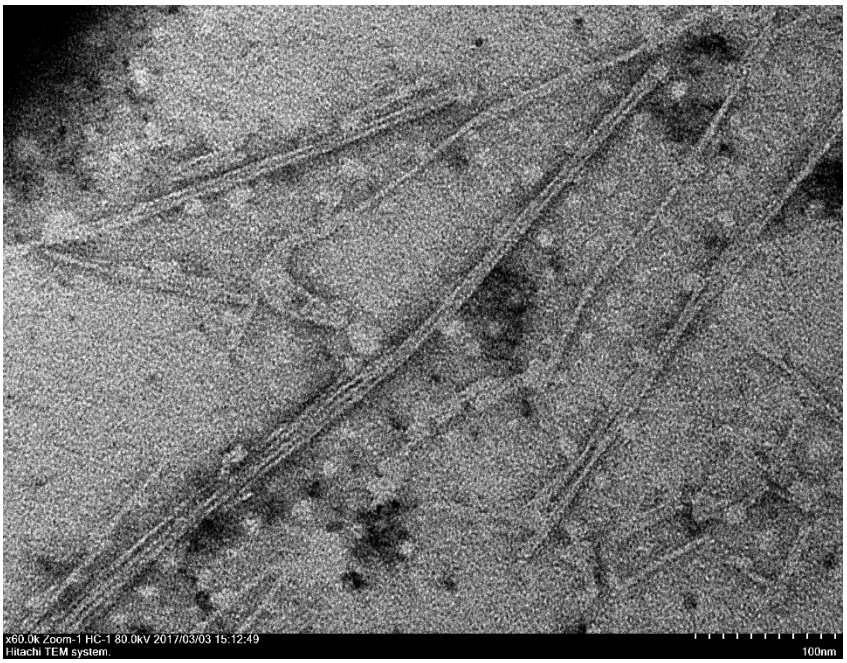

D

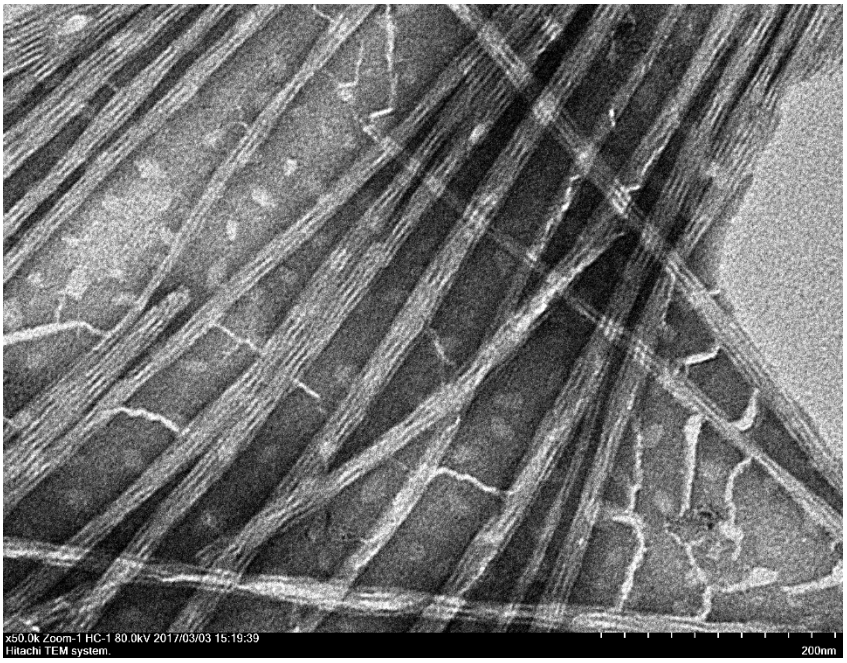

Figure 5-6. TEM shows the morphology of F19Q and F20Q overtime.
(**A**) F19Q upon assembly bundles heavily;
(**B**) Mature F19Q is homogenous fiber with width around 10nm,
(**C**) F20Q assembled into twisted fibers who started bundling;
(**D**) mature F20Q bundles heavily with periodic twist.

Using Solid-state NMR to confirm the conformation of different variants.

The similarity between E22Q and various mutants in terms of Q track IR signal, morphology

revealed by TEM and the conformational transitions suggest their strand orientation to be parallel. However, the most conclusive experimental method for such statement is the solid-state NMR. REDOR and DRAWS experiments will be conducted in the future to show definitively the percentage of various conformations.

Pattern analysis

The IE-IR of [1-^{13}C]F19 L17Q, V18Q, F20Q, A21Q and E22Q were compiled and analyzed since their isotope enrichment are at the same position. The peak positons and heights are shown in the table below.

Table 5-2. Band wavenumber and height ratio for Q congeners.

	C^{12} position	**C^{12} height**	**C^{13} position**	**C^{13} height**	**C^{13}/C^{12} ratio**
L17Q	1637.5	1	1597.3	0.88	1.13
V18Q	1632.7	1	1604.7	0.93	1.07
F20Q	1633.3	1	1601.8	1.3	0.77
A21Q	1631.3	1	1606.1	1.2	0.83
E22Q	1634.3	1	1601.4	0.79	1.26

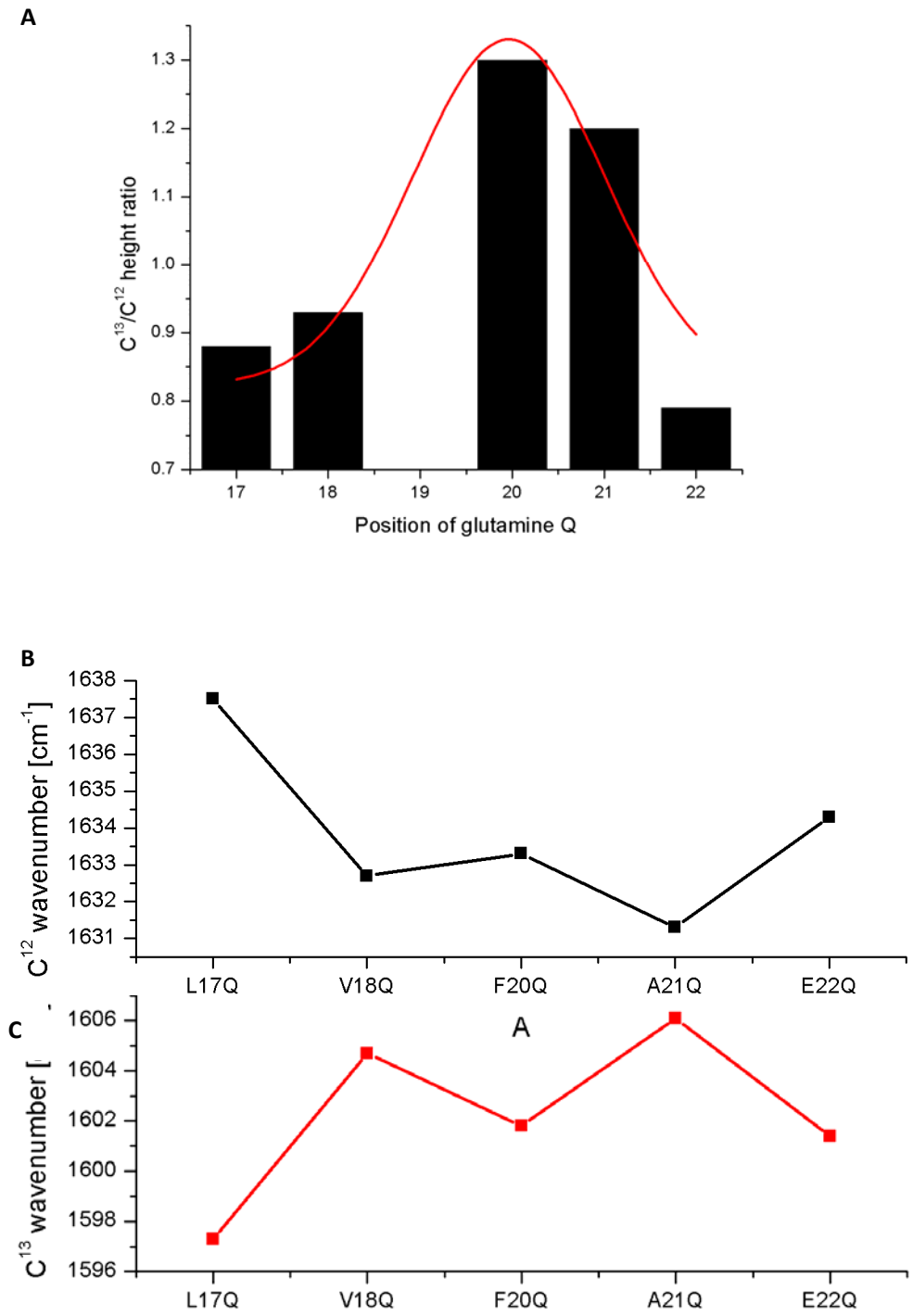

Figure 5-7. Patterns of C^{13} and C^{12} peaks' trend against amino acid enrichment .
(**A**) The ratio of C^{13}/C^{12} increases as Q is moved to the center of the peptide.
(**B**) The positions of C^{13} and C^{12} peaks as a function of Q mutation.
(**C**)The trend of C^{12} shift is the opposite of the ones of C^{13} band.

From **figure 5-7 A**, the C^{13}/C^{12} peak ratio exhibited a pattern of normal distribution. The closer

glutamine is to the center of the peptide, the higher C^{13}/C^{12} ration is. This pattern could be explained by Q track limiting the molecular movement around isotope enriched residue. The decreased movement of ^{13}C enriched carbonyl results in a higher intensity of the ^{13}C band.

Interestingly, as amino acids at different positions are mutated to glutamine, an alternative pattern of ^{12}C and ^{13}C wavenumber appears, and the change of ^{12}C mirrors the one of ^{13}C. It is still unclear how this pattern could appear if all mutants form parallel β-sheets. Additionally, mutations that drive red shift of ^{12}C seems to simultaneously drive the blue shift of ^{13}C peak. This seems to correspond to Q's position above and below the β-sheet plane. Therefore, future studies should be focused on laminations. Cryo-EM and X-ray diffraction and simulations between laminations could be conducted in the future to obtain the optimal stacking pattern[10-12].

Conclusion

In this chapter, the impact of glutamine's position on Aβ (16-22) was studied. As reflected by the by morphology from TEM and kinetic study using IE-IR, glutamine position swapping reveals the importance of the position of key amino acids at a certain peptide. This demonstrates key constraints' global impacts on corporative assemblies.[13]. In the grand picture, it sheds light on why a single amino acid mutant like Dutch mutant could trigger cerebral hemorrhages and premature death.[14]

This study could also reveal another potential applications for IR. So far, IE-IR method has been utilized to study the secondary structure of amyloid self-assembly and its utilization in E22Q structural transition has been explained in previous chapters. The IE-IR spectra are defined by peptide secondary structure and the position of isotope label. However, the result from this chapter raises a question: since all the mutants are parallel and the isotope is labeled at the same position, why would IE-IR differ drastically? The only rational answer is the higher-order difference of these mutants is impacting the IR spectra. Currently, no study has reported the difference in IE-IR signal above secondary structure. The dramatic difference in IE-IR signal reported in this chapter reveals its potential to be highly sensitive to subtle structural differences. Different mechanisms could be at play: the Q track serves as the stapler that restrains freedom of molecular movement and determines the broadness of peaks; the differences on fiber twisting determines the angle of coupling which is magnified over long range order, the lateral association of proto-fibers limits the water contents, movement and frequency of ^{12}C vibration as a whole, therefore shifting its frequency.

References

(1) Gessel, M. M.; Bernstein, S.; Kemper, M.; Teplow, D. B.; Bowers, M. T. Familial Alzheimer's disease mutations differentially alter amyloid beta-protein oligomerization. *ACS Chem Neurosci* **2012**, *3*, 909-918.

(2) Van Nostrand, W. E.; Melchor, J. P.; Cho, H. S.; Greenberg, S. M.; Rebeck, G. W. Pathogenic effects of D23N Iowa mutant amyloid beta -protein. *J Biol Chem* **2001**, *276*, 32860-

32866.

(3) Melchor, J. P.; McVoy, L.; Van Nostrand, W. E. Charge alterations of E22 enhance the pathogenic properties of the amyloid beta-protein. *J Neurochem* **2000**, *74*, 2209-2212.

(4) Kamp, J. A.; Moursel, L. G.; Haan, J.; Terwindt, G. M.; Lesnik Oberstein, S. A.; van Duinen, S. G.; van Roon-Mom, W. M. Amyloid beta in hereditary cerebral hemorrhage with amyloidosis-Dutch type. *Rev Neurosci* **2014**, *25*, 641-651.

(5) Baumketner, A.; Bernstein, S. L.; Wyttenbach, T.; Lazo, N. D.; Teplow, D. B.; Bowers, M. T.; Shea, J. E. Structure of the 21-30 fragment of amyloid beta-protein. *Protein Sci* **2006**, *15*, 1239-1247.

(6) Sian, A. K.; Frears, E. R.; El-Agnaf, O. M.; Patel, B. P.; Manca, M. F.; Siligardi, G.; Hussain, R.; Austen, B. M. Oligomerization of beta-amyloid of the Alzheimer's and the Dutch-cerebral-haemorrhage types. *Biochem J* **2000**, *349*, 299-308.

(7) Marchesan, S.; Vargiu, A. V.; Styan, K. E. The Phe-Phe Motif for Peptide Self-Assembly in Nanomedicine. *Molecules* **2015**, *20*, 19775-19788.

(8) Bertolani, A.; Pirrie, L.; Stefan, L.; Houbenov, N.; Haataja, J. S.; Catalano, L.; Terraneo, G.; Giancane, G.; Valli, L.; Milani, R.; Ikkala, O.; Resnati, G.; Metrangolo, P. Supramolecular amplification of amyloid self-assembly by iodination. *Nat Commun* **2015**, *6*, 7574.

(9) de Groot, N. S.; Parella, T.; Aviles, F. X.; Vendrell, J.; Ventura, S. Ile-phe dipeptide self-assembly: clues to amyloid formation. *Biophys J* **2007**, *92*, 1732-1741.

(10) Schmidt, A.; Annamalai, K.; Schmidt, M.; Grigorieff, N.; Fandrich, M. Cryo-EM reveals the steric zipper structure of a light chain-derived amyloid fibril. *Proc Natl Acad Sci U*

S A **2016**, *113*, 6200-6205.

(11) Sawaya, M. R.; Sambashivan, S.; Nelson, R.; Ivanova, M. I.; Sievers, S. A.; Apostol, M. I.; Thompson, M. J.; Balbirnie, M.; Wiltzius, J. J.; McFarlane, H. T.; Madsen, A. O.; Riekel, C.; Eisenberg, D. Atomic structures of amyloid cross-beta spines reveal varied steric zippers. *Nature* **2007**, *447*, 453-457.

(12) Langkilde, A. E.; Morris, K. L.; Serpell, L. C.; Svergun, D. I.; Vestergaard, B. The architecture of amyloid-like peptide fibrils revealed by X-ray scattering, diffraction and electron microscopy. *Acta Crystallogr D Biol Crystallogr* **2015**, *71*, 882-895.

(13) Childers, W. S., Mehta, A.K., Bui, T.Q., Liang, Y. and Lynn, D.G. Toward intelligent materials. *Molecular Self-Assembly: Advances and Applications* **2012**, 1.

(14) Davis, J.; Xu, F.; Deane, R.; Romanov, G.; Previti, M. L.; Zeigler, K.; Zlokovic, B. V.; Van Nostrand, W. E. Early-onset and robust cerebral microvascular accumulation of amyloid beta-protein in transgenic mice expressing low levels of a vasculotropic Dutch/Iowa mutant form of amyloid beta-protein precursor. *J Biol Chem* **2004**, *279*, 20296-20306.

Chapter 6 IE-IR of parallel peptide system

Background

IE-IR is a simple and efficient method to monitor kinetic transition of peptide conformation [1,2] and confirming the orientation of β-sheets[3]. Multiple computational simulation works have been dedicated to predict the infrared spectra of parallel β-sheet. Simulation is normally conducted by *ab* initio density functional theory (DFT) calculation[4] combined with molecular dynamics (MD) simulation. These simulations commonly convert all side chains to alanine.[3]Current simulation mostly focuses on examine the impact of carbonyl alignment on IE-IR spectra. This localized model emphasis the immediate chemical environment of the ^{13}C labeled amino acid. As a result, most studies predict the IE-IR spectrum of parallel β-sheet should not vary with the position of the label. For example, the work by Axelsen group [4] predicted the infrared spectrum of parallel β-sheet does not change with the position of labels along peptide WLLLLL[4] (**Figure 6-1**). Based on this, experimental methods of using IE-IR to differentiate between parallel and anti-parallel peptide structure has been widely adopted. The commonly adopted method is to enrich different amino acids on the same peptide and compare resulting spectra (isotope scanning experiment). Overlapped spectrum would indicate parallel.[5] Interestingly, to my knowledge no research using this method has observed identical spectra with isotope scanning and all β-sheets studied were concluded to be anti-parallel.

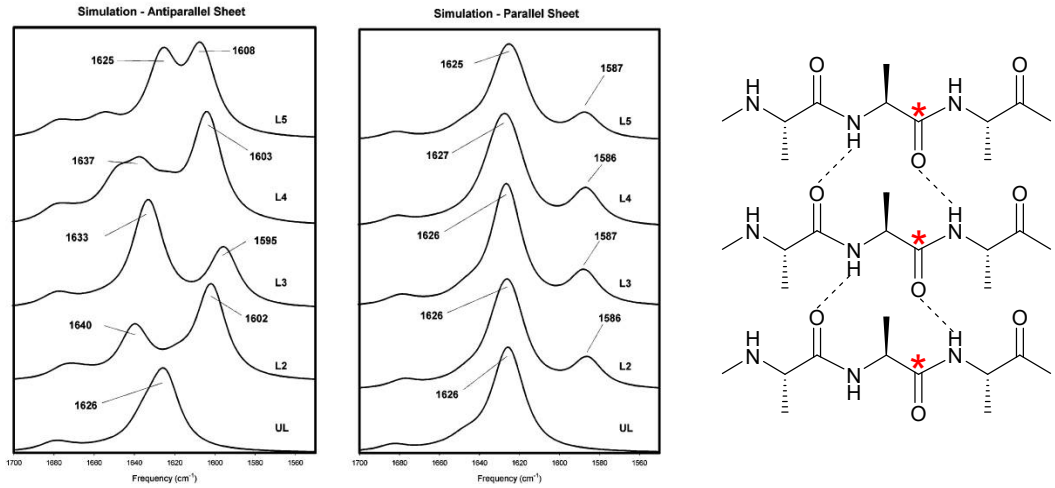

Figure 6-1. Prediction of the IE-IR spectrum of WLLLLL in anti-parallel (left) and parallel (right) conformation.

However, other theories have been developed such as the one by Strasfeld et.al. Through 2D-IR simulation, they predicted the 2D IR spectra rely heavily on the position of the isotopelabeled residue by looking at the cross-peak of $^{12}C{=}O^{16}$ and $^{13}C{=}O^{18}$. [6]

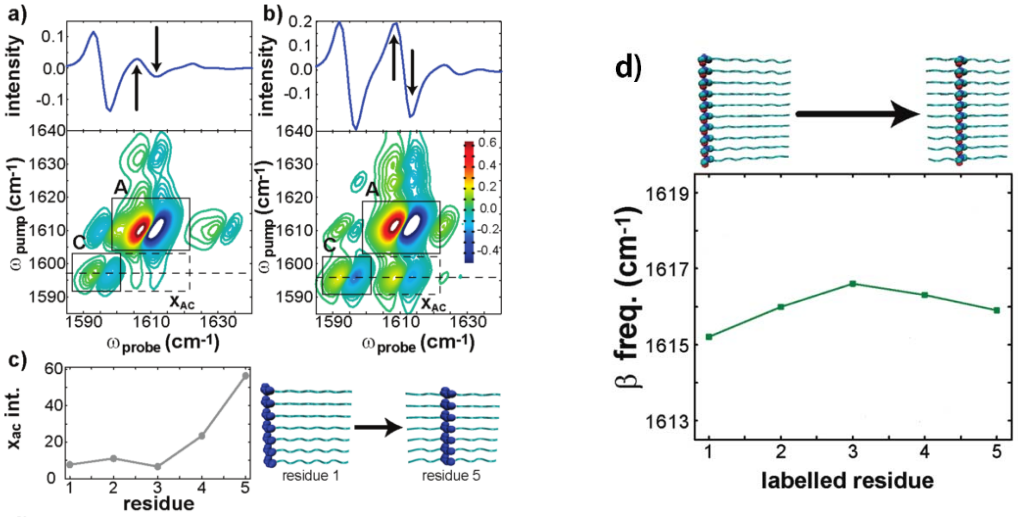

Figure 6-2. Simulated 2D-IR spectrum of 9 residue peptide that forms a β-sheet with the isotope enrichment at different positions.

(a) The cross-peak is the weakest when the isotope is placed at the end of the peptide

(b) The cross-peak is the highest when the isotope is placed at the center of the peptide

(c) The intensity of cross peak as a function of isotope enriched residue

(d) The frequency of ^{12}C band as a function of isotope enriched residue

In the study, the impact of isotope position on 2D-IR spectra was investigated. The introduction of $^{13}C=O^{18}$ caused dramatic energy shift of the enriched carbonyl and decreases the wavenumber by 64 cm^{-1}.[7] Despite the large shift, 2D-IR spectra can still exhibit cross-peaks between enriched and unenriched residues. The cross peak is shown as X_{AC} and its intensity is highest when placed at the center of the peptide. This is explained by the vicinity of enriched amino acid and the central unenriched residue.[6]

Additionally, due to the presence of isotope enriched peptide, the peak position of ^{12}C changes and is more blue-shifted when the enriched residue is in the middle of the peptide (**Figure 6-2 d**). Strasfeld et.al contributed that to the interruption of lateral coupling of natural abundance ^{12}C carbonyl by enriched amino acid. When the isotope edited residue is in the middle, there are two shorter natural peptides, (in the case of peptide of 9 amino acids, there are two resulting tetramers), and that will cause a blue-shift of the IR spectrum. Conversely, when the isotope enriched residue is near the end, a longer natural abundance peptide is present, the peak position is more red-shifted compared to when the enriched residue is in the middle. This study predicts a strong correlation between isotope position and the resulting 2D-IR spectra. Additionally, the vibrational coupling between ^{13}C and ^{12}C through 2D-IR with synthetic peptide macrocycle that was designed to be parallel was experimentally studied, revealing both inter and intra-strand coupling influences the IE-IR spectrum of isotope edited β-sheet.Aside from shifting frequency by through bond coupling and hydrogen bonding network, through space coupling also significantly impacts IR. [8]

These studies indicate that the commonly acknowledged model for predicting the IE-IR signal of β-sheet might be too simplified. Other parameters, such as the position of enrichment [6], the through space coupling between neighboring amino acids[8] need to be considered. However, no experimental studies have been conducted due to the lack of extended parallel β-sheet system.

While most short peptides form anti-parallel sheets,[9-12]we have exploited the cross-strand potential of glutamine residues to enforce parallel strand arrangements through extended Q-tracks[13,14]. This assembly allowed us to map the effect of incorporating single ^{13}C enrichments along the entire length of peptide Aβ(16-22)E22Q or Ac-KLVFFAQ-NH_2 (or simply E22Q) and observe the effect of isotope position on IE-IR spectra.

Methods

Fibril Assembly: Lyophilized Peptides were dissolved in 1,1,1,3,3,3-hexafluoro-2-propanol (HFIP, Sigma) and sonicated for 30 min, then dried under a stream of dry N_2 gas or under vacuum. The resultant clear film was dissolved in 20% acetonitrile/water (0.1 vol% TFA), bath sonicated for at least 10 min and, unless indicated, incubated at room temperature for assembly. To produce unassembled peptide, lyophilized peptide was dissolved in 1,1,1,3,3,3-hexafluoro-2-propanol (HFIP, Sigma) and sonicated for 30 min and stored at room temperature in HFIP.

Attenuated Total Reflectance Fourier Transform Infrared (AT-FTIR): Aliquots (10μL) of peptide solution were dried as thin films on an Pike GaldiATR (Madison, WI, USA) ATR diamond crystal. FT-IR spectra were acquired using a Jasco FT-IR 4100 (Easton, MD, USA) at room temperature and averaging 500 to 800 scans with 2 cm-1 resolution, using either an MCT or TGS detector, 5mm aperture and a scanning speed of 4mm/sec. Spectra were processed with zero-filling and a cosine apodization function. IE-IR spectra were normalized to the peak height of the 12C band.

Transmission Electron Microscopy (TEM): A TEM copper grid with a 200 mesh carbon support (Electron Microscopy Sciences) was covered with 10 μL of a diluted peptide solution (0.05 mM to 0.1 mM) for 1 min before wicking the excess solution with filter paper. 10 μL of the staining solution, either (2% uranyl acetate, Sigma-Aldrich, for Figure 2 of main text or methylamine tungstate, (Ted Pella, Inc) was added and incubated for 2 min, excess solution was wicked away, and the grids were placed in desiccators to dry under vacuum overnight.

Results

Scheme design

To test the positional dependence of IE-IR signal on the position of labeled amino acid, I synthesized Aβ（16-22）E22Q or Ac-^{16}KLVFFAQ^{22}-NH_2 with [1-^{13}C] isotope enriched on five residues—L17, V18, F19, F20, A21. These peptides are separately synthesized, purified,

assembled into 20% MeCN/H2O with 0.1% TFA, and incubated until the transition was complete. Later, the IE-IR of parallel E22Qs with different labels was measured.

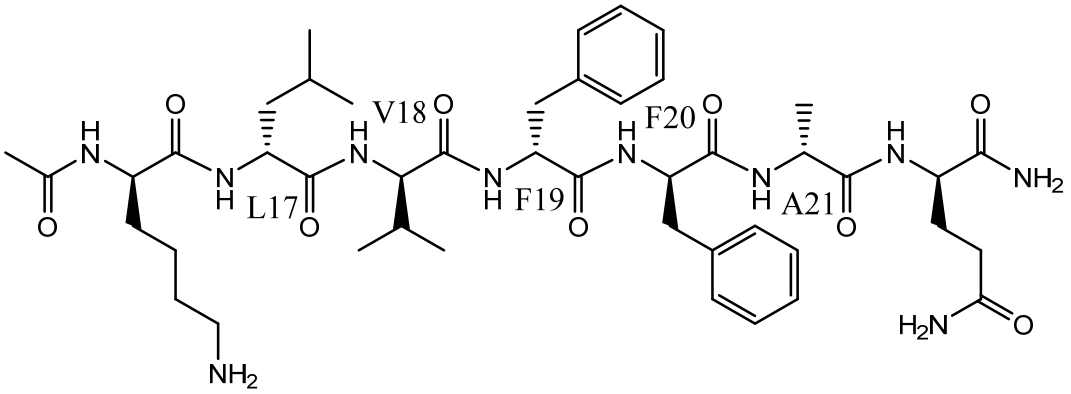

Figure 6-3. Chemical structure of Ac-^{16}KLVFFAQ^{22}-NH_2 with isotope enriched on different positions.

Isotope enrichment does not interfere with the structure

Isotope enrichment do not interfere with the conformation of peptides, therefore the structure of samples with different isotope enrichment are the same, as confirmed by the TEM result in **Figure 6-4**.

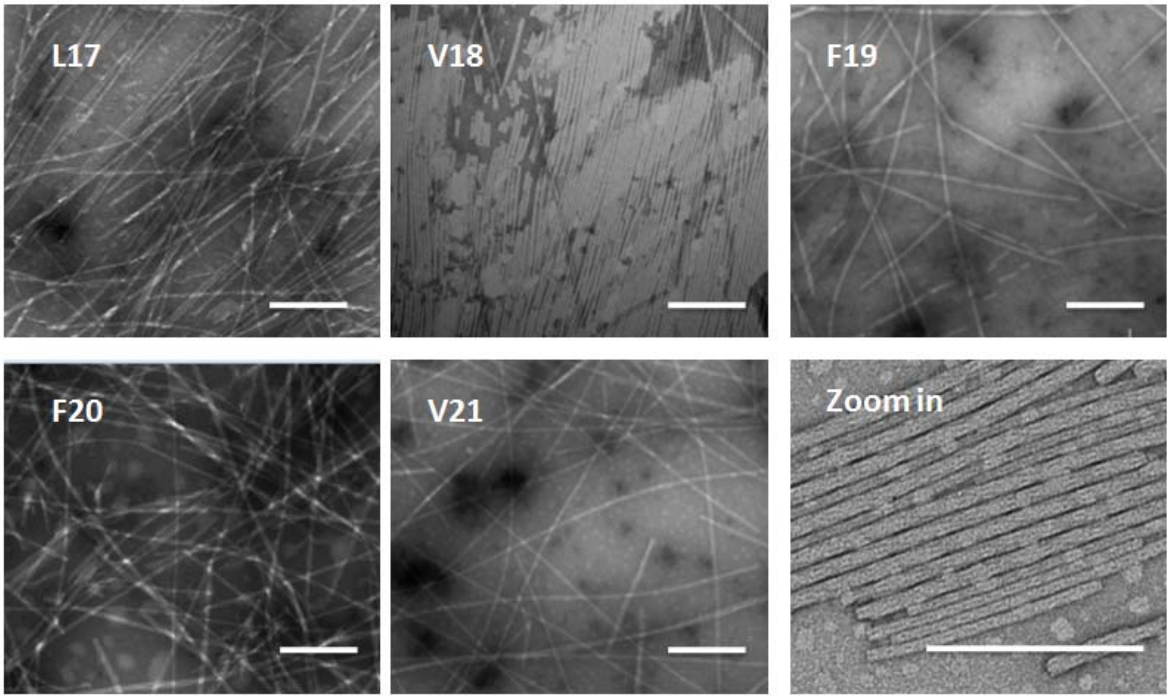

Figure 6-4. TEM of Aβ (16-22)E22Q with isotope enrichment at different residues. All samples grow into non-twisted fibers with width around 10±1 nm. Scale bar 200nm.

IE-IR spectra of isotope enrichment at different positions

Surprisingly, the IE-IR spectrum of Ac-^{16}KLVFFAQ^{22}-NH_2 varies dramatically depending on the enrichment position. The differences can be observed through the peak position of ^{12}C and ^{13}C peaks and the relative^{12}C/^{13}C height ratio. The variation among ^{13}C is 2-3 times more prominent than ^{12}C.

For ease of comparison, all spectra are normalized in two ways, one to the ^{12}C band at around 1630cm^{-1} so that it is easier to compare ^{13}C and ^{12}C bands, another is normalized to amide A to reveal actual height of amide I bands. [15]All spectra exhibit a 1676.3cm^{-1} band, which result from the Q-tracks and further supports all samples are parallel. The positional difference

between [1-^{13}C]F19 E22Q and [1-^{13}C]F20 E22Q, both enriched at vicinal phenylalanine, have the two stretching modes commonly assigned to ^{12}C=O and ^{13}C=O amide I bands; however, the F20 ^{12}C and ^{13}C bands are both red-shifted relative to F19, and the ^{12}C/^{13}C band intensity ratio for F20 is greater. The [1-^{13}C]F19 E22Q and [1-^{13}C]F20 E22Q are both in the middle of the strand where the conformation is more rigid and less exposed to solvent, yet their IE-IR spectra are strikingly different. Therefore, these features are not likely to be a simple function of side chain functionality or environment.

More dramatically, the spectra of [1-^{13}C]L17 E22Q and [1-^{13}C]V18 E22Q contain three bands each, with [1-^{13}C]L17 E22Q at 1628cm^{-1}, 1616 cm^{-1}, and 1597 cm^{-1} and [1-^{13}C]V18 E22Q's at 1633cm^{-1}, 1616cm^{-1}, and 1595.8cm^{-1}. This result is inconsistent with the traditional assignment of two bands, one for ^{12}C=O vibration and the other for ^{13}C=O, suggesting such an assignment is an over-simplification and other factors are contributing to IR bands. [1-^{13}C]A21 E22Q appears to have two broad bands. However, the one around 1611cm^{-1} is broad and is higher in intensity. It is unlikely a single ^{13}C enrichment would exhibit such high intensity therefore it is probably an overlap of two bands with lower frequency.

Normalization on amide A has the same effect as normalization against peptide concentration as it is least disturbed by peptide conformation.[15] The Thomas-Reiche-Kuhn sum rule or energy-weighted sum rule [16]dictates that the total area under the curve for amide I vibration remains constant regardless whether isotope enrichment exist or its position. From figure 6-4 bottom, the height of samples with 3 bands are lower than ones with 2 bands. This is consistent

with the sum rule and further substantiates the difference in spectra are inherent.

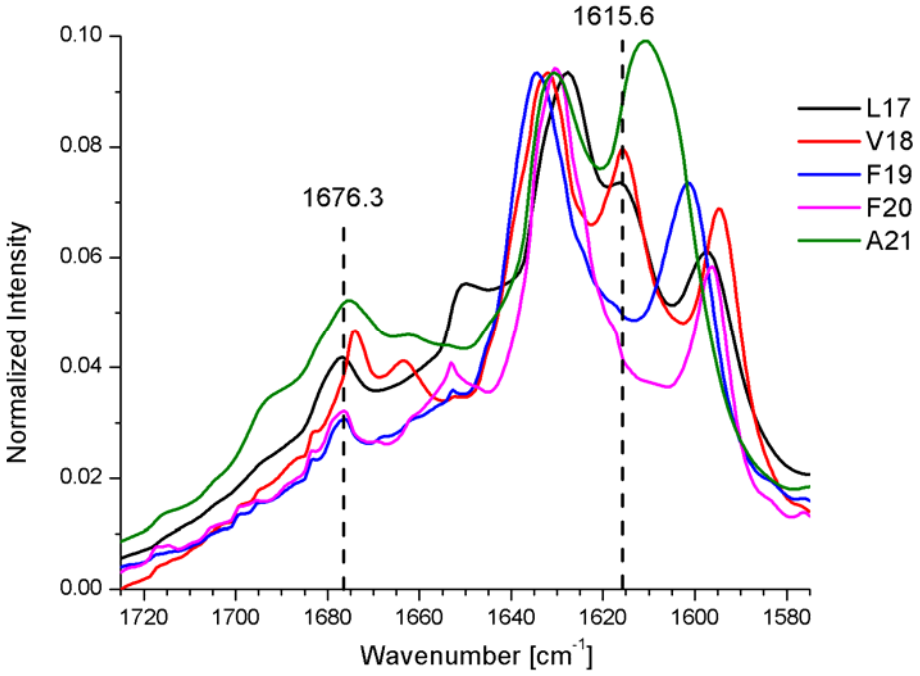

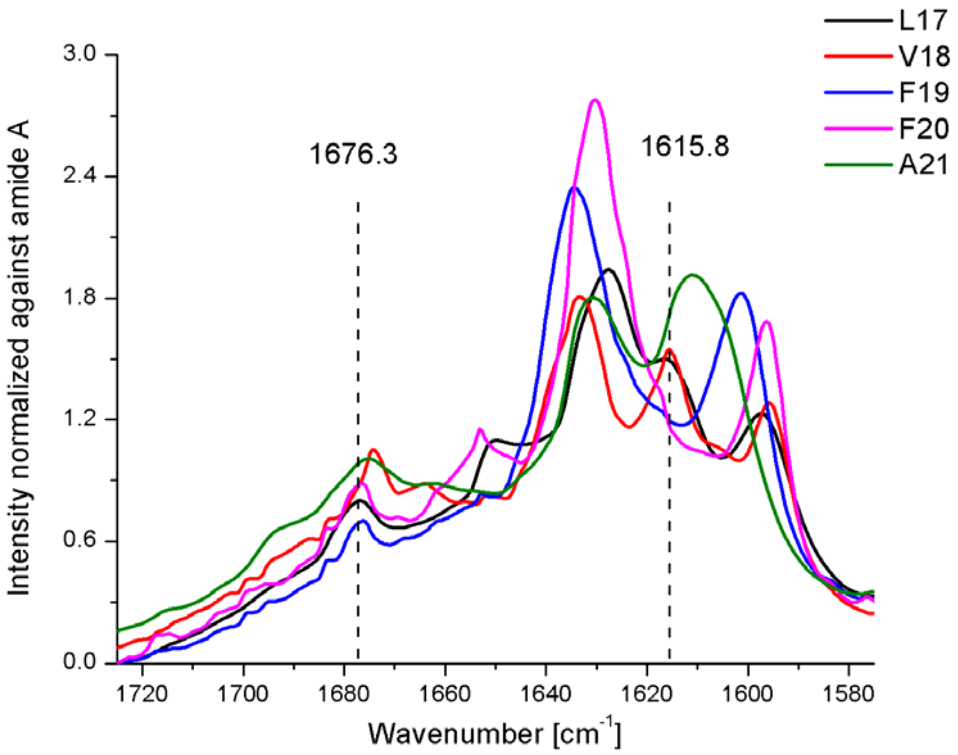

Figure 6-5. The IE-IR spectra as a function of isotope enrichment. The top graph is normalized against ^{12}C band; the bottom graph is normalized against amide A.

Elimination of artificial factors contributing to the spectral difference

With the robust reproducibility of the spectrum of [1-^{13}C] F19 Ac-KLVFFAQ-NH_2 from previous chapters, it is easy to eliminate the argument that any significant difference of the spectrum can be introduced by artificial factors (sample preparation, residual water in the dry film ATR, etc.) To further confirm such a difference is an inherent nature, reproduction experiments are conducted on [1-^{13}C]F20 E22Q by different students.

Table 6-1. Experimental conditions for reproducibility test of [1-^{13}C]F20 Aβ(16-22) E22Q

	Synthetic method	**IR spectra**
Student 1	Manual synthesis	Lyophilized powder was pressed onto ATR
Student 2	Automatic synthesizer	10μL of sample was blow dried on ATR

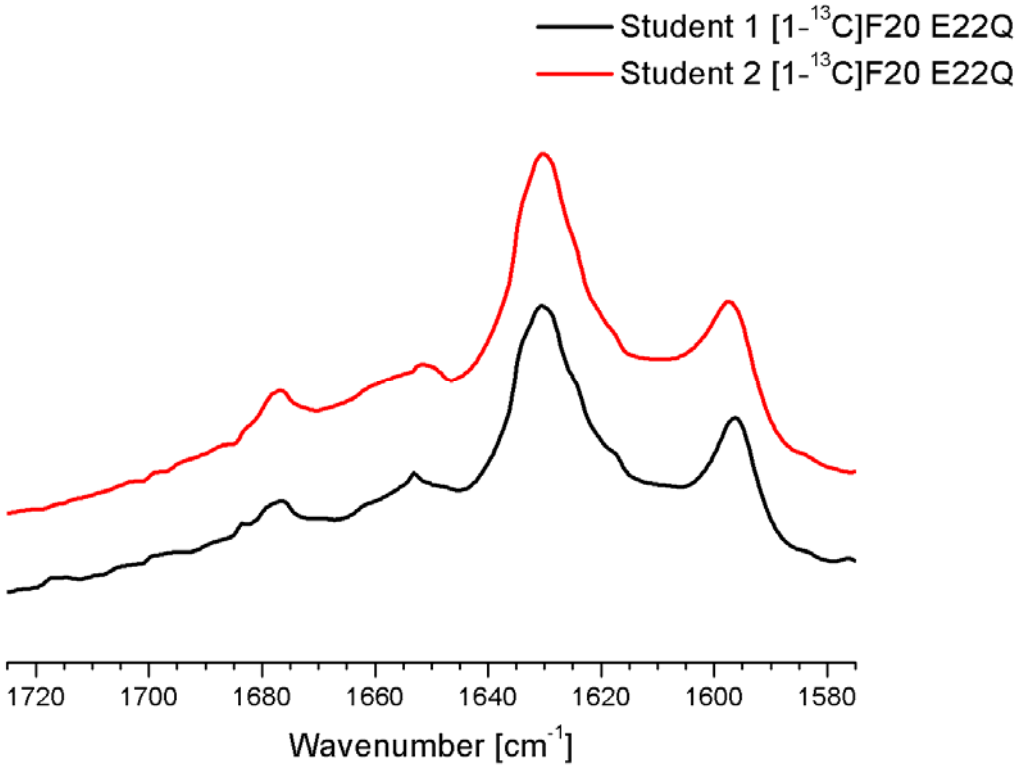

Figure 6-6. IE-IR spectra of [1-^{13}C] F20 E22Q synthesized via different students

Elimination of artificial factors introduced by preparation procedure

To eliminate artificial factors from sample preparation, including HFIP treatment and seeding, the same batch of peptide [1-^{13}C]L17 Aβ(16-22)E22Q was assembled through different protocols.

Table 6-2. Experimental conditions for reproducibility test of [1-^{13}C]L17 Aβ(16-22) E22Q

	HFIP treatment	**Seeding from mature fibers**
Protocol 1	Sample was directly dissolved with 20% MeCN/H2O with 0.1% TFA	No
Protocol 2	Peptide was first dissolved in HFIP; HFIP was later evaporated and the sample was re-dissolved with 20% MeCN/H2O with 0.1% TFA	1% seeds

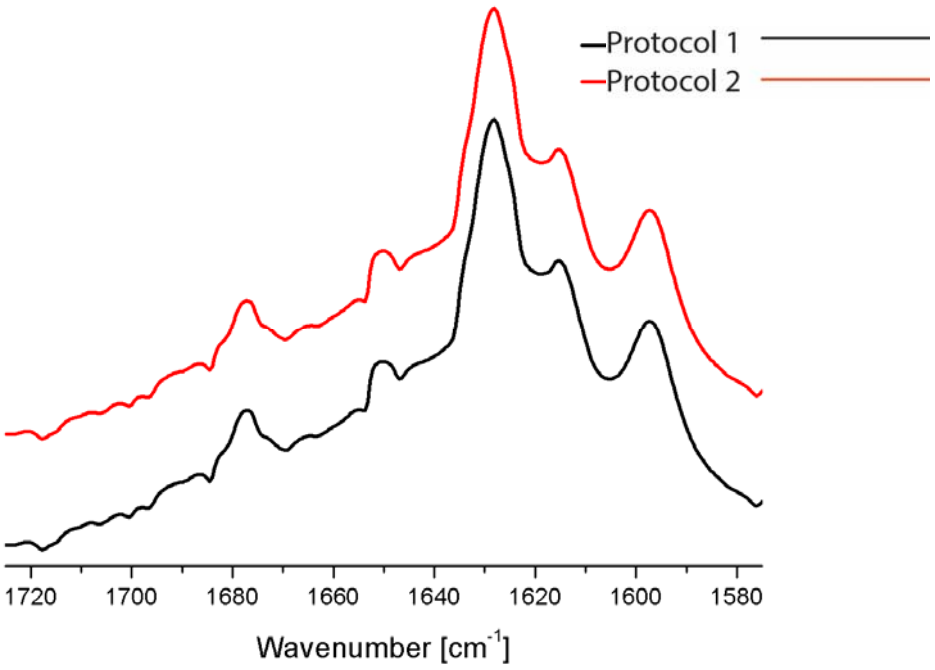

Figure 6-7. IE-IR of [1-^{13}C] F19 E22Q assembled under different methods

These results confirmed that such a drastic difference of IE-IR signal comes completely from the labeling itself instead of haphazard factors.

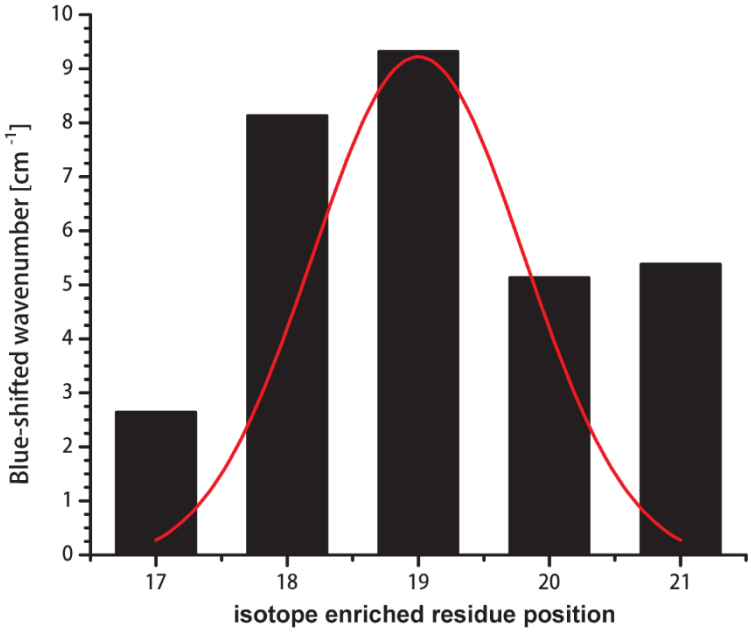

Figure 6-8. Wavenumber of ^{12}C band as a function of labeled amino acid
X-axis indicates the position of isotope enrichment; the y-axis indicates the degree of blue-shift of the ^{12}C band compared to unenriched peptide.

The shift of ^{12}C peak has a trend consistent with the computational prediction of Strasfeld [6].

When enriched reside is at the middle of the peptide, ^{12}C peak blue-shifts the most. (**Figure 6-8**)

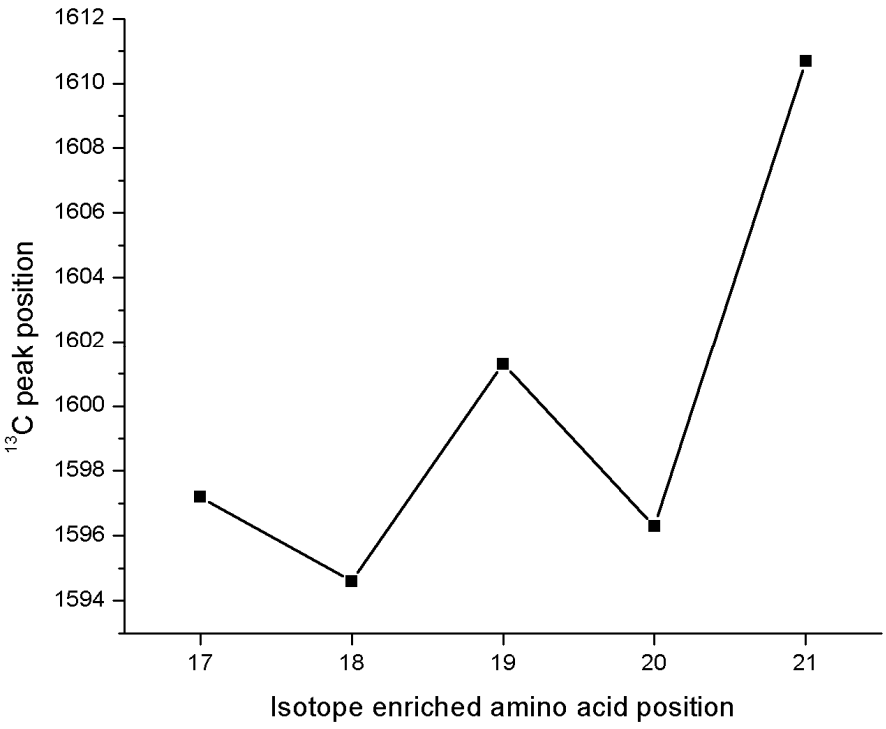

Figure 6-9. Wavenumber of ^{13}C band as a function of the labeled amino acid.

Meanwhile, the position of ^{13}C peak is also plotted against the position of labeled amino acid. (**Figure 6-9**). (In case of spectrum with three peaks, the peak with the lowest wavenumber is used as ^{13}C). Based on the result, when the enrichment site is moved from the N terminus to C terminus, the position of ^{13}C peak fluctuates over a range of twenty wavenumbers. It is worthwhile to notice that when Q is on 18th and 20th position, the ^{13}C wavenumber decreases while on the opposite phase the wavenumber increases. This may be explained by the polarity of amyloid fibers as the chemical environment on different phase of the β-sheets are different .[17,18]

Another trend is the general increase of ^{13}C peak wavenumber as the label is positioned from

the N terminus to the C terminus. This trend is in line with the trend of ^{13}C when E22Q is changing from anti-parallel to parallel as the ^{13}C peak shifts from 1596cm^{-1} to 1602cm^{-1}. In both cases, the alignment of ^{13}C is increased, either by limit of movement by Q-track or peptide orientation, yet it is unclear why the ^{13}C band blue shifts rather than red shifts, since alignment should delocalize the vibrations and leads to a red-shift, which happened for ^{12}C band and for ^{13}C band in titration experimetns.[6] This result is also in contrast with what Decatur reported for prion peptide H1 , in which the alignment of ^{13}C carbonyls creates a red shift. [1] This paradox might result from the impact of vibrational coupling between ^{12}C and ^{13}C, which significantly impacts the wavenumber and height of both bands.

Dilution experiment

To test whether the position of peak could be influenced by ^{12}C-^{13}C coupling, dilution experiment was conducted. [1-^{13}C] F19 E22Q and un-enriched E22Q were dissolved in HFIP separately. [1-^{13}C] F19 E22Q was titrated into un-enriched peptide with a percentage of 20%, 40%, 60%, 80% at a total concentration of 1mM.

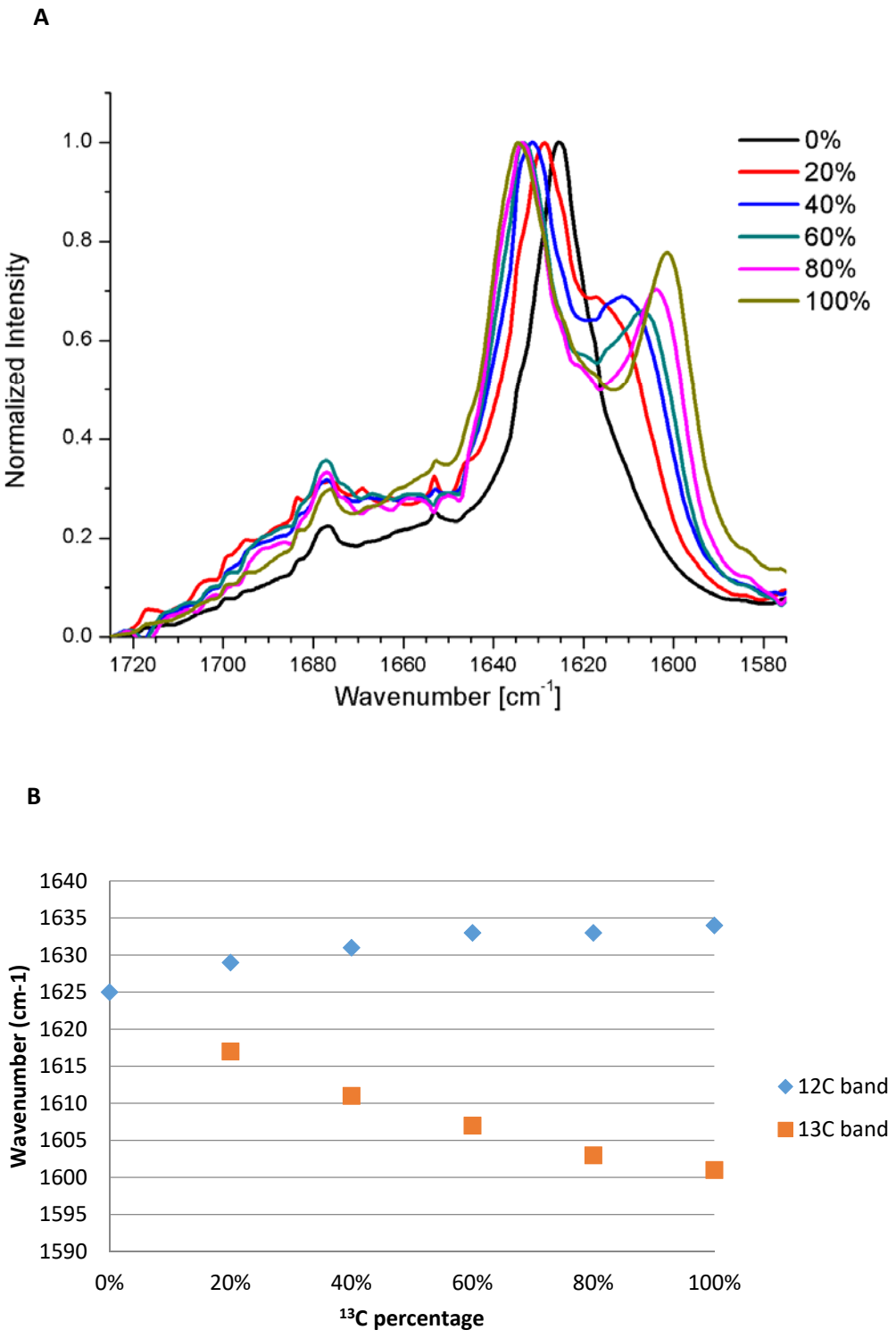

Figure 6-10. (**A**) Isotope titration of [1-^{13}C] F19 E22Q at different percentage of isotope labeled peptide. (**B**)The trend of ^{12}C and ^{13}C band with different percentage of isotope enriched peptide.

As seen from the data, as ^{13}C enrichment increases, delocalization of the ^{12}C band is reduced and the transition is blue shifted. In contrast, increasing the ^{13}C percentage red shifts its transition and increases the $^{13}C/^{12}C$ intensity ratio. ^{13}C band is more sensitive to isotope titration: a 20% adjustment in isotope abundance generates a change of $4cm^{-1}$ for ^{13}C band and 2 cm^{-1} for ^{12}C band.

Based on how C^{12} and C^{13} carbonyl originated bands exhibit opposite trends with isotope titration, the origin of additional bands for [1-^{13}C] L17E22Q and [1-^{13}C] V18 E22Q was evaluated. The result for [1-^{13}C] V18 E22Q is shown in **figure 6-11**.

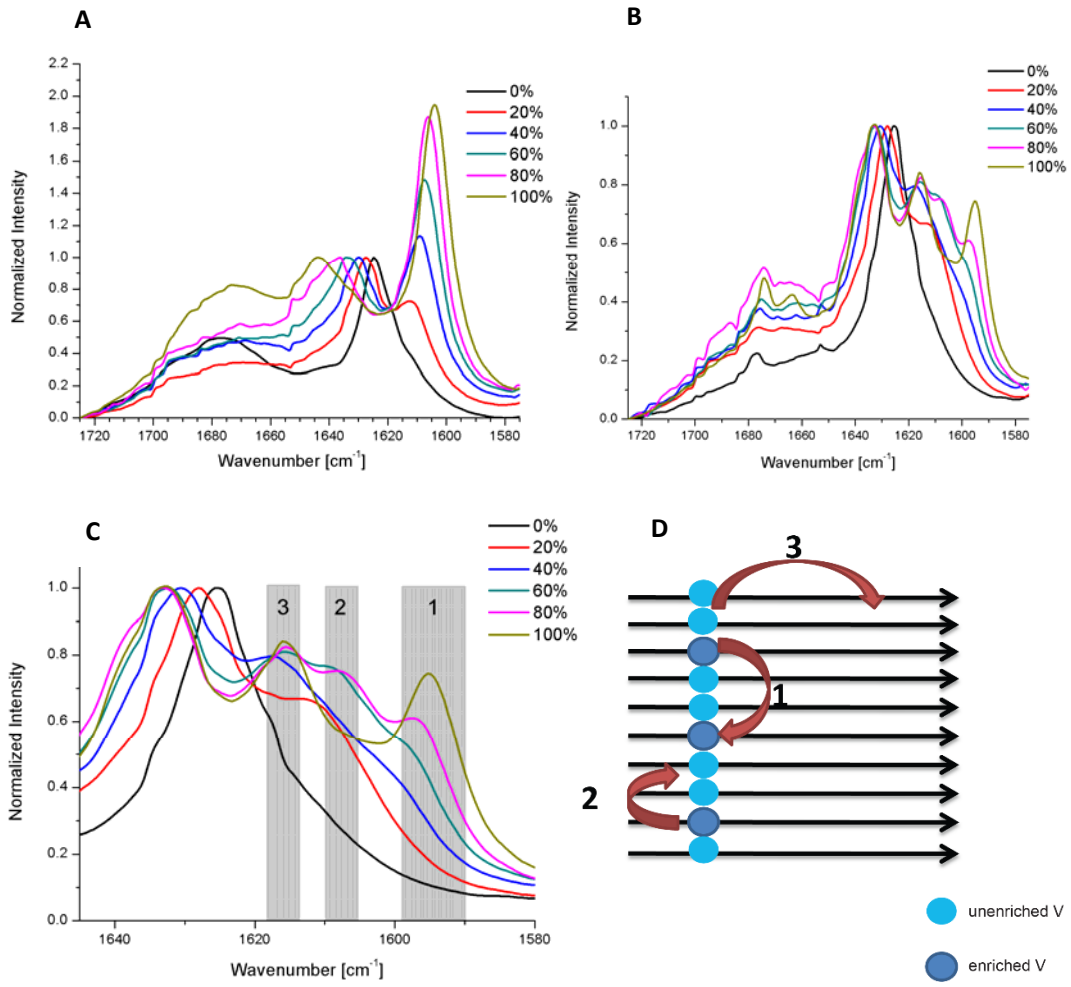

Figure 6-11. IE-IR spectra of [1-^{13}C]V18 E22Q titration experiment at (**A**) the beginning and (**B**) end of the assembly. (**C**) The ^{13}C band region is expanded with peaks numbered. (**D**)Peak assignments.

From **figure 6-11**. At the beginning of assembly, E22Q was anti-parallel out-of-register. The isotope titration leads to a significant blue shift of ^{12}C peak from 1624.5cm^{-1} at natural abundance to 1643.9 cm^{-1} at 100% ^{13}C; the relative intensity of ^{12}C and ^{13}C shifts from 1.4 at 20% ^{13}C to 0.51 at 100% ^{13}C enrichment.

The end spectra elucidates the origin of various peaks. Isotopic dilution reveals an additional band (Band 2) for 60% and 80% ^{13}C which later disappears at 100% ^{13}C enrichment. The trend for bands around 1630cm^{-1} are assigned as ^{12}C-^{12}C modes from the blue shift and decreased intensity with increasing ^{13}C, and the remaining bands are assigned to be relevant to ^{13}C. Band 1 red shifts and increases significantly with increase of ^{13}C and therefore represents interstrand ^{13}C carbonyl coupling. Band 2 is not resolved with 20% and 40% enrichment, red shifts from 60% to 80%, and is not resolved with 100% ^{12}C enrichment. This result is most consistent with band 2 originating from ^{12}C=O and ^{13}C=O coupling of neighboring strands.

Band 3 also red shifts but its relative intensity does not change significantly with ^{13}C enrichment, and the interaction likely arises from ^{12}C=O and ^{13}C=O general coupling. The data suggests that the energy between ^{12}C/^{12}C and ^{13}C/^{13}C coupling is close enough to have additional coupling and generates additional bands, which can be resolved on IR spectra. Its worth noting that in Strasfeld's simulation of the cross-peak between enriched and unenriched vibrators, ^{13}C=^{18}O were used, while for 1D IR, the shift of enriched carbonyl is far less therefore the interaction between ^{13}C=O and ^{12}C=O could be stronger, thus generating a larger influence.

Titration experiment for [1-^{13}C]L E22Q shows similar trend yet due to the higher wavenumber of band 1, band 2 does not manifest.

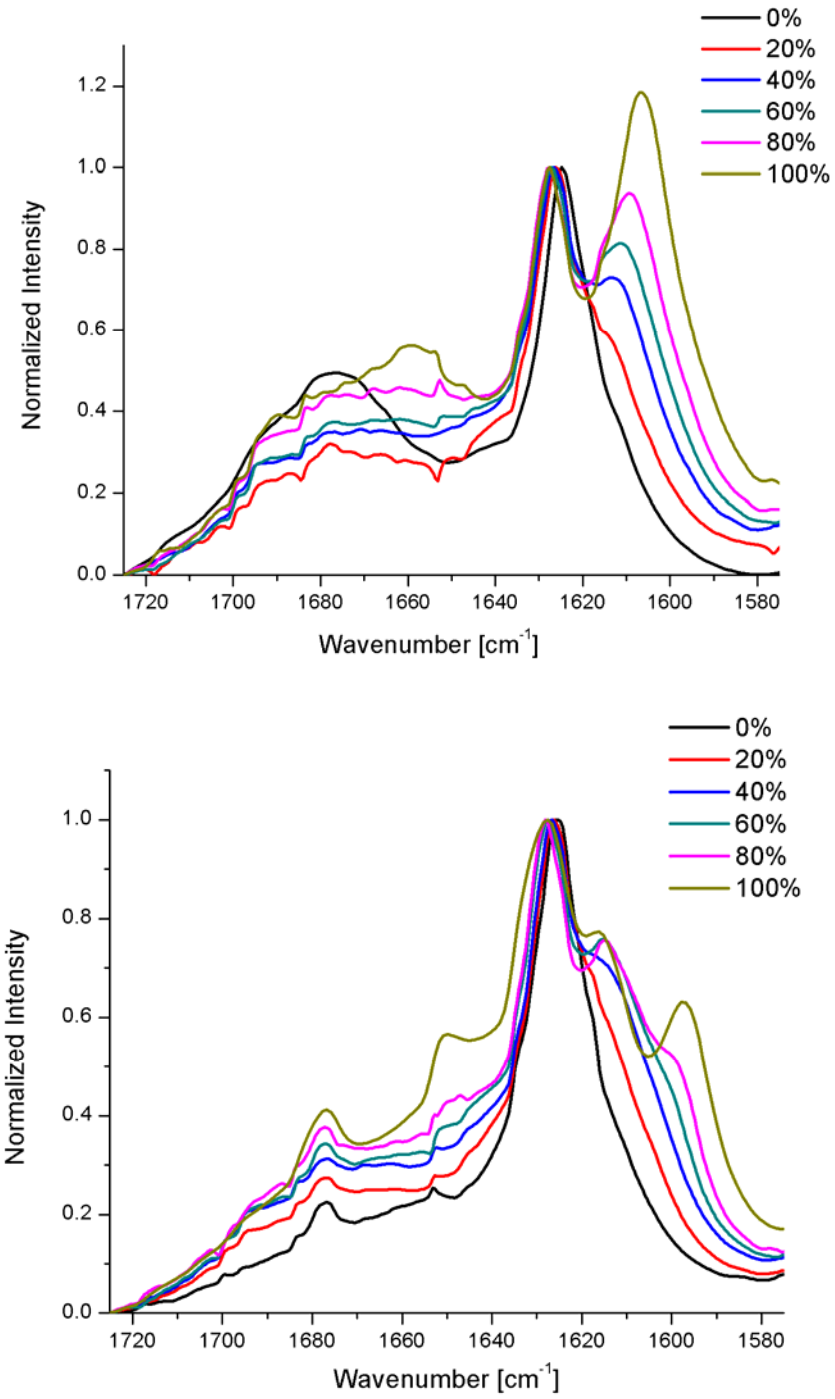

Figure 6-12.The IE-IR spectra of [1-^{13}C] L E22Q at the beginning (top) and end (bottom) of the assembly.

Conclusion

In this chapter, the positional dependence of IE-IR spectra on isotope enrichment is examined. In contrast with common beliefs, the IE-IR spectra shifts dramatically in terms of band numbers, heights and positions. Titration study reveals several factors are attributable to this differences, including the lateral coupling of ^{12}C carbonyls along peptide strand and the coupling between ^{12}C and ^{13}C carbonyls. My study promotes current understanding of IE-IR and enhances its applications for studying protein secondary structure and assembly dynamics.

References

(1) Petty, S. A.; Decatur, S. M. Intersheet rearrangement of polypeptides during nucleation of {beta}-sheet aggregates. *Proc Natl Acad Sci U S A* **2005**, *102*, 14272-14277.

(2) Silva, R. A.; Barber-Armstrong, W.; Decatur, S. M. The organization and assembly of a beta-sheet formed by a prion peptide in solution: an isotope-edited FTIR study. *J Am Chem Soc* **2003**, *125*, 13674-13675.

(3) Welch, W. R.; Keiderling, T. A.; Kubelka, J. Structural analyses of experimental 13C edited amide I' IR and VCD for peptide beta-sheet aggregates and fibrils using DFT-based spectral simulations. *J Phys Chem B* **2013**, *117*, 10359-10369.

(4) Paul, C.; Wang, J.; Wimley, W. C.; Hochstrasser, R. M.; Axelsen, P. H. Vibrational coupling, isotopic editing, and beta-sheet structure in a membrane-bound polypeptide. *J Am Chem Soc* **2004**, *126*, 5843-5850.

(5) Chi, H.; Welch, W. R.; Kubelka, J.; Keiderling, T. A. Insight into the packing pattern

of beta2 fibrils: a model study of glutamic acid rich oligomers with 13C isotopic edited vibrational spectroscopy. *Biomacromolecules* **2013**, *14*, 3880-3891.

(6) Strasfeld, D. B.; Ling, Y. L.; Gupta, R.; Raleigh, D. P.; Zanni, M. T. Strategies for Extracting Structural Information from 2D IR Spectroscopy of Amyloid: Application to Islet Amyloid Polypeptide. *Journal of Physical Chemistry B* **2009**, *113*, 15679-15691.

(7) Moran, S. D.; Zanni, M. T. How to Get Insight into Amyloid Structure and Formation from Infrared Spectroscopy. *J Phys Chem Lett* **2014**, *5*, 1984-1993.

(8) Woys, A. M.; Almeida, A. M.; Wang, L.; Chiu, C. C.; McGovern, M.; de Pablo, J. J.; Skinner, J. L.; Gellman, S. H.; Zanni, M. T. Parallel beta-sheet vibrational couplings revealed by 2D IR spectroscopy of an isotopically labeled macrocycle: quantitative benchmark for the interpretation of amyloid and protein infrared spectra. *J Am Chem Soc* **2012**, *134*, 19118-19128.

(9) Klimov, D. K.; Thirumalai, D. Dissecting the assembly of A beta(16-22) amyloid peptides into antiparallel beta sheets. *Structure* **2003**, *11*, 295-307.

(10) Zanuy, D.; Ma, B.; Nussinov, R. Short peptide amyloid organization: stabilities and conformations of the islet amyloid peptide NFGAIL. *Biophys J* **2003**, *84*, 1884-1894.

(11) Zanuy, D.; Ma, B. Y.; Nussinov, R. Short peptide amyloid organization: Stabilities and conformations of the islet amyloid peptide NFGAIL. *Biophys J* **2003**, *84*, 1884-1894.

(12) Ma, B. Y.; Nussinov, R. Stabilities and conformations of Alzheimer's beta-amyloid peptide oligomers (A beta(16-22 ') A beta(16-35 ') and A beta(10-35)): Sequence effects. *P Natl Acad Sci USA* **2002**, *99*, 14126-14131.

(13) Liang, C. Characterizing Kinetic Intermediate in Amyloid Self-Assembly. *Biophys J* **2015**, *108*, 524a-524a.

(14) Smith, J. E.; Liang, C.; Tseng, M.; Li, N.; Li, S.; Mowles, A. K.; Mehta, A. K.; Lynn, D. G. Defining the Dynamic Conformational Networks of Cross- Peptide Assembly. *Isr J Chem* **2015**, *55*, 763-769.

(15) Barth, A. Infrared spectroscopy of proteins. *Biochim Biophys Acta* **2007**, *1767*, 1073-1101.

(16) Smith, W. L. Energy-weighted sum rules and the analysis of vibrational structure in molecular spectra. *J Mol Spectrosc* **2015**, *316*, 105-113.

(17) DePace, A. H.; Weissman, J. S. Origins and kinetic consequences of diversity in Sup35 yeast prion fibers. *Nat Struct Biol* **2002**, *9*, 389-396.

(18) Mehta, A. K.; Lu, K.; Childers, W. S.; Liang, Y.; Dublin, S. N.; Dong, J.; Snyder, J. P.; Pingali, S. V.; Thiyagarajan, P.; Lynn, D. G. Facial symmetry in protein self-assembly. *J Am Chem Soc* **2008**, *130*, 9829-9835.

Chapter 7. Conclusion and perspectives

The diagnosis and successful treatment of neurodegenerative diseases many depend on a thorough understanding of the structure and dynamics of amyloid self-assembly. The complexity of the energy landscape of amyloid folding has frustrated these effort, for a decade. The assembly process is commonly considered as a nucleation dependent process where the conformation of assembly is determined at the nucleation phase, which is then elongated and replicated by monomer addition. Based upon this model, drug development has focused on the triggers of protein structural and functional change, generating molecules with the capacity to block the relevant conformations are therapeutics. Over the last decade, the distinctive evolutionary features of amyloid has been recognized as critical for etiology. Unlike soluble proteins, these peptides assemble into multiple conformations with equivalent thermostability and lifetime. Different conformations can possess different toxicity, requiring that the most toxic conformations be targeted. In this dissertation, we propose a new model that recognizes the evolving nature of amyloid, its structural change over time, and the resulting implications for developing therapeutics.

Aβ (16-22) E22Q, or E22Q, is the first short peptide whose conformational transition is comprehensively quantified. E22Q first assembles into anti-parallel out-of-register ribbon through entropic hydrophobic collapse, then autonomously converts to parallel in-register

fibers. The N-terminus positive charge repulsion from lysine (K) in the particle phase dictates the formation of anti-parallel β-strands. During the elongation process, when monomers are adding along the active ends of the peptide, the inter-strand glutamines can be organized as Q track, driving the strand orientation into parallel. The aqueous buffer environment mitigates the electrostatic repulsion between lysines, rendering the parallel β-sheet as the thermodynamically favored conformation.

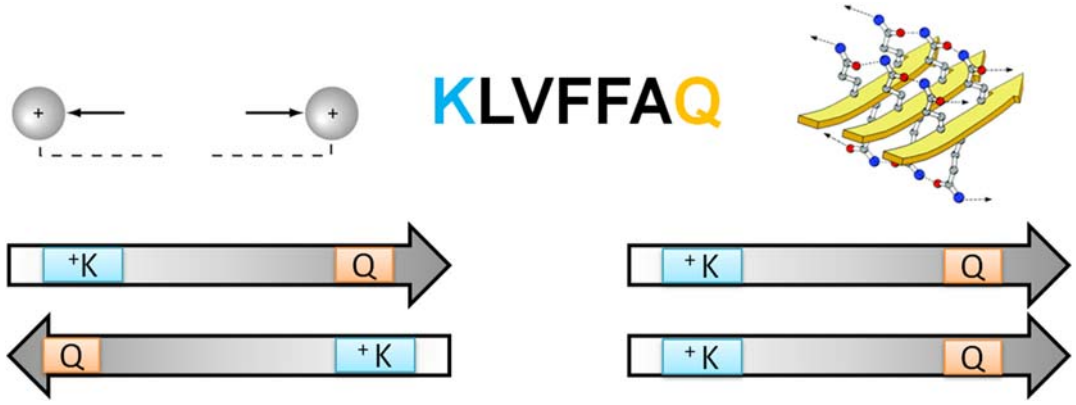

Figure 7-1. KLVFFAQ transitions from anti-parallel out-of-register to parallel in-register. At the oligomer phase, electrostatic repulsion dominates the process while eventually, inter-strand hydrogen bond between glutamines dominate the assembly process and forms parallel beta-sheet.

Isotope edited infrared spectroscopy (IE-IR) is optimized to characterize the transition of this process. Conformational specific information is obtained in-real time, a basis sets for Aβ (16-22) is developed, and the obtained IE-IR spectra are fit for each component. These results provided the first mechanistic insight into the kinetic pathway for amyloid assembly.

Environmental influences on assembly can be important, as here salt is shown to impact the assembly process through multiple stages. At the nucleation stage, salt doesn't alter the

structure of the assembly, but significantly increases the particle size and degree of assembly, following the mechanism of Hofmeister series. During elongation phase, salt speeds up the emergence of parallel β-sheet by screening lysine repulsion. On the other hand, salt impedes the transition to the thermodynamics product, kinetically trapping multiple intermediates. High salt introduces and maintains this heterogeneity by depleting the monomer concentration, stabilizing intermediates through bundling, and generating new conformations through secondary nucleation. This chapter demonstrates the significant impact of these counter-ions on these self-assembly systems.

Another factor that impacts self-assembly significantly is the position of glutamine Q. By positioning glutamine at different locations of A (16-22), significant differences in assembly structure and transition dynamics are observed. Despite similar chemical composition, their infrared signal varies drastically and the transition time varies from hours to months. This chapter demonstrates how significant the position of a single amino acid can have on the self-evolving system. This positional information now greatly extends insight into the impact of risk factors in disease etiology.

The use of isotope edited infrared spectroscopy (IE-IR) to study protein structural change is also modified. E22Q is one of the few short peptides that can be used as a model to study the normal mode of parallel β-sheets. The positional dependence of isotope enrichment on the IE-IR spectra of E22Q was shown, contrary to all existing theory, to dramatically impact the IE-IR signal when moved along the peptide backbone. The effect largely result from the disruption

of lateral coupling between ^{12}C amide bonds along strand and the coupling of ^{12}C and ^{13}C carbonyls. This study significantly promotes the current understanding of normal mode of isotope enriched systems and provides valuable insight for future experimental designs, and for the real-time analysis of amyloid assembly.

Like nucleic acid, amyloid carries sufficient information to evolve and create phenotypic functional capacity for selection in biological system. The reversibility of monomer addition allows the conformational population to be changed by multifaceted molecular forces and grow functional capability for selection. Although some amyloids form stable conformation from the beginning due to a predominantly stable energy state, more often than not, amyloid's conformation is evolving over time. These conformational intermediates are of great significance because interference at the intermediate level alters the downstream assembly pathways, therefore significantly altering the conformational distribution of amyloid. Understanding these intermediate states are critical for identifying viable targets for drug development and the forecast of these devastating amyloid diseases.

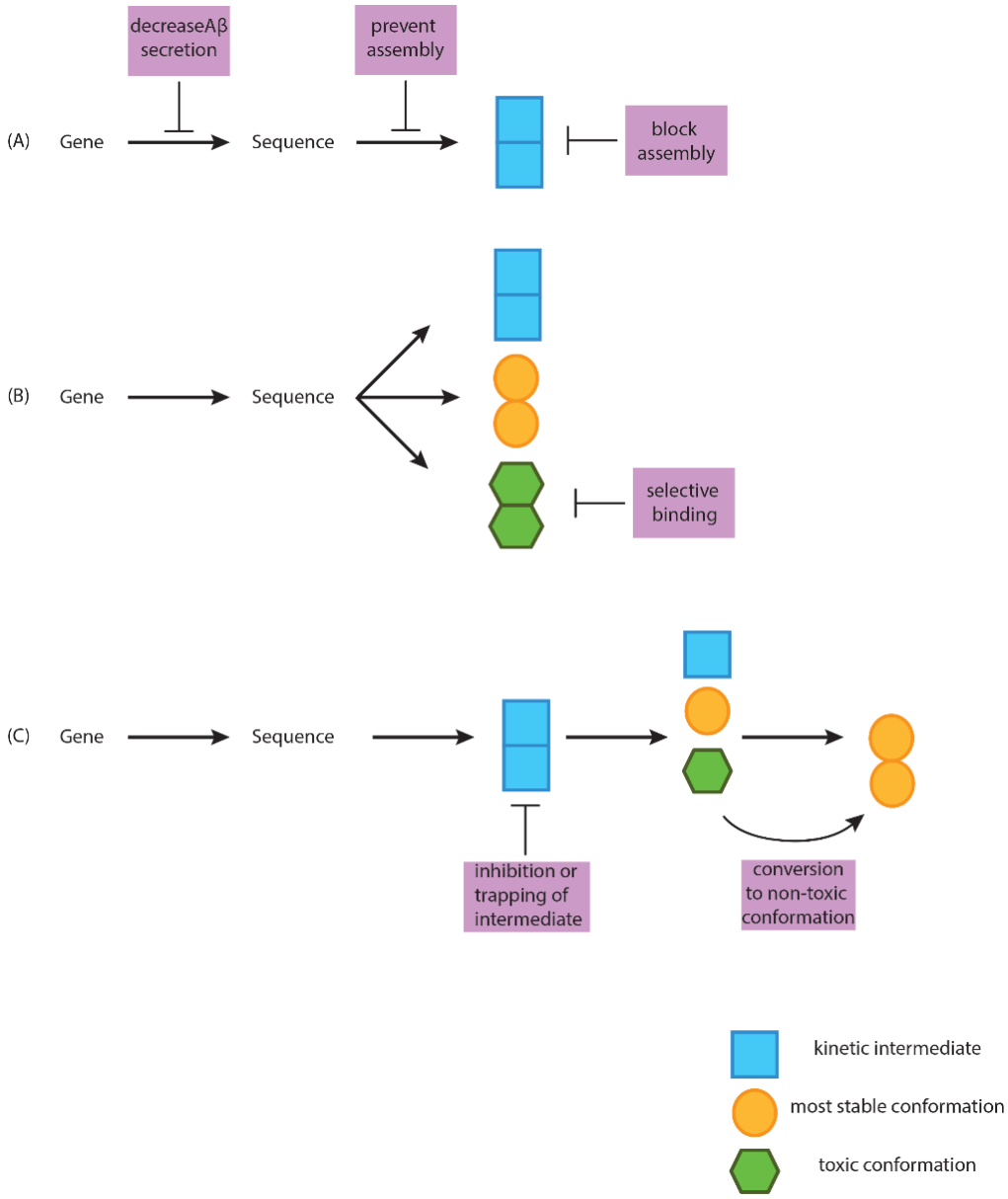

Figure 7-2. Understanding of drug development strategy dictates drug development strategy. (**A**) Drug development in nucleation dependent model targets inhibiting Aβ monomer formation, preventing assembly and blocking assembled fibers. (**B**) Polymorphism model selectively targets the most toxic species. (**C**) The inhibition of toxic species can be achieved by either blocking or trapping its precursors, or driving its conformation to less toxic ones.

The drug design strategy depends on our understanding of the amyloid assembly and the nucleation dependent model suggests that specific conformations with higher toxicity should be targeted for effective therapeutics. Under the conformational evolution model, the complex cellular environment would significantly impact the kinetics and conformational distribution of

amyloid such that the whole system needs to be monitored over time at different compartments of the brain. Multiple stages and targets can now be identified to develop treatment. The formation of toxic amyloid could be pre-empted at the intermediate level, or selection pressure could be exerted to convert the toxic species to less impactful conformations. It is still unclear what drug design strategy can be used when faced with an evolving target, but these methods outlined here revealed new strategies to harness the biological system to address their constraints on human health.